8-9-2014

Oxygen flux and dielectric response study of Mixed Ionic-Electronic Conducting (MIEC) heterogeneous functional materials

Fazle Rabbi
University of South Carolina - Columbia

Oxygen flux and dielectric response study of Mixed Ionic-Electronic Conducting (MIEC) heterogeneous functional materials

By

Fazle Rabbi

Bachelor of Science
Bangladesh University of Engineering & Technology, 2007

Submitted in Partial Fulfillment of the Requirements

For the Degree of Doctor of Philosophy in

Mechanical Engineering

College of Engineering and Computing

University of South Carolina

2014

Accepted by:

Kenneth L. Reifsnider, Major Professor

Fanglin Chen, Committee Member

Kevin Huang, Committee Member

Xiao-Dong Zhou, Committee Member

Kyle S. Brinkman, Committee Member

Lacy Ford, Vice Provost and Dean of Graduate Studies

DEDICATION

This work is dedicated to my mother Mazeda Khatun and my father Md. Mohsin Ali, whose love and sacrifices have made me the person I am today.

ACKNOWLEDGEMENTS

I would like to express my sincere gratitude to Dr. Kenneth Reifsnider for giving me this wonderful opportunity to pursue my dream. His guidance, enthusiastic encouragement, patience and unwavering support have made this an experience of a life time for me. He not only taught me to be a good researcher but also a good human being. I will cherish these years working with him and the knowledge that he shared with me. I would also like to sincerely thank Dr. Kyle Brinkman for providing me with immense support with his knowledge and expertise in this field. I am also thankful to my dissertation committee members- Dr. Fanglin Chen, Dr. Kevin Huang and Dr. Xiao-Dong Zhou for their valuable time and support with their insightful suggestions that was of immense help along the way towards my PhD.

I would like to thank all of my colleagues from the EFRC group, past and present, for their support, suggestions and contribution in my work that made my life as a PhD student a lot easier and enjoyable. I also want to thank all of my friends from around the world here in Columbia that helped me make this city a home away from home.

Last but not the least, I would like to express my love and respect to the most precious people of my life, my family, my parents, my sisters, brother-in-laws, my nieces and nephew and my fiancé for their love, support and encouragement to achieve my dream and become a better human being.

ABSTRACT

Dense mixed ionic-electronic conducting (MIEC) membranes consisting of ionic conductive perovskite-type and/or fluorite-type oxides and high electronic conductive spinel type oxides, at elevated temperature can play a useful role in a number of energy conversion related systems including the solid oxide fuel cell (SOFC), oxygen separation and permeation membranes, partial oxidization membrane reactors for natural gas processing, high temperature electrolysis cells, and others. This study will investigate the impact of different heterogeneous characteristics of dual phase ionic and electronic conductive oxygen separation membranes on their transport mechanisms, in an attempt to develop a foundation for the rational design of such membranes. The dielectric behavior of a material can be an indicator for MIEC performance and can be incorporated into computational models of MIEC membranes in order to optimize the composition, microstructure, and ultimately predict long term membrane performance. The dielectric behavior of the MIECs can also be an indicator of the transport mechanisms and the parameters they are dependent upon.

For this study we chose a dual phase MIEC oxygen separation membrane consisting of an ionic conducting phase: gadolinium doped ceria-$Ce_{0.8}Gd_{0.2}O_{1.9}$ (GDC) and an electronic conductive phase: cobalt ferrite-$CoFe_2O_4$ (CFO). The membranes were fabricated from mixtures of Nano-powder of each of the phases for different volume percentages, sintered with various temperatures and sintering time to form systematic

micro-structural variations, and characterized by structural analysis (XRD), and micro-structural analysis (SEM-EDS). Performance of the membranes was tested for variable partial pressures of oxygen across the membrane at temperatures from 850°C-1060°C using a Gas Chromatography (GC) system. Permeated oxygen did not directly correlate with change in percent mixture. An intermediate mixture 60%GDC-40%CFO had the highest flux compared to the 50%GDC-50%CFO and 80%GDC-20%CFO mixtures. Material characterization suggests the emergence of a third phase contributing to the behavior. Microstructural studies suggested changes in micro-structure of a given volume fraction for different sintering temperature and sintering time. Flux variation was observed for membranes with the same constituent volume fraction but different micro-structure indicating the effects of the micro-structure on the overall oxygen permeation.

To correlate the experimental flux measurement with a standard Wagner's flux equation, different microstructural characteristics were studied to incorporate them into a modified Wagner's flux equation.

In-situ broadband dielectric spectroscopy measurements over a temperature range of 850°C-1060°C and frequency range of (0.1Hz-1MHz) of the operating 60%GDC-40%CFO mixture oxygen separation membranes were measured using a NOVOCONTROL dielectric spectroscopy test system. Dielectric response of the operating membrane was studied to identify the charge transfer process in the membrane.

A computational model to study the dielectric impedance response of different microstructure was developed using a COMSOL^{TM} Multiphysics qasi-static electromagnetic module. This model was validated using model materials with regular

geometric shapes. To measure impedance of real micro/nano-structures of the membrane material, domains required for the COMSOL calculation were obtained from actual micro/nano structures by using 3D scans from X-ray nano and micro tomography. Simpleware™ software was used to generate 3D domains from image slices obtained from the 3D x-ray scans. Initial voltage distributions on the original microstructure were obtained from the computational model. Similarly, development of a primary model for simulating ionic/electronic species flow inside of an MIEC was also begun. The possibility of using broadband dielectric spectroscopy methods to understand and anticipate the flux capabilities of MIECs to reduce the cost and time of development of such material systems was explored.

TABLE OF CONTENTS

LIST OF TABLES

LIST OF FIGURES

LIST OF SYMBOLS

O^{2-}	Ionized oxygen.
e^{-}	Electron.
P_{O_2}	Oxygen partial pressure.
P'_{O_2}	Oxygen partial pressure on feed side (High oxygen partial pressure).
P''_{O_2}	Oxygen partial pressure on permeate side (Low oxygen partial pressure).
$V_O^{\cdot\cdot}$	Empty lattice sites for oxygen anions.
O_O^X	Uncharged oxygen ion on lattice site.
$h^{\cdot}$	Electron hole.
z_k	Charge number of charge carrier k.
σ_k	Conductivity of charge carrier k.
z_k	Charge number of charge carrier k.
F	Faraday constant.
$\nabla\eta_k$	Electrochemical potential gradient of charge carrier k.
$\nabla\mu_k$	Chemical potential gradient of charge carrier k.
$\nabla\varphi_k$	Electrical potential gradient of charge carrier k.
j_k	Flux of charge carrier k.
j_{O_2}	Oxygen flux.
σ_{el}	Conductivity of electronic phase.

σ_{ion} Conductivity of ionic phase.

$V_{f(el)}$ Volume fraction of electronic phase.

$V_{f(ion)}$ Volume fraction of ionic phase.

$\vec{D}$ Dielectric displacement.

ρ Charge density.

$\vec{H}$ Magnetic field.

$\vec{j}$ Ohmic current density.

$\vec{E}$ Electric field.

$\vec{B}$ Magnetic induction.

$\vec{P}$ Polarization.

ε_0 Permittivity of vacuum.

ε Relative permittivity.

χ Susceptibility.

$\varepsilon^*(\omega)$ Frequency dependent complex permittivity.

$\varepsilon'(\omega)$ Frequency dependent real permittivity.

$\varepsilon''(\omega)$ Frequency dependent imaginary permittivity.

$\sigma^*(\omega)$ Frequency dependent complex conductivity.

$Z(\omega)$ Frequency dependent complex Impedance.

ω Angular frequency.

LIST OF ABBREVIATIONS

CFO ..... Cobalt Ferrite ($CoFe_2O_4$)

EDS ..... Energy Dispersive X-Ray Spectroscopy

GC ..... Gas Chromatography

GDC..... Gadolinium Doped Ceria ($Ce_{0.8}Gd_{0.2}O_{1.9}$)

MIEC ..... Mixed Ionic Electronic Conductor

SEM..... Scanning Electron Microscope

SOFC ..... Solid Oxide Fuel Cells

XRD..... X-Ray Diffraction

CHAPTER 1

INTRODUCTION

Mixed Ionic Electronic Conductors (MIECs) have multiple distinct material phases and associated interfaces, for which the geometric scale and specific morphology at the micro/nano-level play an essential role in the global properties, functional behavior, and material system performance, thus determining the perm-selectivity and the magnitude of permeation of the membrane. Such materials are at the heart of revolutionary advances in devices that convert and store energy (e.g., batteries, fuel cells, solar cells, capacitors, and many electro-optical devices), and other membrane-based devices used in chemical and fuel processing, sequestration, and extraction. For example, ion conducting ceramic membranes have found application in a wide range of energy conversion devices. These systems include oxygen separation and permeation membranes [1], [2], partial oxidization membrane reactors for natural gas processing [3], solid oxide fuel cells [4] and high temperature electrolysis cells [5].

These materials are generally required to conduct ions to operate. But if the corresponding electronic flow necessary for charge balance is not provided by an external circuit, mixed ionic-electronic conduction is required. But designing and optimizing a single phase material capable of conducting both ions and electrons remains a challenge. Thus, to impart dual conductivity behavior, ionic conductive materials were mixed with electronic conductive materials to form an MIEC material. Design, control, and

fabrication of these materials with specific micro or nano-structure to achieve prescriptive functional performance of the material systems and devices has seen incredible progress due to the development of variety of additive manufacturing methods and techniques. However, systematic multiphysics analysis methods properly set on field equations that represent the local details of such material systems is not available, so that first-principles understandings and designs of those heterogeneous materials are not properly founded.

1.1 Separation membranes

Separation membranes can be described as a partition between two volumes of different species which preferentially allows one species (i.e. oxygen in case of oxygen separation membrane) to permeate through due to the presence of a driving force such as a pressure, electric, or chemical potential gradient. Dense separation membranes can be divided into 3 types-

a. Ceramic membranes.
b. Metal membranes.
c. Liquid-immobilized membranes.

Ceramic separation membranes have promising applications in the field of solid oxide fuel cells and oxygen permeable separation membranes. There are several different types of ceramic structures that are capable of exhibiting oxygen permeation behavior. A significant number of oxygen permeable ceramics that have been developed including perovskite-type oxides in ternary or quaternary systems consisting of rare-earth, alkaline-earth, and transition metals. $La_{0.7}$ $Sr_{0.3}Ga_{0.6}Fe_{0.4}O_{3-\delta}$ [6], $Pr_{0.7}Sr_{0.3}Fe_{0.8}Al_{0.2}O_{3-\delta}$ [7] and $Ba_{0.5}Sr_{0.5}Co_{0.8}Fe_{0.2}O_{3-\delta}$ [8] are well known to exhibit a high oxygen flux density reaching

to 8 μmol·cm^{-2}·s^{-1} at elevated temperatures under methane conversion atmospheres. In addition to these single-phase mixed conductors, dual-phase-type mixed conductors comprising of ionic and electronic conductive phases have also been developed [9]–[12]. These dual phase MIECs can be divided into two subgroups of oxide-oxide and oxide-metal mixture materials. Several recent studies of oxide-oxide MIEC membranes have been conducted. Wang et. al. studied mixtures of $Zr_{0.8}Y_{0.2}O_{1.9}$ (ZYO) and $La_{0.8}Sr_{0.2}CrO_{3-\delta}$ (LSC) [13] with the volume ratio of 60%ZYO-40%LSC. Wu et. al. studied mixtures of $Bi_{1.5}Y_{0.3}Sm_{0.2}O_3$ (BYS) and $La_{0.8}Sr_{0.2}MnO_{3-\delta}$ (LSM) [14] with volume ratios of 60%BYS-40%LSM, 65%BYS-35%LSM and 70%BYS-30%LSM. Wang et. al. studied $La_{0.15}Sr_{0.85}Ga_{0.3}Fe_{0.7}O_{3-\delta}$ (LSGF) and $Ba_{0.5}Sr_{0.5}Fe_{0.2}Co_{0.8}O_{3-\delta}$ (BSCF) [15] at the volume ratio of 0.928%LSGF-0.072%BSCF and Kharton et. al. have studied mixtures of $Ce_{0.8}Gd_{0.2}O_{2-\delta}$ (CGO) and $La_{0.7}Sr_{0.3}MnO_{3-\delta}$ (LSM) [16] with a weight ratio of 50%CGO-50% LSM.

Similarly, extensive research has been done on oxide-metal mixture MIECs. 50YSZ-50Pd mixture of $(ZrO_2)_{0.94}(Y_2O_3)_{0.06}$ (YSZ) and Palladium (Pd) with the volume ratio of 60%YSZ-40%Pd were studied by Chen et. al. [17], Capoen et. al. studied $(Bi_2O_3)_{0.75}(Er_2O_3)_{0.25}$ (ESB)-Silver(Ag) with a volume ratio of 60%ESB-40%Ag [18], $Bi_{1.5}Y_{0.3}Sm_{0.2}O_3$ (BYS) and silver(Ag) mixtures were studied by Kim et. al. [19] and $(Bi_2O_3)_{0.74}(SrO)_{0.26}$ (SSB) and silver(Ag) mixtures were studied by Wu et. al. [20]. Due to their mixed oxygen-ion and electronic conducting capability, the studies of these MIECs has become very important for their promising applications, such as the production of pure oxygen from air and hydrogen form hydrocarbons [21], [22]. With dual-phase composite mixed conductors it is possible to control the mixed conductivity by using

different volume fractions of the two different phases and to adjust to particular operation requirements. Thus, to measure the performance of oxygen separation membranes made of MIEC materials, the contribution of both the ionic and electronic conductivities as well as the interactions between the two different phases due to their material properties and morphology variations on the charge transport mechanisms must be considered. The oxygen flux through an MIEC membrane can generally be described by the Wagner equation in terms of combined material conductivity where the equation is constructed based on the two conductivities, ionic and electronic [23].

1.2 Separation membrane systems

In an oxygen separation membrane system, oxygen passes through the ionic conductive phase in ionic form and to maintain electric neutrality there must be a simultaneous flux of electrons in the opposite direction to compensate for the opposite charge of the oxygen flux. So separation membrane systems based on ceramic materials can generally be divided into two classes. For both cases a driving force is needed for the oxygen to permeate through the oxygen separation membrane.

The driving force can be a chemical potential gradient (i.e. oxygen partial pressure gradient) or electrical potential gradient across the membrane [23], [24]. For materials with ionic conductivity only, the path for the electrons to flow in order to maintain charge neutrality is provided by the electrodes shown in Figure 1.1. Such a system has the inherent benefit that the amount of oxygen ion flow and thus the `generation of oxygen can be controlled by controlling the electron flow through the external electrode.

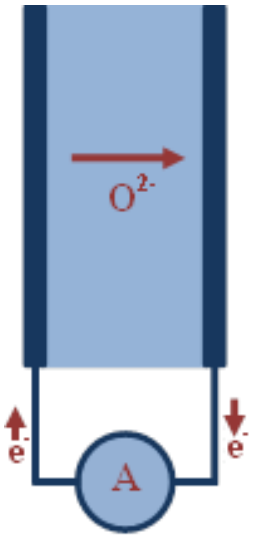

Figure 1.1. Single-phase ionic conducting separation membranes with electric potential as driving force.

But for an MIEC membrane, no electrodes are required to operate. The only driving force required is the oxygen pressure difference on both sides of the membrane. These membranes can be either a single phase material capable of conducting both electrons and ions as shown in Fig. 2.2(a) or a two phase mixture of two different materials as shown in Fig. 2.2(b), one ionic conductive and the other an electronic conductive material.

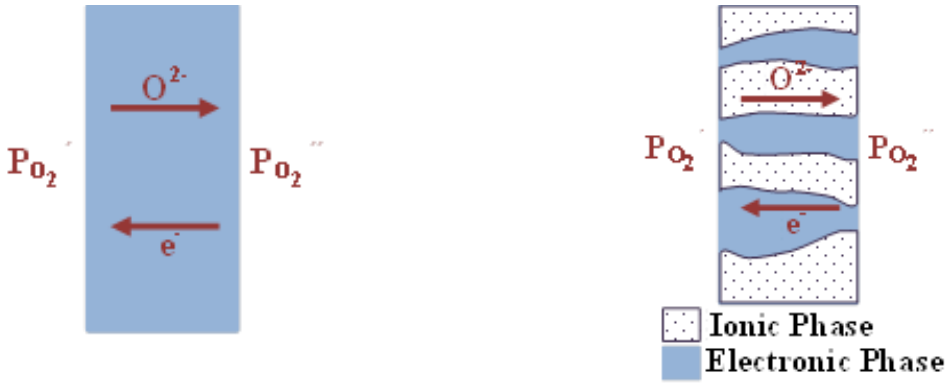

(a) (b)

Figure 1.2. Mixed ionic electronic conducting, a) single phase oxygen separation membrane, b) dual phase oxygen separation membrane.

The MIEC behavior of several materials have been reported by the several research groups [9], [10], where insoluble metallic or any other electronic conductive ceramic is incorporated into a predominantly ionic conducting phase to introduce MIEC properties.

For our study of the behavior of heterogeneous MIECs, gadolinium doped Ceria-$Ce_{0.8}Gd_{0.2}O_{1.9}$ (CGO) Cobalt ferrite-$CoFe_2O_4$ (CFO) was selected as the ion and electronic conducting phase respectively. Coupled transport of ions and electrons through the two different phases in opposite directions enables the permeation of ions through the membrane. These charge transport mechanisms are functions of different parameters of the system as well as the materials properties originating from the interaction between the constituents. Heterogeneous MIECs display conduction characteristics that are also highly dependent on morphology and local geometry [25], [26]. These characteristics of the morphology of the systems are a function of synthesis conditions such as primary constituents' condition, sintering temperature, and time etc. By controlling these, systematic variations of the local morphology and microstructure can be obtained and their influence on overall membrane operation can be identified.

CHAPTER 2

FUNDAMENTALS OF DENSE MIXED CONDUCTING OXYGEN SEPARATION MEMBRANES

Recent advancements in the field of dense MIEC oxygen separation membranes have enhanced the oxygen permeation rate with high perm-selectivity. Simplicity of operation has created interest among researchers to develop MIECs as a potentially clean, efficient and economical means of producing pure oxygen by separation from air or other oxygen-containing gas mixtures.

2.1 Working Principle

The working principle of MIEC membranes can be described as follows. First the membrane temperature is increased to an operating temperature that initiates the ionic oxygen flow through the membrane. At the feed side atmospheric air is flowed and at the permeate side oxygen at lower pressure is maintained.

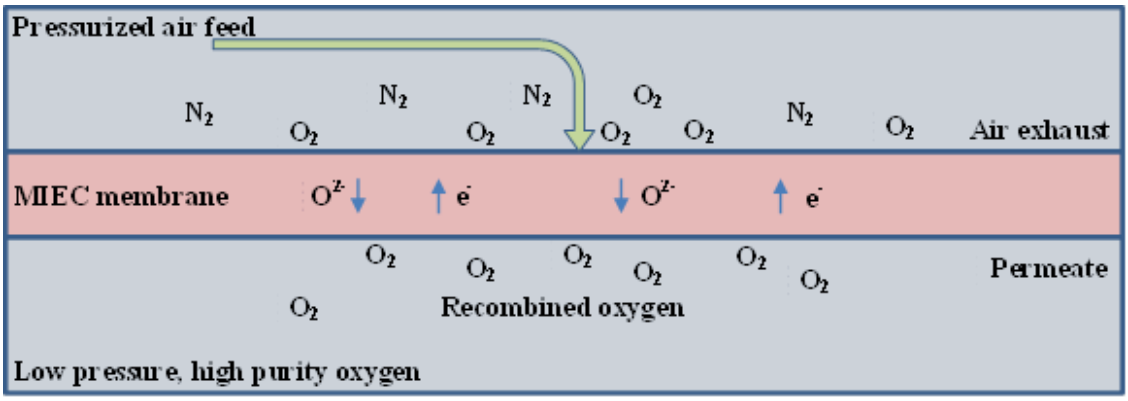

Figure 2.1. Schematic of oxygen ion and electron flow in an MIEC oxygen separation membrane.

This differential of oxygen partial pressure applied across the membrane is the driving force for overall oxygen transport.

As the MIEC is a dense gas tight barrier, it blocks the direct transport of oxygen molecules. But the oxygen ions migrate selectively through the membrane. Transport (permeation) of oxygen through the membrane occurs as a coupled transport of ions and electrons. The overall process is divided into three steps as shown in Figure 2.1:

Oxygen at the oxide surface at the feed side (high oxygen partial pressure) is dissociated and ionized, where the oxygen molecule picks up electrons from accessible surface electronic states and changes into oxygen ion. The oxygen ions travel through the membrane via the oxygen vacancy sites:

(a) $^{1}/_{2}O_{2}(g) + 2e^{-}(M) \rightarrow O^{2-}(I)$ at one surface (*Feed*).

Simultaneous flux of electronic charge carriers through the electronic conductive phase charge compensates for the flux of oxygen ions:

(b) Coupled transport of O^{2-} and $2e^{-}$ in opposite directions through the bulk.

The oxygen ions reach the permeate side (low oxygen partial pressure) and each ion recombines again to form oxygen molecules by releasing their electrons in the electronic conducting phase of the membrane. And this recombined oxygen is released in the permeate stream as pure oxygen:

(c) $O^{2-}(I) \rightarrow {}^{1}/_{2}O_{2}(g) + 2e^{-}(M)$ at the other surface (*Permeate*).

2.2 MIECs as oxygen separation membranes

Developing a single-component material that exhibits both large ionic and electronic conductivity is a difficult task. The process becomes even more complicated if the material is required to operate within an appropriate range of temperature and oxygen

partial pressures with good surface activity for the transfer of gas-phase oxygen to the solid material. Thus, an ideal composite material would have one phase as a good oxygen ionic conductor and another phase as a good electronic conductor. In addition, the introduction of another phase to enhance the electronic conductivity in materials with low electronic conductivity has become a quite desirable but challenging strategy. These composite materials significantly improve the oxygen permeation of the ceramic phase alone (mainly fluorite), by up to 2 or 3 orders of magnitude, as shown by J. Sunarso el al. [12], where they compared the oxygen flux of single phase ionic and dual phase MIEC materials.

2.2.1 Structure of the MIEC ceramic membrane

For this study the materials we selected to synthesize for the MIEC were Gadolinium doped Cerium (GDC) as the ionic conducting phase and Cobalt Ferric Oxide (CFO) as the electronic conducting phase. The GDC has a Flourite type structure and CFO is a spinel-type mixed-metal composite.

2.2.1.1 Flourite Compounds

Calcium fluoride (CaF_2) has the basic crystal structure known as fluorite, which is shown in Figure 2.2. Fluorite is one of the most common crystalline solid types found in nature. The basic structure for a fluorite can be described as a face centered cubic packing of cations, with anions in all of the tetrahedral holes. It can also be described as a simple cubic packing of anions with cations in the cubic (8-coordinate) holes. To maintain an ideal fluorite structure with cation-anion contact and closest packed cations, the cation to anion radius ratio must be 4.38. A smaller cation to anion radius ratio would push the

cations apart such that they would not be as closely packed, as observed in all known compounds.

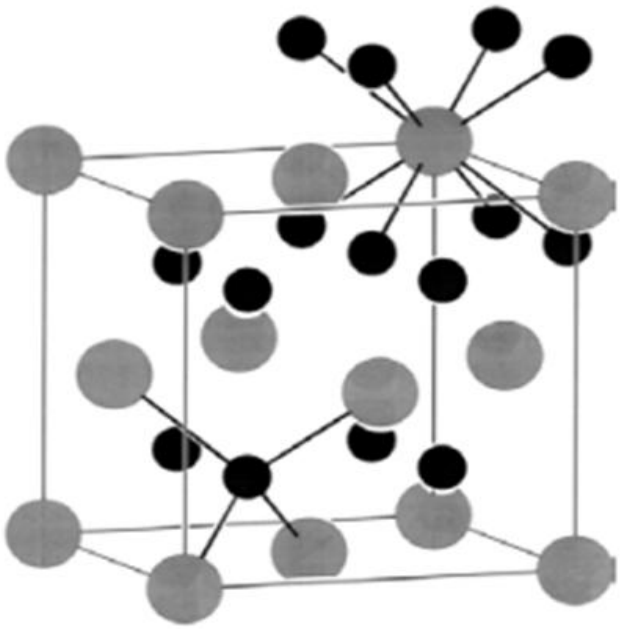

Figure 2.2. An ideal cubic fluorite CaF_2 structure where Black atoms are F^{1-} anions and gray atoms are Ca^{2+}cations.

A larger ratio would mean that the anions could not be in contact with all 4 coordinating cations at once and thus is not possible. Fluorite tends to have mainly ionic cation-anion bonds. Although an ideal fluorite/antifluorite structure has a very high atom density, cation to anion radius ratios tend to be much closer to one, forcing the closest packed atoms apart and dramatically decreasing the density [27].

2.2.1.2 Cerium (IV) Oxide

Cerium dioxide crystallizes in the cubic fluorite structure because it has the same atomic structure as calcium fluoride. The lattice structure refers to the orientation of cerium cations and oxygen anions in space. The cerium cations crystallize in a face

centered cube, and the oxygen anions fill the tetrahedral positions in the metal cage. The ceria structure is shown in Figure 2.3.

In oxygen deficient environments the Ce atoms are reduced from a 4+ state to a 3+ state. As a result crystalline CeO_2 is known to exhibit minor defects. This behavior can be extrapolated as high surface area ceria nanoparticles grown in open air increase the ability of Ce to change oxidation states.

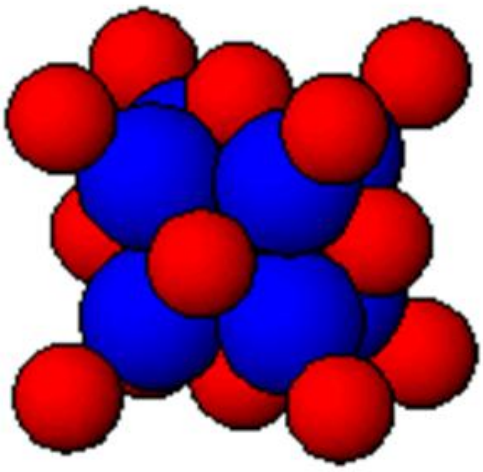

Figure 2.3. CeO_2 Fluorite Structure where red atoms are Cerium and Blue atoms are Oxygen.

Ce^{3+}'s high affinity for oxygen absorption allow for O_2 uptake [28]. Prepared CeO_{2-x}nanotubes exhibit higher oxygen absorption than the nanoparticles because of their larger surface area (both inner and outer surface of the tubes) [29]. Cerium oxide compound are useful in catalytic converters as oxygen storage material to reduce CO and NO emissions in automobiles.

2.2.1.3 Gadolinium doped Ceria

Gadolinium doped ceria has a structure similar to the half unit cell shown in Figure 2.4, where one alternative lattice space is filled with ceria and trivalent dopant gadolinium which gives rise to the creation of oxygen vacancies [30], [31].

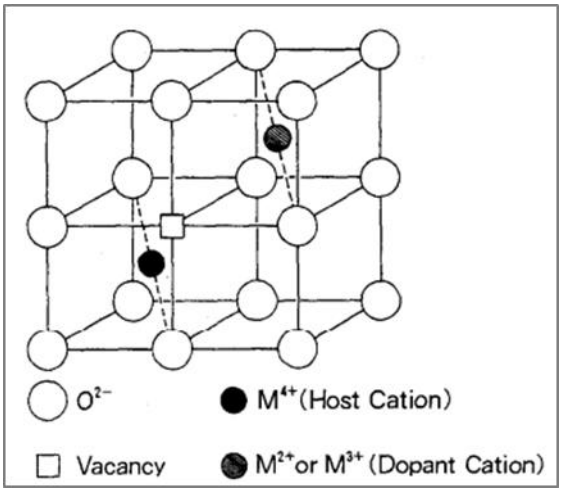

Figure 2.4. A half unit cell of the fluorite structure showing the position of dopant cation-oxygen vacancy [30]

2.2.1.4 Spinel-Type mixed-metal composites

Spinel type mixed metal composites are one of the most widely used metal oxides. It is an important group of mixed metal oxides, as different members in the groups are used in energy storage, magnetic application and catalytic reactions. The general chemical composition of the spinel type metal oxide can be represented as AB_2O_4 where A is a divalent atom of radius between 80 and 110pm, such as Mg, Fe, Mn, Zn, and Cu. And B is a trivalent atom of radius between 75 and 90pm, such as Ti, Fe, Al, and Co. The structure consists of a cubic closed-packed array of 32 oxide ions, which forms 64 tetrahedral holes and 32 octahedral holes in one unit cell containing eight formula

units $(AB_2O_4)_8$ [32]. There are two types of sub-cells commonly described for the spinel structure, here shown as crystal structure in Figures 2.5 and 2.6respectively.

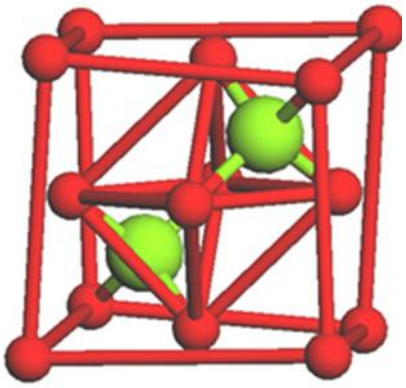

Figure 2.5. Two kinds of occupied tetrahedral sites in spinel sub-cell a. A is in green and O is in red.

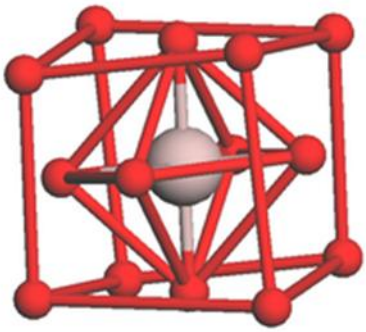

Figure 2.6. Occupied octahedral site in spinel sub-cell b. B is in gray, and O is in red.

Structure in Figure 2.5 shows the filling of 2 tetrahedral sites within one-eighth of the unit cell, and structure in Figure 2.6 shows a filled octahedral site. The arrangement of these two cubic sub-cells in one unit cell is shown in Figure 2.7. There are 12 filled octahedral sites not centered in the sub-cells that are also filled to give a total of 16 filled octahedral sites. In a normal spinel structure, all the trivalent cations are located in half of the octahedral sites, while all of the divalent cations occupy 1/8 of the tetrahedral sites.

2.2.1.5 Spinel-Type ferrite composite

$CoFe_2O_4$ has an inverse spinel crystal structure. In the normal crystal structure of an AB_2O_4 spinel, the A^{2+} atoms occupy all of the tetrahedral coordination sites and the B^{3+}atoms occupy all of the octahedral sites [33]. In the case of an inverse spinel such as $CoFe_2O_4$, the cobalt (Co) cation occupies one half of the octahedral coordination sites.

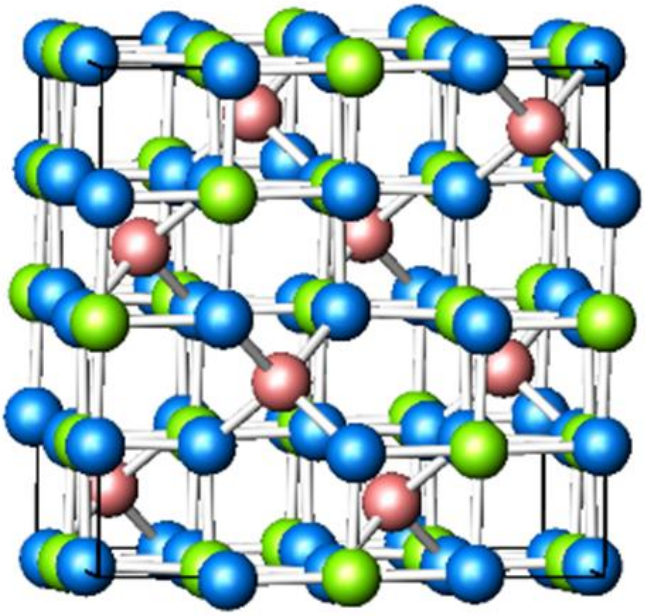

Figure 2.7. Crystal Structure of $CoFe_2O_4$ where green atoms are Co, pink atoms are Fe, and blue atoms are O.

Half of the Fe^{3+} cations occupy the other half of the octahedral coordination sites as well as all of the tetrahedral coordination sites. The crystal structure of $CoFe_2O_4$ is shown in Figure 2.7.

2.3 Flux theory of dual-phase mixed conducting oxygen separation membranes

2.3.1 Wagner equation

The Wagner equation for a Mixed Ionic-Electronic Conducting oxygen separation membrane is based on the assumption that the lattice diffusion of oxygen or the transport of electronic charge carriers through bulk oxide is the controlling factor for the overall oxygen permeation through the bulk membrane. This oxygen is transported selectively through the membrane in the form of oxygen ions, rather than molecules, under the driving force of a gradient in oxygen chemical potential. The flux of oxygen ions is charge compensated by a simultaneous flux of electrons or electron holes, which is enabled without the use of external circuitry.

The flow of oxygen ions through the membrane can be described by the interaction of gaseous oxygen with the oxide lattice and can be represented by a chemical reaction of the form

$$\frac{1}{2}O_2+V_O^{\cdot\cdot}+2e'=O_O^X \tag{2-1}$$

Here the oxygen vacancies can be assumed to be the mobile ionic defects. These may be created, e.g., by doping of the oxide lattice with aliovalent cations. The intrinsic ionization across the band gap can be is represented by

$$nil=e'+h^{\cdot} \tag{2-2}$$

Thus the flux equation for the single particle charge carrier can be written as

$$j_k=-\frac{\sigma_k}{z_k^2F^2}\nabla\eta_k \tag{2-3}$$

Where z_k is the charge number and σ_k is the conductivity of charge carrier k, F the Faraday constant, and $\nabla\eta_k$ the gradient of the electrochemical potential. The electrochemical potential $\nabla\eta_k$ is actually the combination of a gradient in chemical potential $\nabla\mu_k$ and a gradient in electrical potential $\nabla\varphi$, and thus $\nabla\eta_k$ represented as below

$$\nabla\eta_k=\nabla\mu_k+z_kF\nabla\varphi \tag{2-4}$$

Due to the rapid diffusion of charge carriers, an electrical potential $\nabla\varphi$ is generated. This causes the charge carriers to move at an accelerated rate with respect to the electrical potential direction. No charge accumulation occurs at the steady state. Thus the fluxes of ionic and electronic defects can be related to each other by the charge balance

$$2j_{V_O^{\cdot\cdot}}=j_{e'}-j_{h^{\cdot}} \tag{2-5}$$

To obtain the flux of oxygen vacancies in terms of the chemical potential gradients only, we use equation 2.3, 2.4 and 2.5 eliminate the electrostatic potential gradient. If it is further assumed that internal defect chemical reactions are locally not disturbed by the transport of matter, the chemical potential gradients of individual charge species can be converted into the virtual chemical potential of gaseous oxygen, μ_{O_2}. The following differential relations hold at equilibrium

$$\frac{1}{2}\nabla\mu_{O_2}+\nabla\mu_{V_O^{\cdot\cdot}}+2\nabla\mu_{e'}=0 \tag{2-6}$$

$$\nabla\mu_{e'}+\nabla\mu_{h^{\cdot}}=0 \tag{2-7}$$

where $\mu_{V_O^{\cdot\cdot}}$ denotes the chemical potential of the oxygen vacancy, $\mu_{e'}$ and $\mu_{h^{\cdot}}$ denoting the chemical potential of electrons and electron holes, respectively. The flux of

oxygen through the membrane can be derived by combining Equations (2.3) to (2.7), using the relationship $j_{O_2}=-\frac{1}{2}j_{V_O^{\cdot\cdot}}$

One finds,

$$j_{O_2}=-\frac{1}{4^2F^2}\left[\frac{(\sigma_{e'}+\sigma_{h^{\cdot}})\cdot\sigma_{V_O^{\cdot\cdot}}}{(\sigma_{e'}+\sigma_{h^{\cdot}})+\sigma_{V_O^{\cdot\cdot}}}\right]\nabla\mu_{O_2} \tag{2-8}$$

or, in a more generalized form,

$$j_{O_2}=-\frac{1}{4^2F^2}\left[\frac{(\sigma_{el}\cdot\sigma_{ion})}{(\sigma_{el}+\sigma_{ion})}\right]\nabla\mu_{O_2} \tag{2-9}$$

Where $\sigma_{ion}=\sigma_{V_O^{\cdot\cdot}}$ and σ_{el}-$\sigma_{h^{\cdot}}$+$\sigma_{e'}$ are the partial ionic and electronic conductivity, respectively. The conductivity term in Equation (2.9) is equivalent to $t_{el}t_{ion}\sigma_{total}= t_{ion}\sigma_{el}=t_{el}\sigma_{ion}$, where t_{el} and t_{ion} are the fractions (transference numbers) of the total conductivity σ_{total} provided by electronic and ionic defects, respectively. Integration of equation (2.9) across the oxide membrane thickness, L, using the relationship $\nabla\mu_{O_2}=\frac{\partial}{\partial x}RT\ln P_{O_2}$(x = distance coordinate) and assuming no divergence in the fluxes, yields the Wagner equation in the usual form, [23], [34]

$$j_{O_2}=-\frac{RT}{4^2F^2L}\int_{\ln P'_{O_2}}^{\ln P''_{O_2}}\left[\frac{(\sigma_{el}\cdot\sigma_{ion})}{(\sigma_{el}+\sigma_{ion})}\right]d\ln P_{O_2} \tag{2-10}$$

Here the oxygen partial pressures available on the either side of the membrane are used as the limits of the integration. Equation (2-10) has general validity for mixed conductors. For a more detailed derivation for a specific mixture, defect chemistry as well as material interaction between phases is must be considered. Several investigations have suggested similar modification of the flux equation considering microstructural, concentration factors and other parameters. Huang et al. [35] used a modified flux

equation for CO_2 separation membranes considering microstructural and concentration factors. Song et al. [36] reported modification of the flux equation for hydrogen separation membranes where they considered atomic diffusion through nickel phase and included with the standard flux equation consist of the proton and electron conduction terms. It is our goal in this work to include similar terms originated from internal material properties and include them in the standard equation shown in equation (2-10). For example, the Wagner's equation does not take into consideration the comparative amount of ionic and electronic phase in the MIEC as well as the structural and interfacial effects between the constituents. Thus, to predict flux through a composite membrane, these effects must be considered.

2.3.2 Modified Wagner's equation

It is clear that species flux through a heterogeneous membrane results from a complex combination of actions and interactions at the local microstructural level. Processing (or aging) variations in size, shape, connectivity, interface/interphase characteristics, and physical properties of the constituent phases can change the global transport properties greatly, and even in an anomalous manner that is not in proportion to systematic changes in such variables as the volume fraction of a given phase. Design of such material systems is an expensive and time consuming process of anecdotal trial and error unless comprehensive modeling approaches based on the controlling physics and chemistry are available.

The classical approach to such modeling is to construct an "effective medium" concept to incorporate the details of the constituents. The literature for such an approach is extensive; many reviews are available [37]. For charge displacement, the most widely

recognized approach is the Maxwell-Wagner-Sillars (MWS) model [38], [39]. Many additions include an asymmetrical integration technique (by Bruggeman [40]) and extension of "filler" geometry to elliptical geometries [41]. Heterogeneous materials containing more than two phases have also been considered by Bilboul and others [42]. However, prior effective property models have limited or no utility for the present problem. This will be the subject of a subsequent paper, but a few comments are added here. Effective property models are generally concerned with distributions of an additive or 'filler' phase in a matrix of otherwise continuous material. In some of the advanced models, some connectivity of the distributed phase is allowed, but non-dilute mixtures are not rigorously represented and fully dense interlaced phases are not represented. To our knowledge, no ionic flux models for heterogeneous materials have been set on the actual heterogeneous microstructure (from observations). Specifically, the electrochemical considerations that control the balance of electrical and ionic conduction essential for the proper design of the microstructure of a separation membrane have not been integrated with effective property theory, per se. A step in that direction can be found in the work of Buttin wherein a one dimensional flux problem for transport of oxygen through a double layer of YSZ and YSZ oxide has been constructed to provide inputs into a standard Wagner equation for mixed conductors [43].

In this study we will compare experimental flux through the membranes with three different volume fractions and compare with the calculated value of flux using the standard Wagner's flux equation shown in Equation 2-10. The single phase values of ionic conductivity, σ_{ion} and electronic conductivity, σ_{el} is measured experimentally using a NOVOCONTROL^{TM} impedance measurement system. For a mixture with more than

one constituent of electronic or electronic conductive phases, the conductivity of the phases can be combined using the following mixture Equation (2-11) and Equation (2-12).

$$\sigma_{el}=V_{f(el1)}\cdot\sigma_{el1}+\left(1-V_{f(el1)}\right)\sigma_{el2} \quad (2\text{-}11)$$

$$\sigma_{ion}=V_{f(ion1)}\cdot\sigma_{ion1}+\left(1-V_{f(ion1)}\right)\sigma_{ion2} \quad (2\text{-}12)$$

The combined conductivity used in the Wagner's equation does not take into account the comparative amount of the two phases (electronic-ionic), so one approach might be used is shown in equation 4 utilized in the of the MPM model [44],

$$\sigma_C=(\lambda-k)\sigma_{el}V_{el}^2+k(\sigma_{el}-\sigma_{ion})V_{el}+\sigma_{ion} \quad (2\text{-}13)$$

In which the parameter, k, carries information about the integrity of the phases (are they interacting, contiguous, etc.) and λ carries information about the dispersion of the phases, i.e., the surface to volume ratio of the phases present ($\lambda\approx1$ representing widely dispersed particles to $\lambda\approx0$ representing single dispersed phase etc.). For example, if $\lambda>k$, i.e., lots of second phase particles per unit volume fraction, V_f , but the collective electronic conductivity is smaller than the ionic value (perhaps because of loss of connectivity, etc.), then the variation of the combined conduction as a function of volume fraction of the additive phase has a maximum. The values of the parameters k and λ can be computed by using x-ray tomography techniques similar to the process demonstrated by Nelson et. al. [45]. In this process, x-ray nanotomography is used to construct a 3D representation of the segmented phases. Surface area shared by the phases, volume fraction of connected regions can be obtained from these 3D images. Equation (2-13) includes the volume fraction in determining the total conductivity that can be used in the Wagner's equation. Similar work has been done by Zhang et. al. where they modify the Wagner's equation to

calculate flux through porous CO_2 separation membrane [35]. This modified equation takes into account the volume fraction variation of the two phases (electronic-ionic) as well as the porosity and tortuosity of the membrane.

CHAPTER 3

SYNTHESIS AND CHARACTERIZATION OF MEMBRANES

3.1 Sample preparation

The dual phase membranes were prepared by mixing the respective volume percent of the ionic conductive phase $Ce_{0.8}Gd_{0.2}O_{1.9}$ (InfraMat Advanced Materials LLC) and the electronic conductive phase $CoFe_2O_4$ (InfraMat Advanced Materials LLC) by ball milling powder in ethanol for 6 hours. Three different composition of mixture ratios- 50% GDC-50%CFO, 60% GDC-40%CFO and 80% GDC-20%CFO were prepared for the present study. After drying and sieving, the ceramics were mixed with a 0.1% mass PVA synthetic binder to facilitate the die press process of the sample. 1.6gm of powder mixtures were uniaxially pressed into pellets of 20 mm diameter with a force of 20 kN to get a sample of 18mm diameter because each sample diameter reduced during sintering. Samples were sintered for two different conditions, - at 1300°C for two hours and 1300°C for five hours. For the 80% GDC-20%CFO mixture, samples sintered at 1400°C for two hours were also prepared. Temperature ramp rate of 2^oC/minute during heating and cooling stages were used in the furnace. The surface of each side of the samples was polished to remove any surface roughness from the sintering process. The polishing process was done by gradually increasing the grit count of the silicon carbide sandpaper to 1200. The thickness of each final sample was 0.9mm.

The different sintering conditions used for the sample preparation are presented in Table 3.1.

Table 3.1. Sintering cycles used for different membranes.

Sintering Cycles	Membrane Mixture
Room temp to 1300°C @ 2°C/min Hold at 1300°C for 2 Hrs 1300°C to 900˚C @ 2°C/min 900˚C to room temp	50GDC-50CFO, 60GDC-40CFO, 80GDC-20CFO
Room temp to 1300°C @ 2°C/min Hold at 1300°C for 5 Hrs 1300°C to 900˚C @ 2°C/min 900˚C to room temp	50GDC-50CFO, 60GDC-40CFO, 80GDC-20CFO
Room temp to 1400°C @ 2°C/min Hold at 1300°C for 5 Hrs 1300°C to 900˚C @ 2°C/min 900˚C to room temp	80GDC-20CFO

Ceramics were characterized from 10 to 90 degrees two theta on a PanAnalytical X-ray diffractometer to determine phase formation. The sintered microstructure and chemical composition were investigated on a Hitachi instrument equipped with Energy Dispersive Spectroscopy (EDS).

3.2 Flux measurement Setup

3.2.1 Flow system

The experimental setup had two primary parts. The first part consisted of the Probostat^{TM} that has two chambers separated by the membrane sample, each chamber had

input and output flow outlets for two different types of gases. The second part consisted of an Agilent 3000 Micro Gas Chromatographer used to measure oxygen in a sweep gas obtained from the Probostat™. The ProboStat™ is a test cell that enables measurements of electrical properties, transport parameters, and kinetics of materials, solid/gas interfaces and electrodes under controlled atmospheres at high temperatures up to 1600ºC. Figure 3.1 shows a schematic of the sample station and the electrode and gas supply assembly of the Probostat™ connected with the gas chromatograph. The sample under test rests on a 50 cm long support tube of alumina with an inner diameter of 15 mm, inside of a closed outer tube of alumina or silica. A spring-loaded alumina assembly holds the sample in place. A gold seal ring is placed between the sample and support tube to stop leakage between the two chambers. Figure 3.2 shows the schematic of the membrane sample set inside the sample station with gold seal. Helium gas is flowed in the inside chamber through a silica tube near the bottom surface of the sample as the sweep gas. The sweep gas was collected from the bottom of the inner chamber and passed to the GC. A steady flow of air was maintained on the top of the sample on the outer chamber and then released into the atmosphere. In the Gas Chromatograph (GC), Helium was used as the carrier gas. Helium of constant pressure at 80Psi was supplied to the GC as the carrier gas, and the sweep gas from the exit port of the Probostat™ inner chamber was supplied to the GC to analyze the permeated oxygen content. Figure 3.3 shows a picture of the base of the Probostat™ containing the gas supply ports for the experiments.

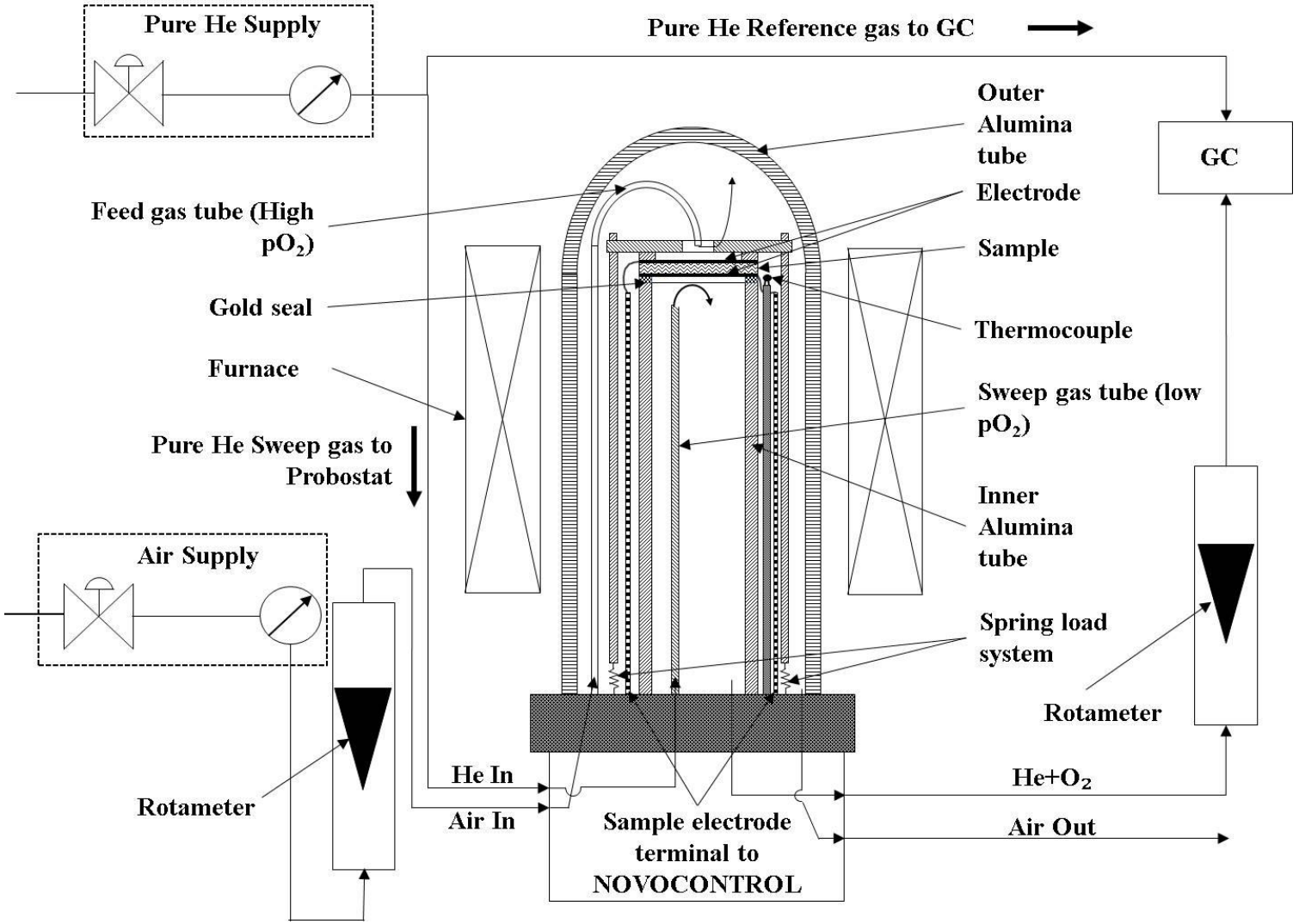

Figure 3.1. Complete in-situ measurement set-up block diagram.

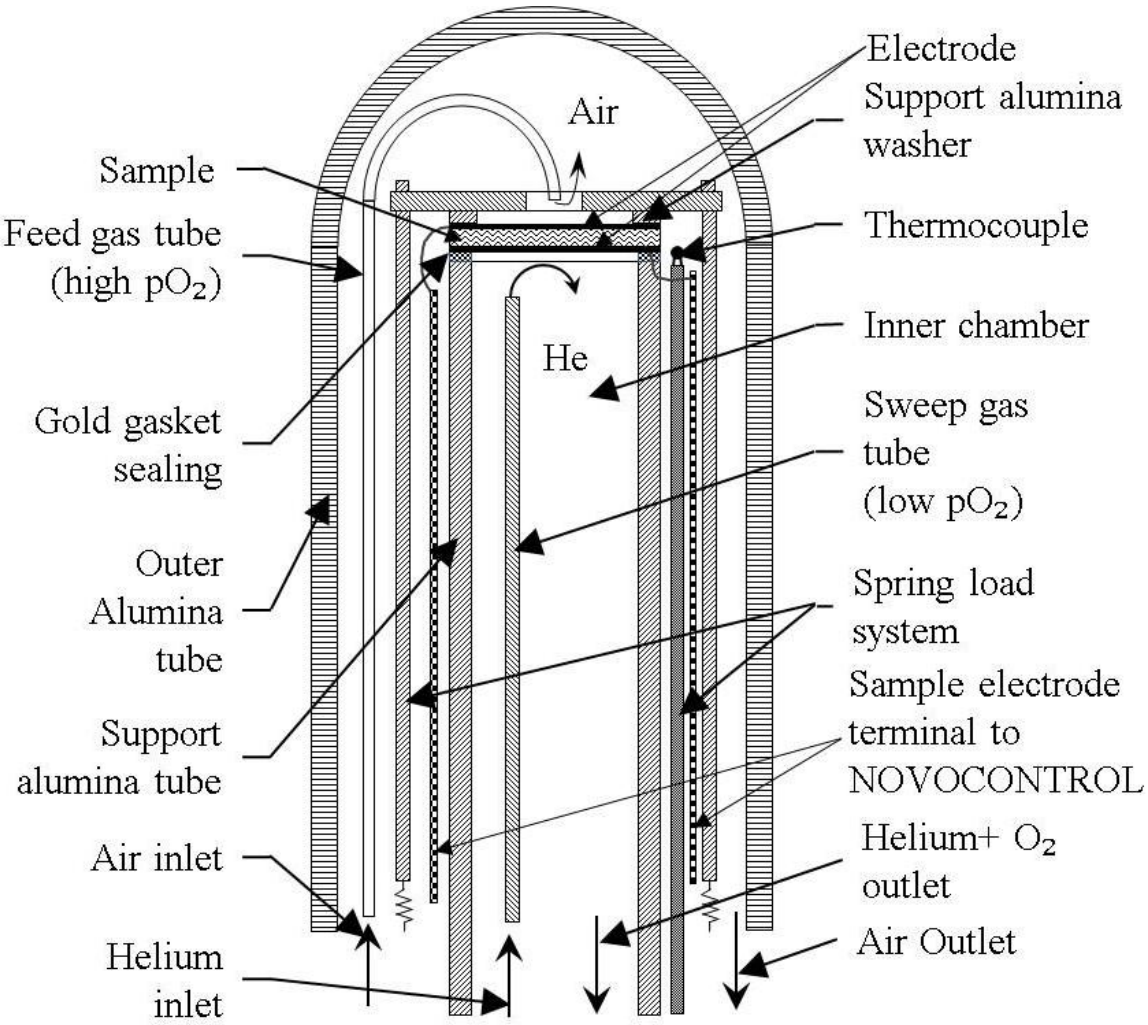

Figure 3.2. Probostat^{TM} sample stage schematic.

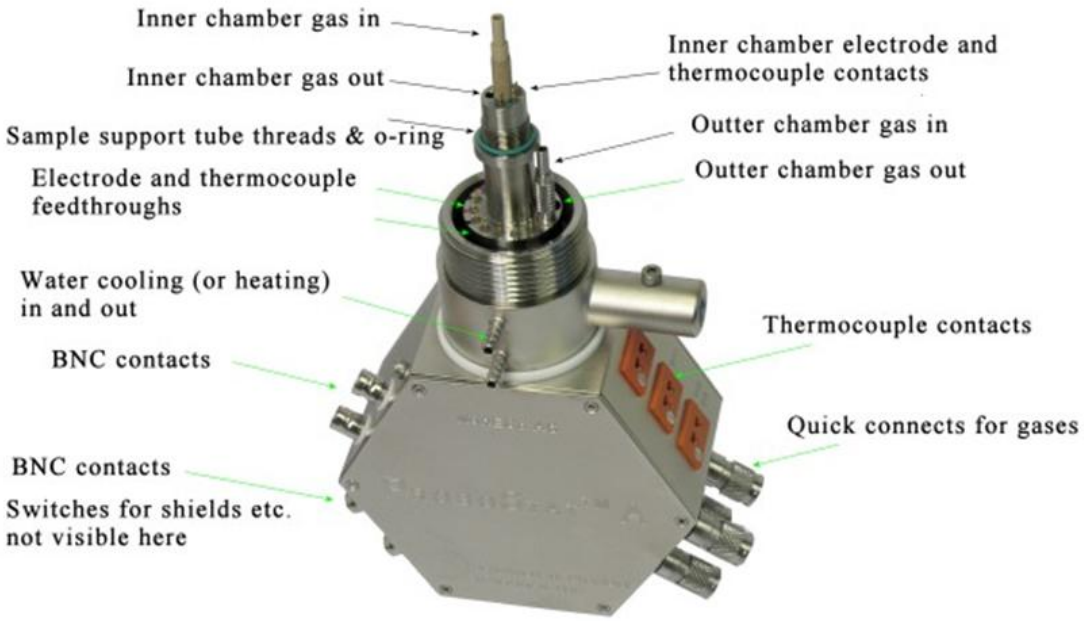

Figure 3.3. Probostat^{TM} base unit with feed throughs.

3.2.2 Gas Chromatograph (GC) Calibration

The calibration of the GC was done based on the comparison of the gas mixtures with known mole percentages of oxygen and nitrogen with the balance helium. Two-level calibration was used for this set of experiments. The two calibration gases used were 0.9943 mole percentage Nitrogen (N_2) – 0.108 mole percentage Oxygen (O_2) – Balance Helium (He) and 4.973 mole percentage N_2 – 0.99 mole percentage O_2 – Balance He. A calibration curve was generated from the two data points obtained from analyzing the two calibration gases. To analyze the unknown mixture of oxygen and nitrogen obtained from membrane permeation, the mixture was run through the GC in exactly the same way as the calibration mixtures. The GC signal response, which was the area due to the unknown amount of mixture ratio, was interpreted by means of the calibration curve to calculate the oxygen and nitrogen amounts present in the carrier gas.

The total oxygen permeated through the membrane was calculated from the mole percentage of oxygen using the total flow rate of the carrier gas. The leakage oxygen passing through the gold seal was also considered, and subtracted from the total oxygen. The gas flux was calculated using the ideal gas law and the oxygen permeation concentration.

The presence of leakage oxygen was calculated from the amount of N_2 present in the carrier gas. Leakage oxygen is the part of atmospheric air, containing both N_2 and O_2 as the main constituents with a ratio of 3.7276. So the leakage of O_2 was calculated from the total N_2 present using that ratio.

After subtracting the leakage O_2 from the total O_2, the remaining O_2 gives the permeating oxygen through the membrane. Then dividing by the total area of the active membrane area not covered by the seal determined the actual flux of O_2 through the membrane. For higher temperatures, the leakage of oxygen was less than 10% of the permeated oxygen.

3.3 Sample Characterizations

3.3.1 Constituent analysis

The microstructure of the 80GDC-20CFO sintered ceramic is shown in Figure 3.4 a), from SEM measurements. The fine, sub-micron (~500 nm) grain size observed is a consequence of the starting materials particle size in the 100nm regime. Kagomiya has previously observed changes in the oxygen permeation properties of thin film GDC-CFO membranes with changes in grain size; however this relation has not been explored in bulk materials [46]. Figure 3.4 b) depicts the backscattered SEM image along with spots indicated for chemical composition analysis.

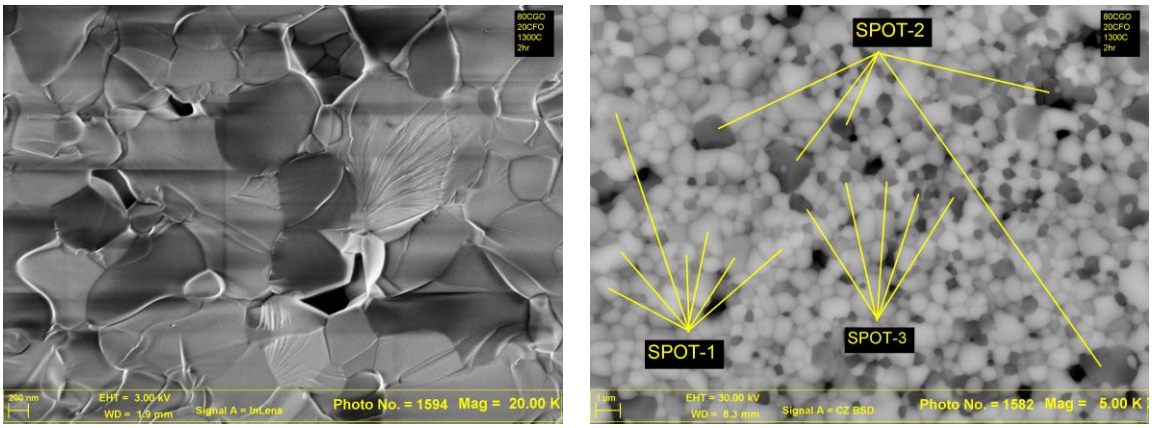

a) b)

Figure 3.4. 80GDC-20CFO Sintered at 1300°C for 2 hours: a) SEM-Secondary Electron Image b) SEM-Backscattered Electron Micrograph with spots 1 and 2 and 3 indicating EDS chemical composition analysis.

A summary of the EDS chemical composition analysis is given in Table 3.2, confirming the presence of a Gd-Fe-O phase ($GdFeO_3$ and/or $Gd_3Fe_5O_{12}$). Interfacial $GdFeO_3$ has been previously observed in this material system via high resolution TEM at the GDC-CFO interface [47].

$GdFeO_3$ is a perovskite compound with a room temperature relative permittivity of ~1000 [48], while $Gd_3Fe_5O_{12}$ is has a cubic structure with a room temperature relative permittivity of ~9 [49]. In previous reports [46], [47], the presence of $GdFeO_3$ did not have a detrimental effect on the oxygen transport, most likely due to the small quantity and location at the grain boundary interfaces. However, the location at the interface and dielectric nature of this compound may impact the measured permittivity and serve as an indicator for MIEC performance.

Table 3.2. Summary of Elements and Crystalline Phases determined from XRD measurements and EDS elemental analysis of 80GDC-20CFO Sintered sample at 1300°C for 2 hours.

Spot	Elements (Major, Minor)	Crystalline Phases*
1	O, Ce, Gd, Fe	$Ce_{0.8}Gd_{0.2}O_{1.9}$ + $Gd_3Fe_5O_{12}$ + $GdFeO_3$
2	O, Co, Fe	$CoFe_2O_4$
3	O, Ce, Gd, Fe	$Ce_{0.8}Gd_{0.2}O_{1.9}$ + $Gd_3Fe_5O_{12}$ + $GdFeO_3$

The SEM determined microstructure of the 50GDC-50CFO sintered ceramic is shown in Figure 3.4 a). Figure 3.4 b) depicts the backscattered SEM image along with spots indicated for chemical composition analysis.

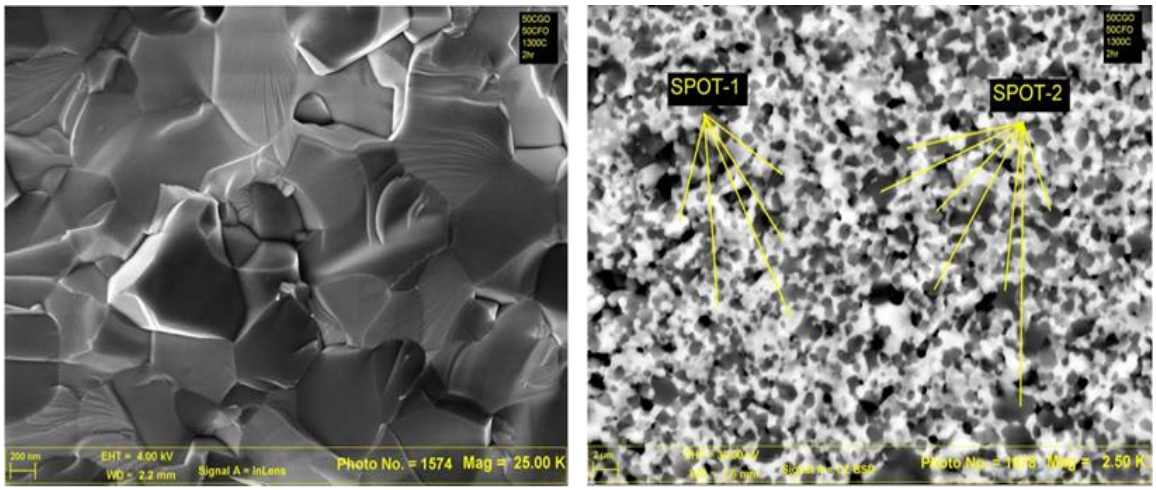

Figure 3.5. 50GDC-50CFO Sintered at 1300°C for 2 hours: a) SEM-Secondary Electron Image b) SEM-Backscattered Electron Micrograph with spots 1 and 2 indicating EDS chemical composition analysis.

A summary of the EDS chemical composition analysis for the 50GDC-50CFO is given in Table 3.3, confirming the presence of a Gd-Fe-O phase ($GdFeO_3$ and/or $Gd_3Fe_5O_{12}$).

Table 3.3. Summary of Elements and Crystalline Phases determined from XRD measurements and EDS elemental analysis of 50GDC-50CFO Sintered sample at 1300°C for 2 hours.

Spot	Elements (Major, Minor)	Crystalline Phases*
1	O, Ce, Gd, Fe	$Ce_{0.8}Gd_{0.2}O_{1.9}$ + $GdFeO_3$
2	O, Co, Fe	$CoFe_2O_4$

3.3.2 X-ray Diffraction (XRD) analysis

Phase identification was performed by X-ray diffraction analysis by surface scan done on the three different volume fraction mixtures. Figure 3.6 shows XRD pattern for a 50GDC-50CFO sintered at 1300˚C for 2 hours.

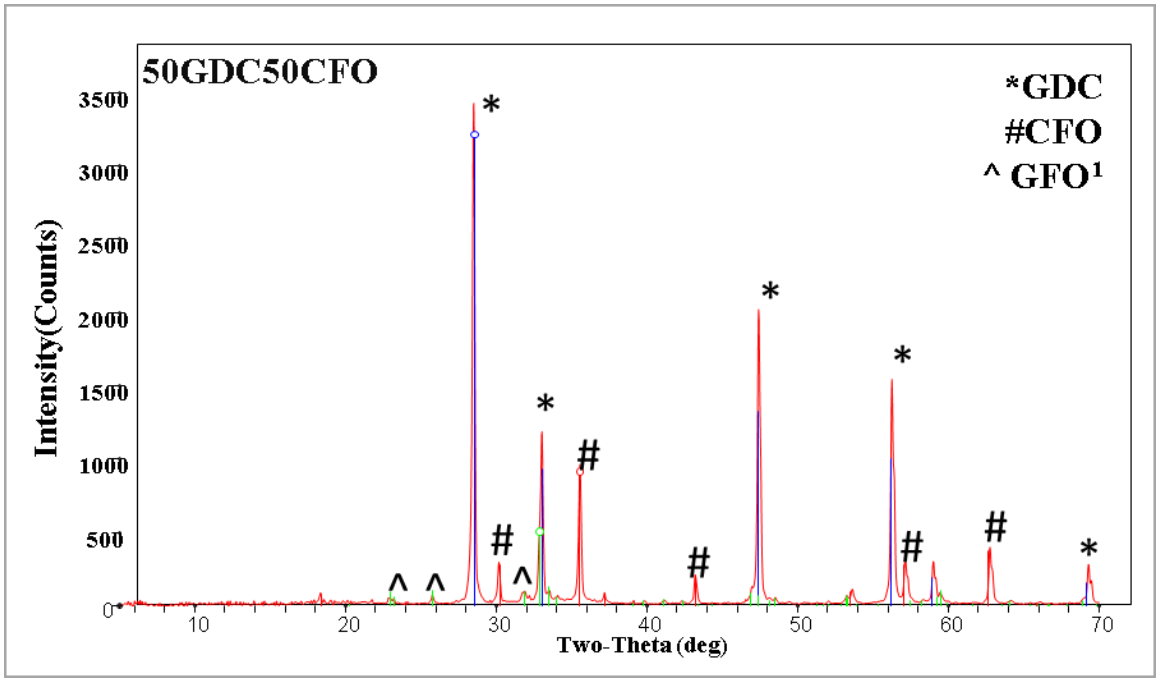

Figure 3.6. X-ray diffraction spectra of 50GDC-50CFO mixtures, calcined in air at temperatures from 1000-1300°C for 2 hours.

As expected the sample had GDC ($Ce_{0.8}Gd_{0.2}O_{1.9}$) and CFO ($CoFe_2O_4$) phases. There was the emergence of a third phase which was tentatively identified by select diffraction peaks and EDX chemical analysis as gadolinium ferrite $GdFeO_3$ (GFO[1]) which was generated during the sintering process.

X-ray diffraction spectra shown in Figure 3.7 for the 60GDC-40CFO sample sintered at 1300°C for 2 hours also show presence of GDC and CFO as well as the third oxide phase $GdFeO_3$ similar to the 50GDC-50CFO sample.

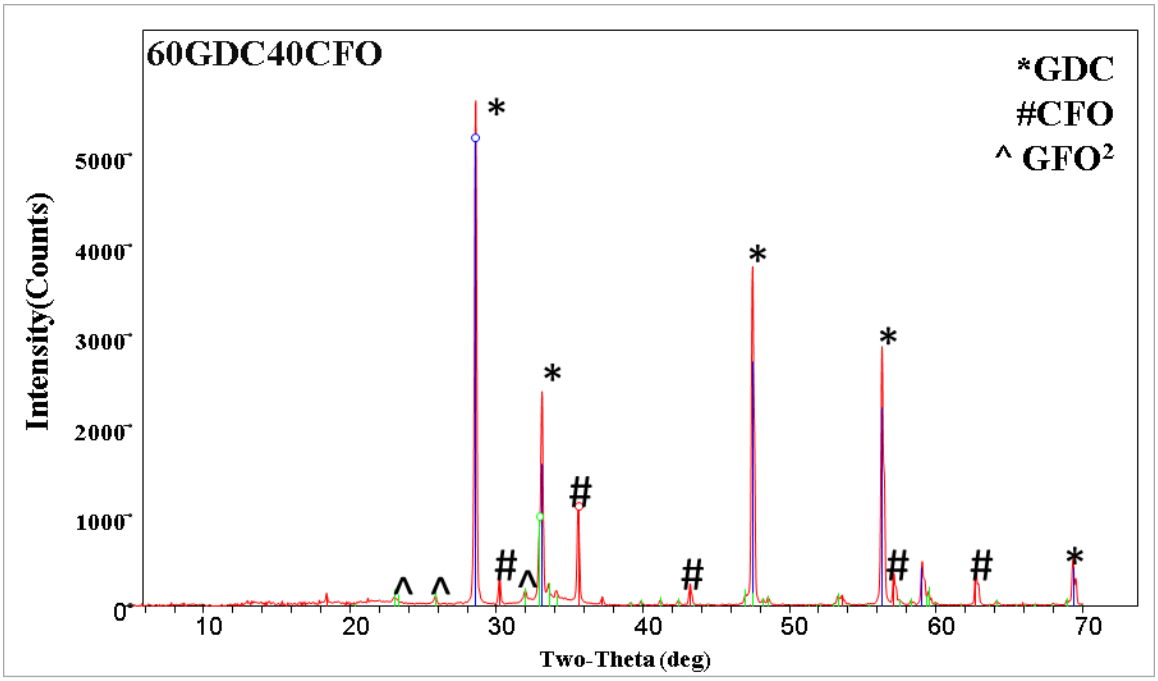

Figure 3.7. X-ray diffraction spectra of 60GDC-40CFO mixtures, calcined in air at temperatures from 1000-1300°C for 2 hours.

The X-ray diffraction pattern for the 80GDC-80CFO sample sintered at 1300°C had the two GDC and CFO phases. But it had a different form of gadolinium ferrite different than the gadolinium ferrite present in the previous two samples. EDS analysis of the sample confirms the third oxide phase is a gadolinium ferrite with the composition of $Gd_3Fe_5O_{12}$.

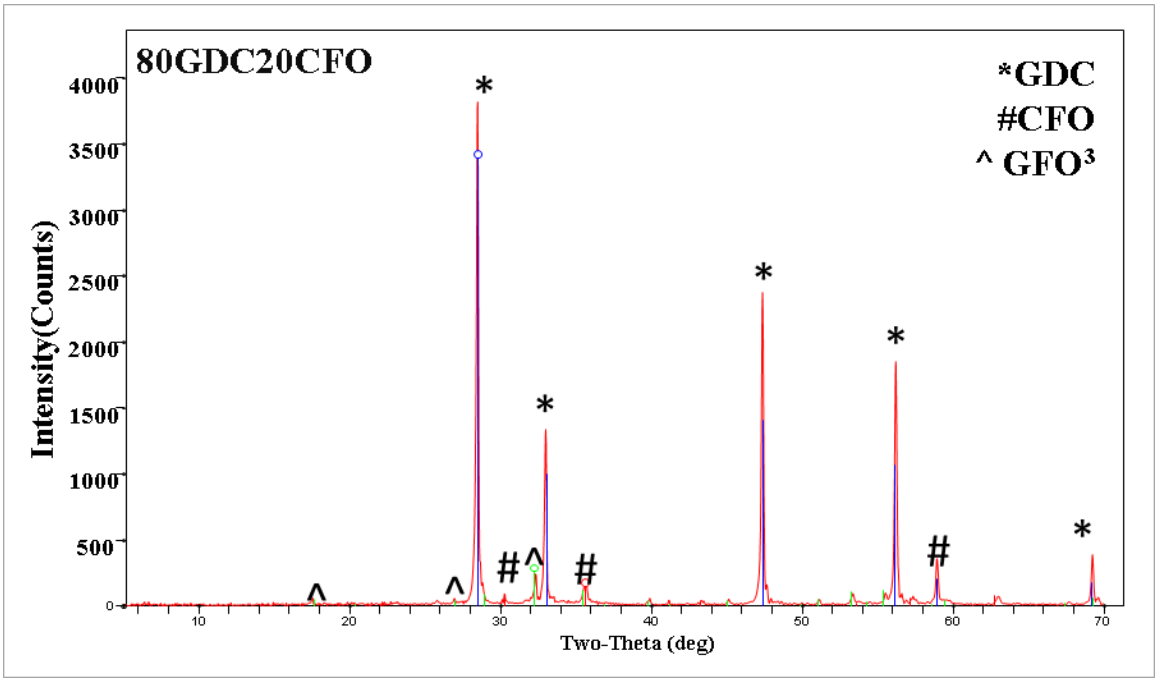

Figure 3.8. X-ray diffraction spectra of 80GDC-20CFO mixtures, calcined in air at temperatures from 1000-1300^{o}C for 2 hours.

Figure 3.8 shows the XRD pattern of the 80GDC-20CFO sample with the different phases marked. Figure 3.9 shows a combined representation of the XRD pattern of the single phases: GDC, CFO and the three mixture samples.

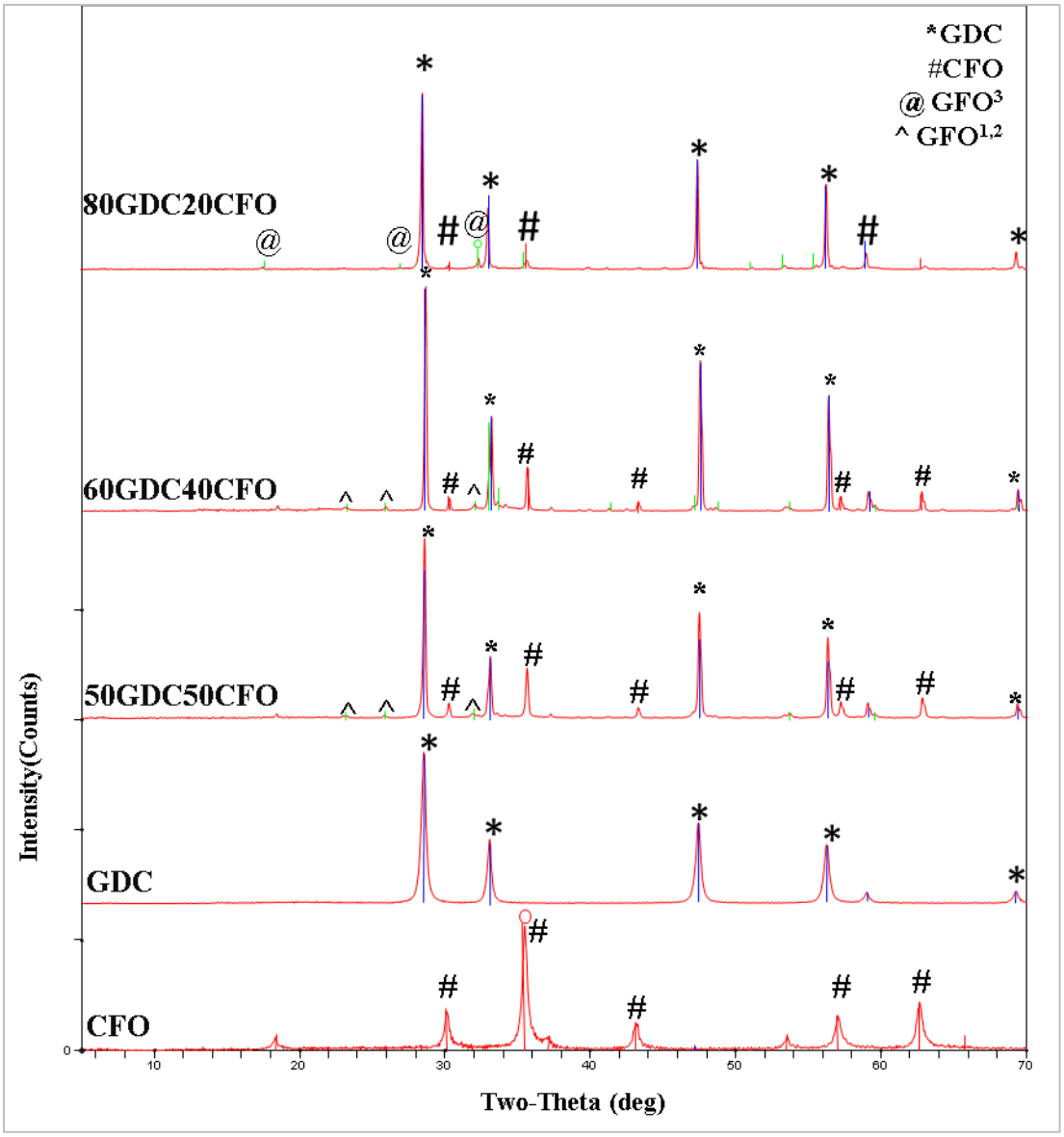

Figure 3.9. X-ray diffraction pattern for a) gadolinium doped ceria (GDC), b) cobalt ferrite (CFO), c) 80%GDC-20%CFO, d) 60%GDC-40%CFO and e) 50%GDC-50%CFO.

3.3.3 Surface degradation

The operation cycle is shown in Figure 3.10 is showing the time required for the sealing and flux measurement for each temperature steps.

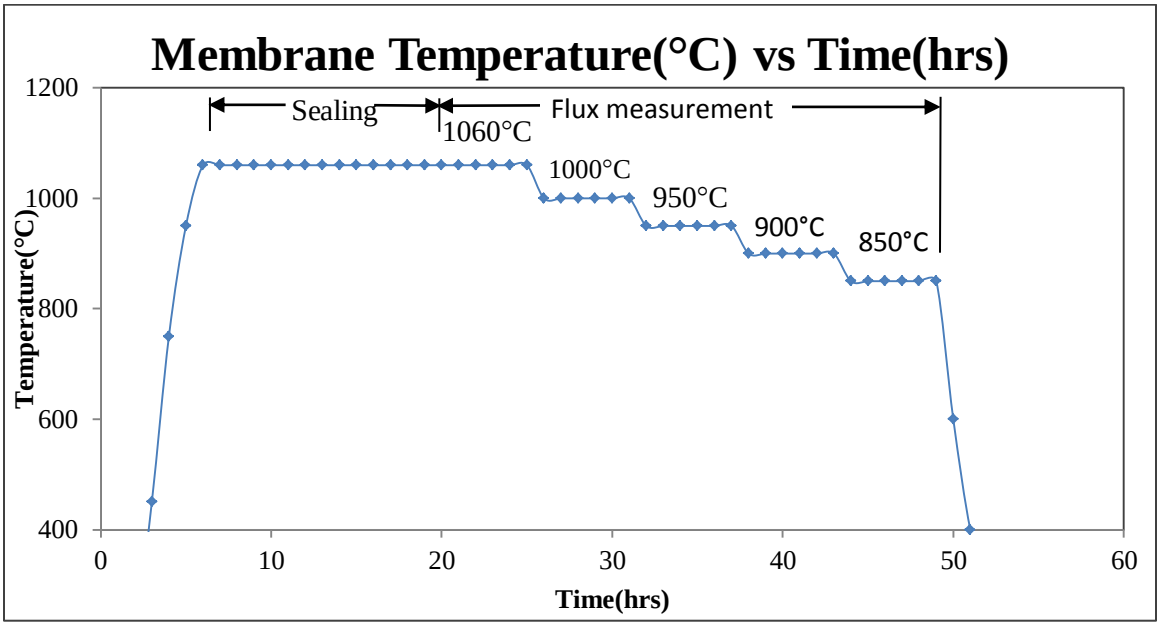

Figure 3.10. Temperature vs Time (hours) showing operating condition over operating ime period of the membrane.

The gold sealing was made at a temperature of 1060°C for 20-24 hours. The flux measurements were taken from 850°C to 1060°C and the total time required for the measurements were 50-60 hours. So each sample was operated for 70-75 hours. SEM images of the polished surface of the fresh membranes and degraded surface of both side: air side and permeate side of the used samples were taken to compare degradation on the two sides of each sample as well as degradation on the surface between different mixture samples.

Figure 3.11(a) shows the surface of the fresh 50%GDC-50%CFO perovskite membrane. The grain size is not uniform, and was distributed from 0.1 μm to around

3μm. Figure 3.11(b) and 3.11(c) shows the two surfaces of the membrane after 70hour-75hour operation. The surface of the perovskite membrane on the permeate side (helium sweep side) shown in figure 3.11(c) had significantly higher degradation compared to the feed side (air side) shown in figure 3.11(b).

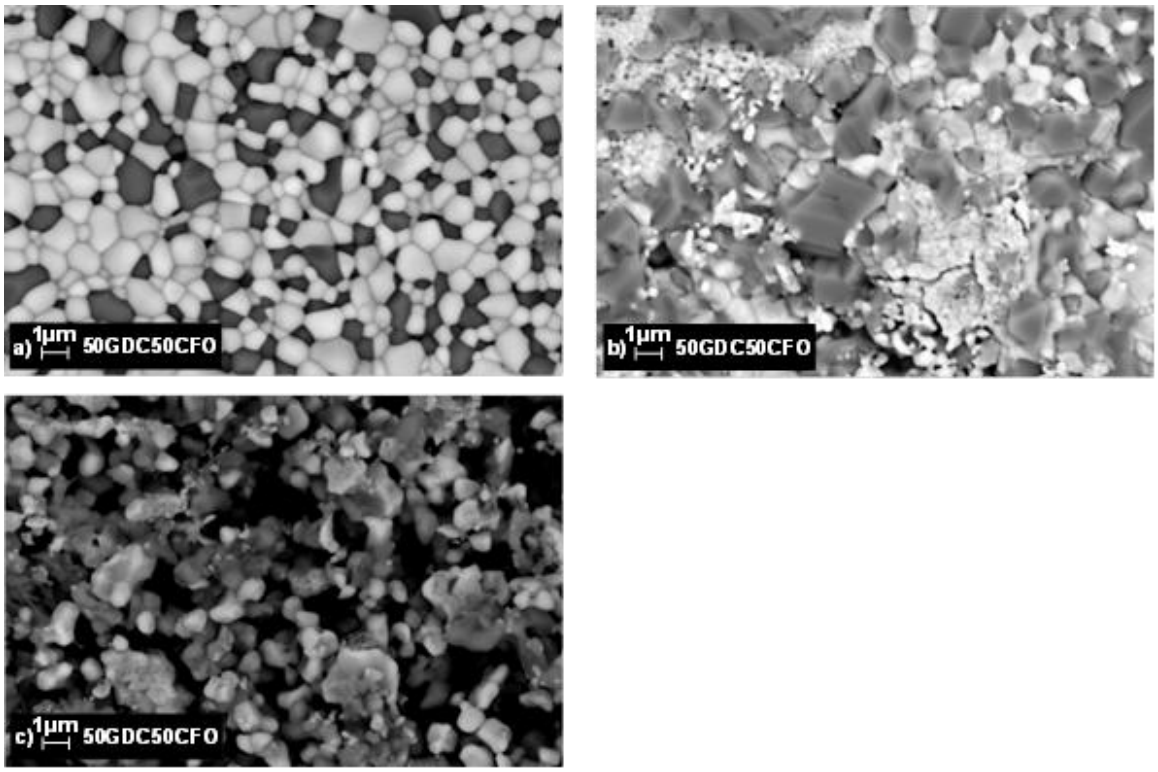

Figure 3.11. Scanning electron micrographs showing microstructure of the 50%GDC-50%CFO perovskite membrane: a) Fresh polished membrane surface as fabricated, b) Air Side surface and c) permeate side surface.

For the 60%GDC-40%CFO mixture membrane the scanning electron micrograph shows a grain size from 0.2 μm to 4μm shown in figure 3.12(a). Degradation on the permeation side is significantly high compared to the air side shown in figure 3.12(c) and 3.12(b) respectively, similar to the 50%GDC-50%CFO sample.

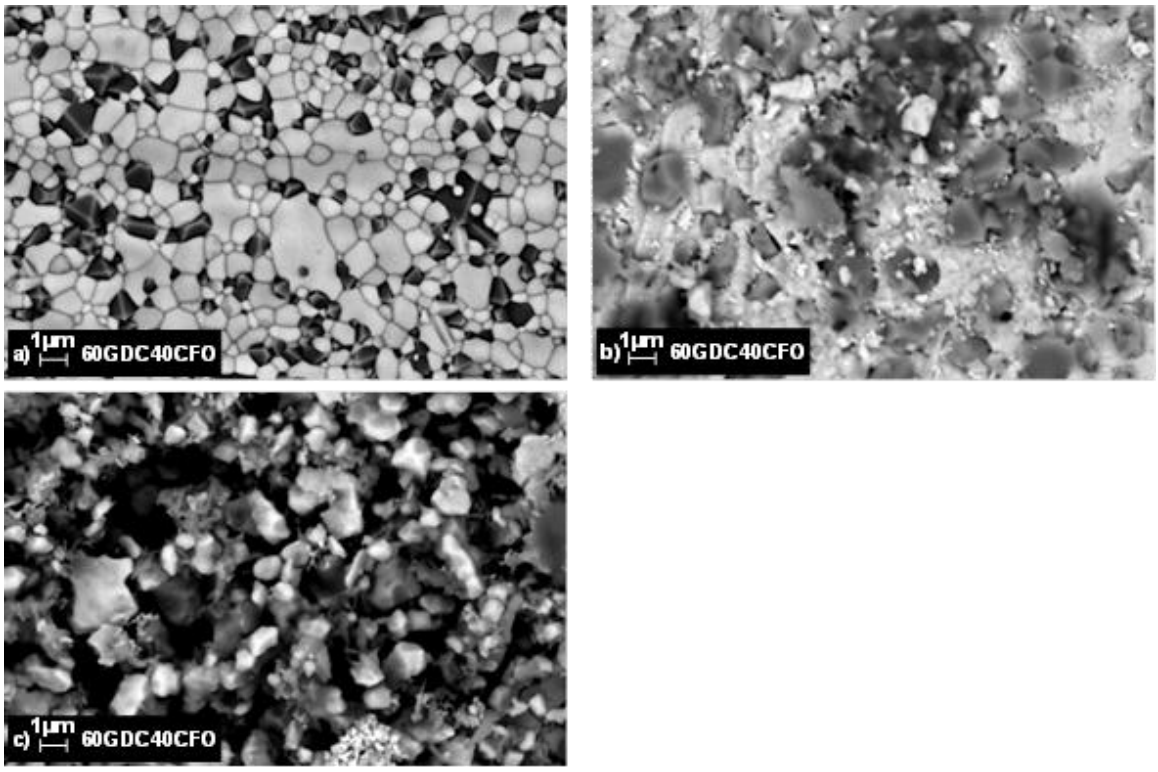

Figure 3.12. Scanning electron micrographs showing microstructure of the 60%GDC-40%CFO perovskite membrane: a) Fresh polished membrane surface as fabricated, b) feed surface and c) permeate side surface, after 75 hours of operation at operating temperature from 850˚C to 1060˚C.

80%GDC-20%CFO sample characteristics for the fresh and used samples are shown in figure 3.13(a), 3.13(b) and 3.13(c) exhibiting degradation on either side similar to the above two samples.

Comparison of the permeate side of the three membranes shown in Figures 3.11(c), 3.12(c) and 3.13(c) shows that the permeate side of the 50%GDC-50%CFO membrane has the most degradation and the 80%GDC-20%CFO sample has the least degradation, and this can be attributed to the fact that GDC has a higher sintering temperature at 1500°C compared to the sintering temperature of CFO sintered at 1100°C-1200°C.

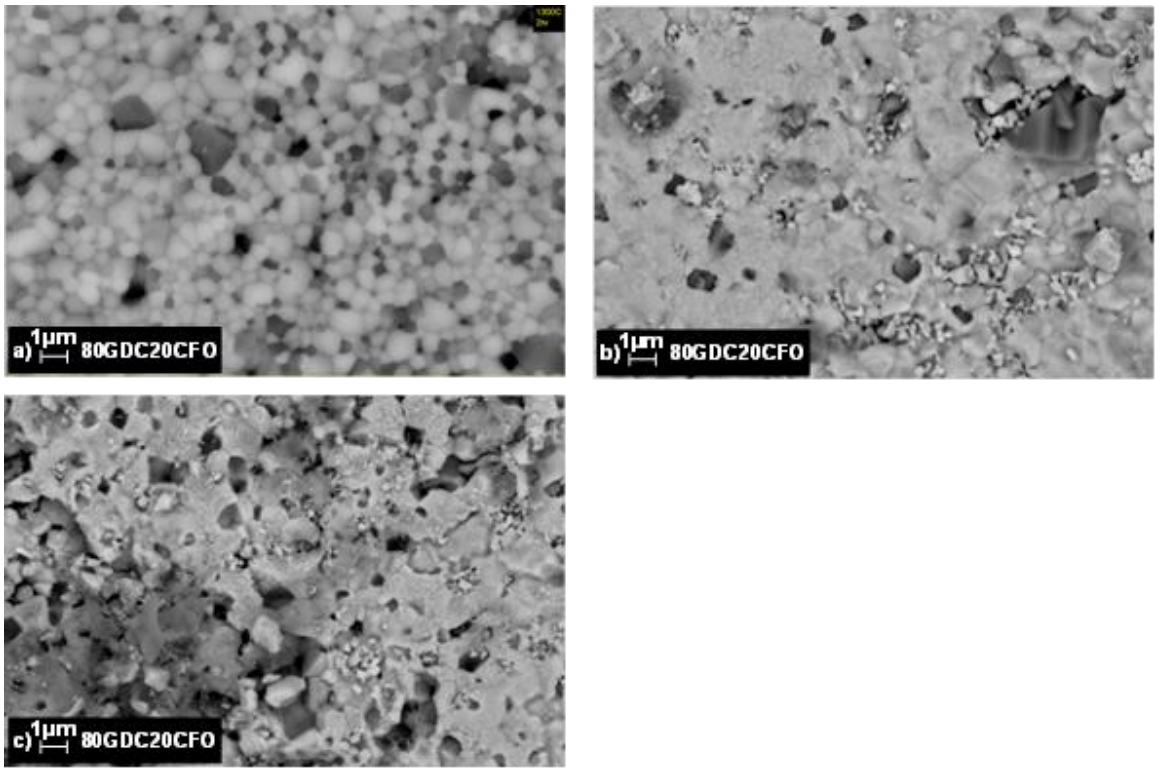

Figure 3.13. Scanning electron micrographs showing microstructure of the 80%GDC-20%CFO perovskite membrane: a) Fresh polished membrane surface as fabricated, b) Air Side surface and c) permeation side surface**.**

Thus with increase in the electronic phase of CFO, the degradation in the permeate surface is increased as the membrane is operated at a higher temperature. This also effects the surface properties of the system.

3.4 Permeation

From the SEM microstructural study, we observed that for different mixture ratio the size of the grains varied. Different sintering condition also influenced the grain size and microstructure of the membranes. These effects of volume fraction, sintering condition and microstructure on overall flux were studied systematically varying different parameters. The effect of partial pressure on the overall permeation flux was studied in these experiments by varying flow rate of sweep gas.

3.4.1 Effect of Volume Fraction

For the volume fraction study, three sets of samples with varied volume fraction were made. The three sets were- 50%GDC-50%CFO, 60%GDC-40%CFO and 80%GDC-20%CFO. These samples were synthesized using the same sintering conditions. Two such sintering conditions were used to make two groups, one with a 1300°C sintering temperature for two hours, and one with a 1300°C sintering temperature for five hours. Different sintering conditions created microstructural variations in the sample groups. For the 80%GDC-20%CFO composition, another sintering condition of 1400°C for two hours was used. Flux was measured over a temperature range from 850°C-1060°C with 50°C increments.

Figure 3.14 shows measured flux vs temperature for three different volume fraction samples sintered in 1300˚C for 2 hours.

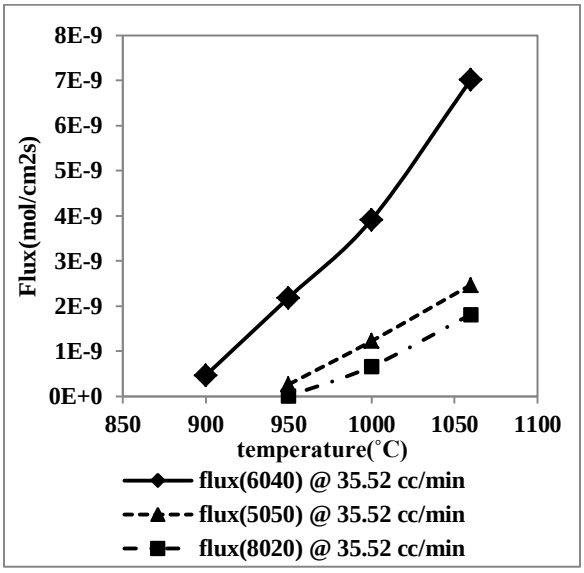

Figure 3.14. Flux variation for different volume fraction samples sintered at 1300˚C for 2 hours measured for operating temperature from 850˚C to 1060˚C and 35.52 cc/min sweep gas flow rate.

In this case an intermediate volume fraction mixture (60%GDC-40%CFO) had a higher permeation flux compared to the other two mixtures. This behavior is thought to be related to the emergence of the third phase of Gadolinium Iron Oxide that we observed from the XRD data previously discussed. Figure 3.15 shows flux vs. temperature for the three different volume fraction samples sintered in the same sintering temperature of 1300˚C but for a longer time of 5 hours. In this case also the intermediate mixture of 60%GDC-40%CFO has a higher value of flux compared to the other two mixtures indicating the consistency of this behavior.

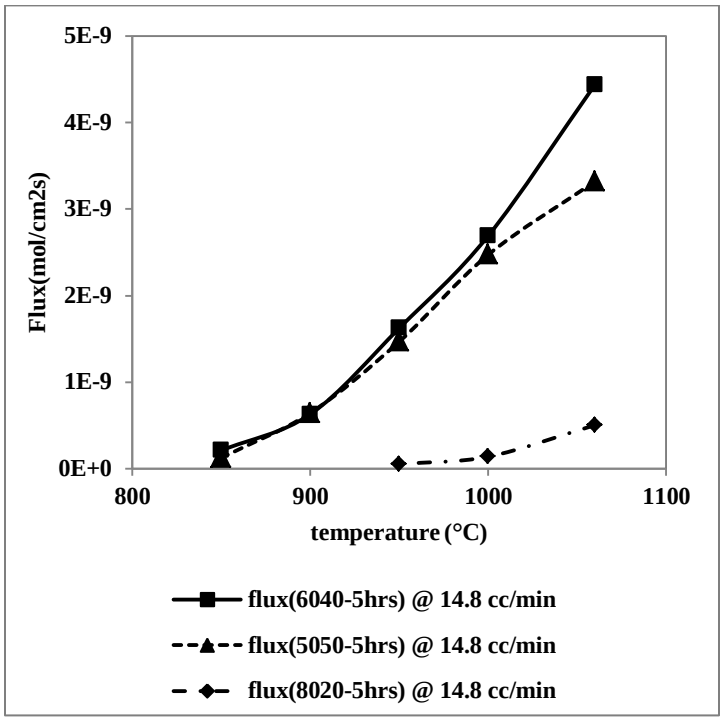

Figure 3.15. Flux variation for different volume fraction samples sintered at 1300˚C for 5 hours measured for operating temperature from 850˚C to 1060˚C and 14.8 cc/min sweep gas flow rate.

3.4.2 Effect of Microstructure

For microstructural variations, two different sintering conditions, 1300˚C for 2 hours and 1300˚C for 5 hours were used for the three different mixture samples. An additional sintering condition of 1400˚C for 2 hours was used.

Figure 3.16. Microstructural variations for 60%GDC-40%CFO sample sintered at 1300˚C for a) 2 hours and b) 5 hours.

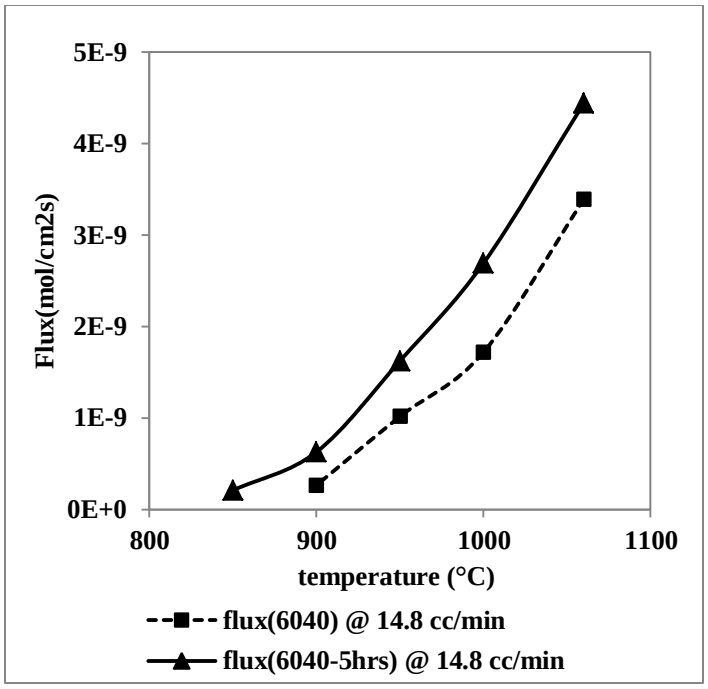

Figure 3.17. Flux variation for varied microstructure of 60GDC-40CFO mixture. Microstructure variation obtained by using two different sintering conditions (1300°C for 2 hours and 1300°C for 5 hours) measured for operating temperature from 850˚C to 1060˚C and 14.8 cc/min sweep gas flowrate.

Figures 3.16 shows scanning electron micrographs of the microstructural variation of the 60%GDC-40%CFO originated from the different sintering time with longer sintering time increasing the grain size of each phases. Figure 3.17 and shows sample with longer sintering time and larger grain size has higher flux.

Similarly for the 50%GDC-50%CFO sample longer sintering time produces large grains and increased flux shown in Figures 3.18 and 3.19. In addition, the formation of GdFe phases during sintering suggest that at increased temperature and longer duration of sintering may impact both the character of the starting materials and the emergent GdFe phase with implications for oxygen transport in the materials system.

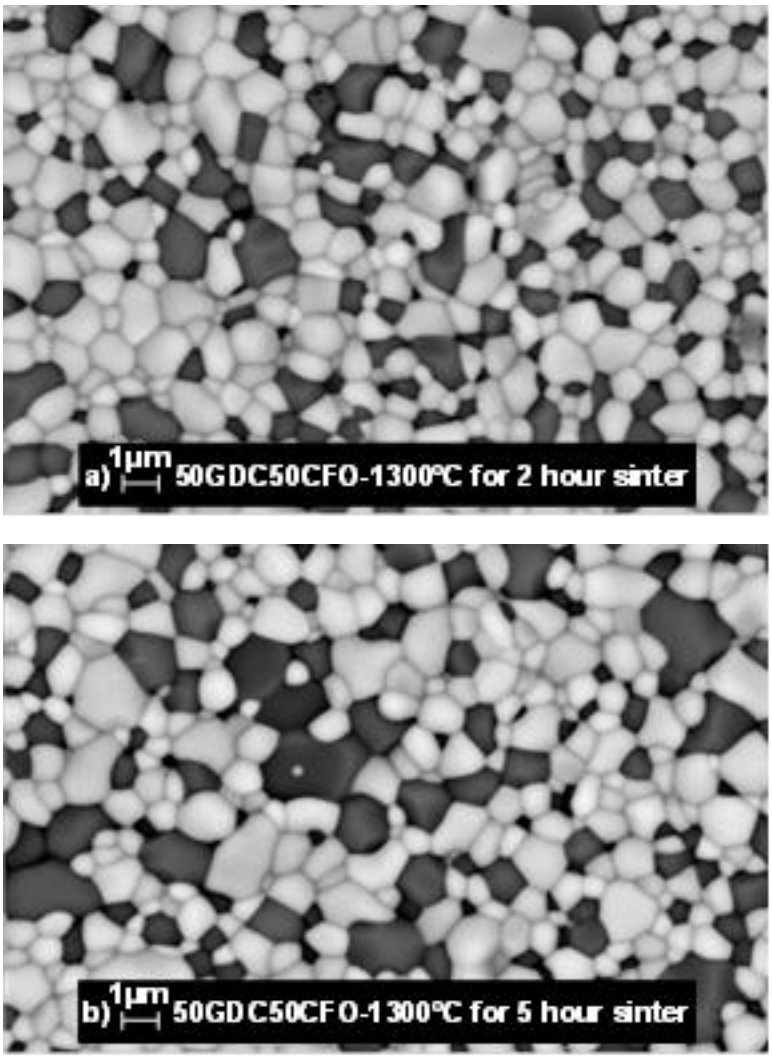

Figure 3.18. Microstructural variations for 50%GDC-50%CFO sample sintered at 1300˚C for a) 2 hours and b) 5 hours.

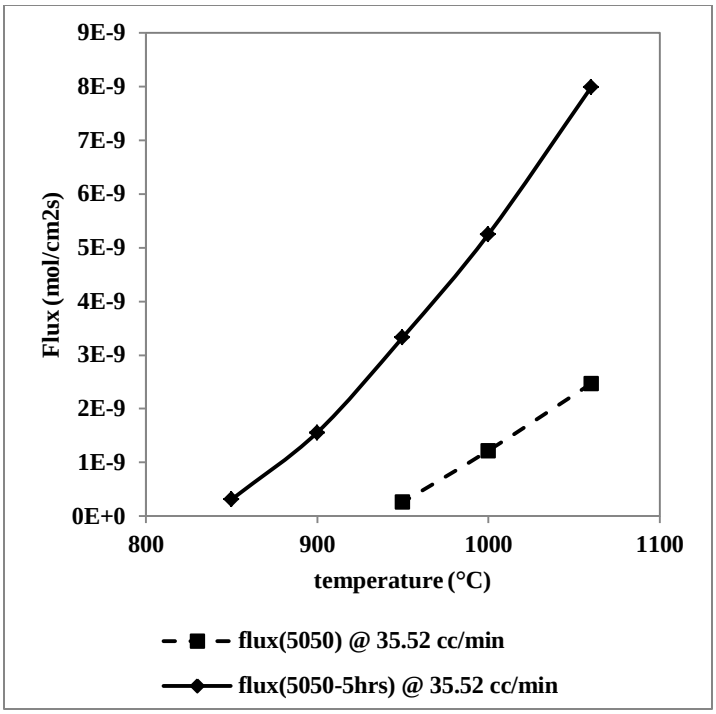

Figure 3.19. Flux variation for varied microstructure of 50GDC-50CFO mixture. Microstructure variation obtained by using two different sintering conditions (1300°C for 2 hours and 1300°C for 5 hours) measured for operating temperature from 850˚C to 1060˚C and 14.8 cc/min sweep gas flowrate.

For the 80%GDC-20%CFO sample an additional sintering condition of 1400˚C for 2 hours was used which gave even larger grain boundary size and increased flux compared to the samples sintered in 1300˚C temperature shown in Figures 3.20 and 3.21.

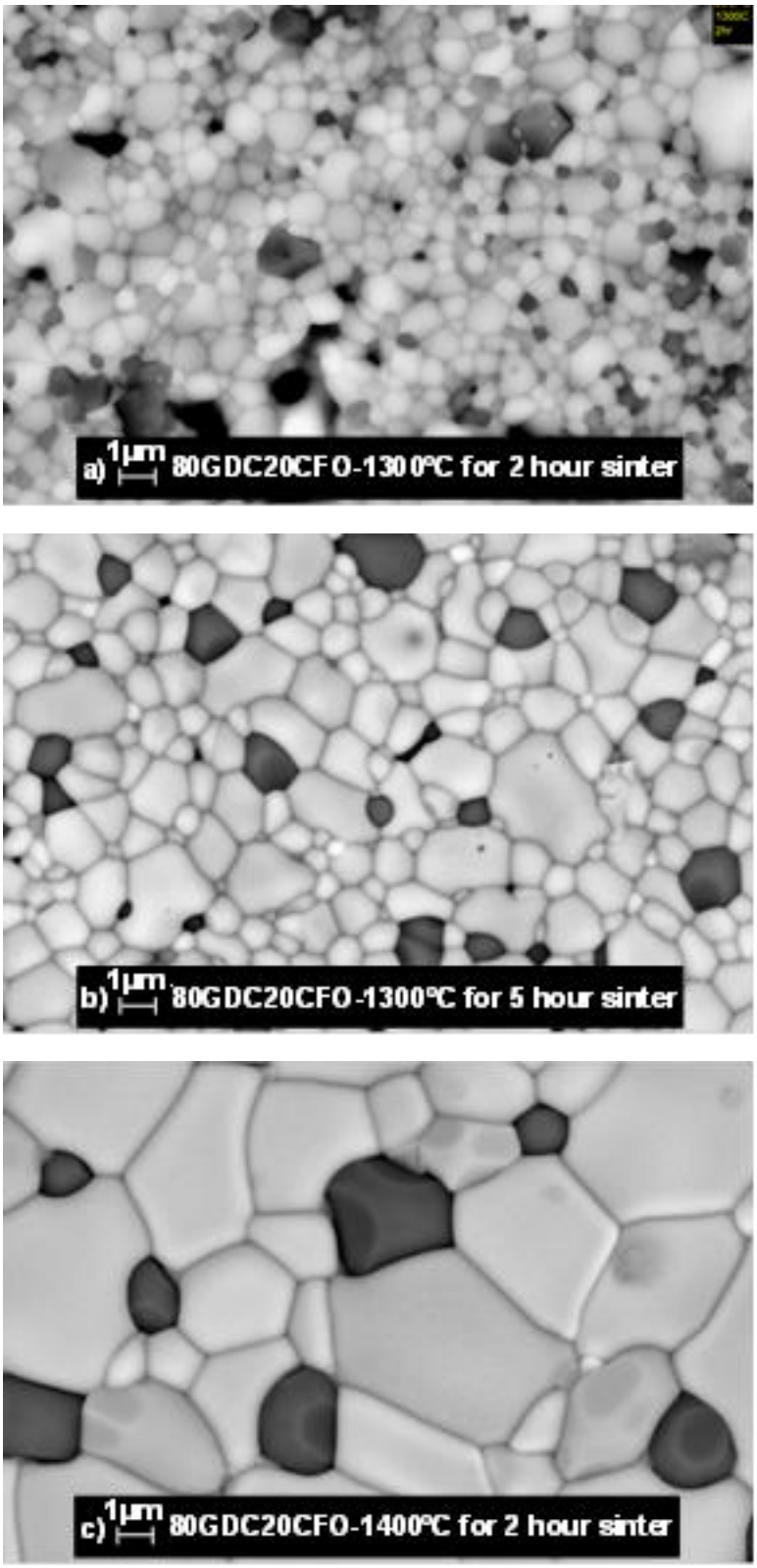

Figure 3.20. Microstructural variations for 80%GDC-80%CFO sample sintered at a) 1300˚C for 2 hours, b) 1300˚C for 5 hours and c) 1400˚C for 2 hours.

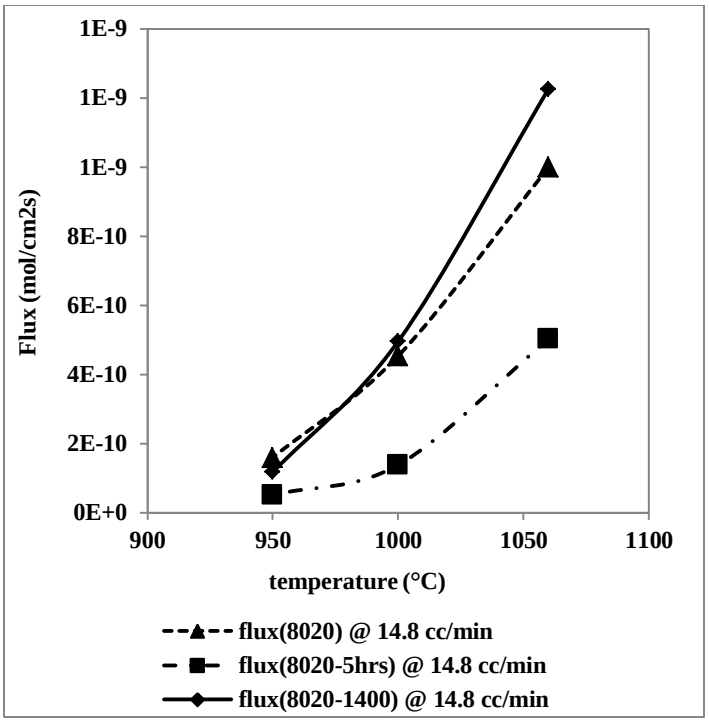

Figure 3.21. Flux variation for varied microstructure of 80GDC-20CFO mixture. Microstructure variation obtained by using three different sintering conditions (1300°C for 2 hours, 1300°C for 5 hours and 1400°C for 2 hours) measured for operating temperature from 850˚C to 1060˚C and 14.8 cc/min sweep gas flow rate.

3.4.3 Effect of platinum surface layer

Effect of a platinum paste electrode was studied by comparing the flus values of membranes with and without platinum paste surface layers. Improved oxygen flux has been reported by Murphy et. al. where they enhanced the flux by applying platinum layer on top of the sample[50], [51]. In our study a thin layer of platinum paste was applied using brush and sintered at 800°C temperature. Flux measurements were taken from 850°C-1060°C for a constant flow rate of 35.52cc/min.

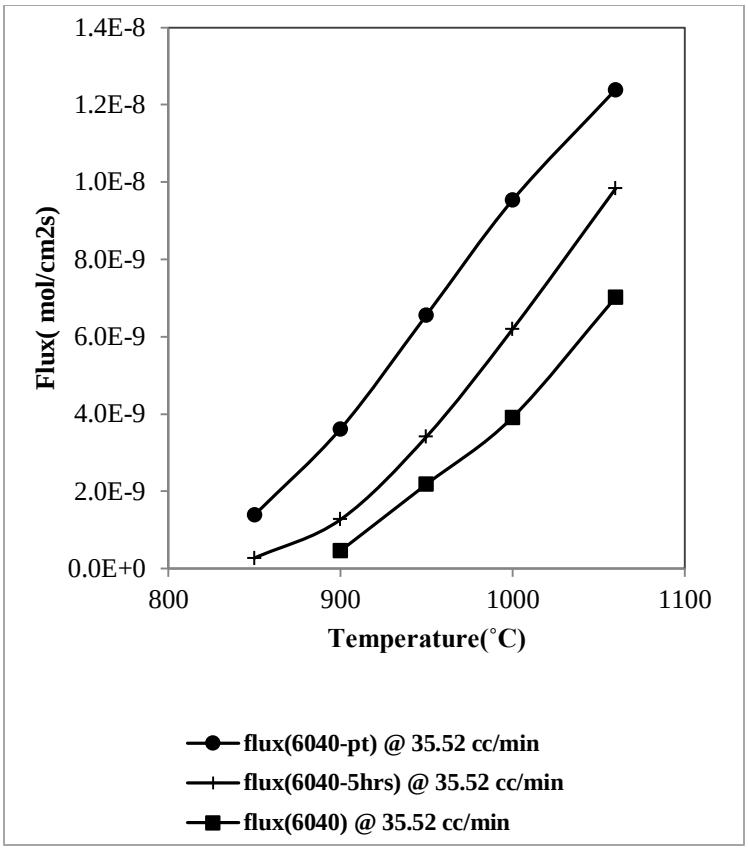

Figure 3.22. Flux comparison for use of platinum paste on 60% GDC-40%CFO sample, measured for operating temperature from 850˚C to 1060˚C and 35.52 cc/min sweep gas flowrate.

Figure 3.22 shows measured flux for variation of the 60GDC-40CFO mixture, i) sintered at 1300°C for 2 hours with plain surface, ii) sintered at 1300°C for 5 hours with plain surface and iii) sintered at 1300°C for 2 hours with platinum surface layer. And the plot indicates membrane with the platinum surface layer has the highest oxygen flux. The increase of flux with platinum surface layer can be originated from catalytic behavior of platinum. Also porosity of the platinum layer increases the surface area of the membrane surface and thus increasing surface activity of the membrane resulting in flux increase.

3.4.4 Flux equation comparison

In Figure 3.23, comparison between measured fluxes of MIEC membranes were made with calculated flux for the same mixture predicted from Wagner's equation.

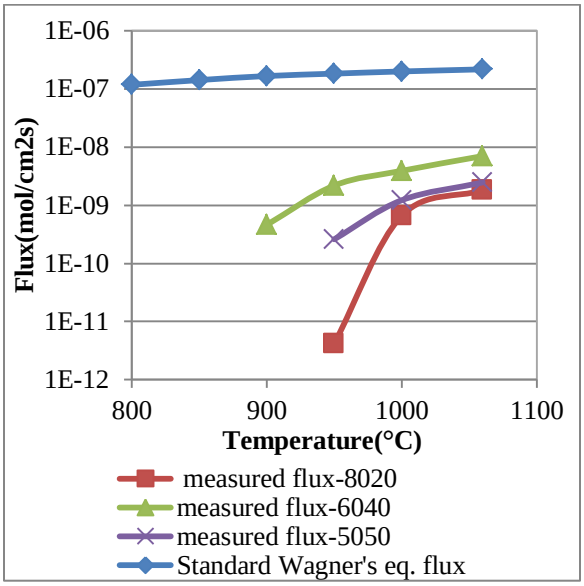

Figure: 3.23. Flux comparison between experimental and calculated flux using Wagner's equation.

For the Wagner's equation, we used total conductivity of the ionic phase GDC and electronic phase CFO from the measured value we obtained shown in Table 4.2 discussion in Section **4.5.3.** Here we can see that the calculated flux is much higher compared to the actual flux, and since it does not take into account the volume fraction of each phase, no individual prediction can be made for each of the volume fraction mixtures. So modification can be made based on the MPM model shown in Equation (2-13). For this case, we will assume for the three mixtures - 80GDC-20CFO, 60GDC-40CFO and 50GDC-50CFO, the value of k varies from 0.7-0.5 and the value of λ varies from 0.3-0.25. More accurate values of these constants will be obtained by the x-ray nanotomography techniques mentioned earlier from the works of Nelson et. al. [45].

Figure 3.24 illustrates a comparison between calculated flux from the modified Wagner's equation and actual flux. This time, using Equation (2-13), we could incorporate the volume fractions into the prediction.

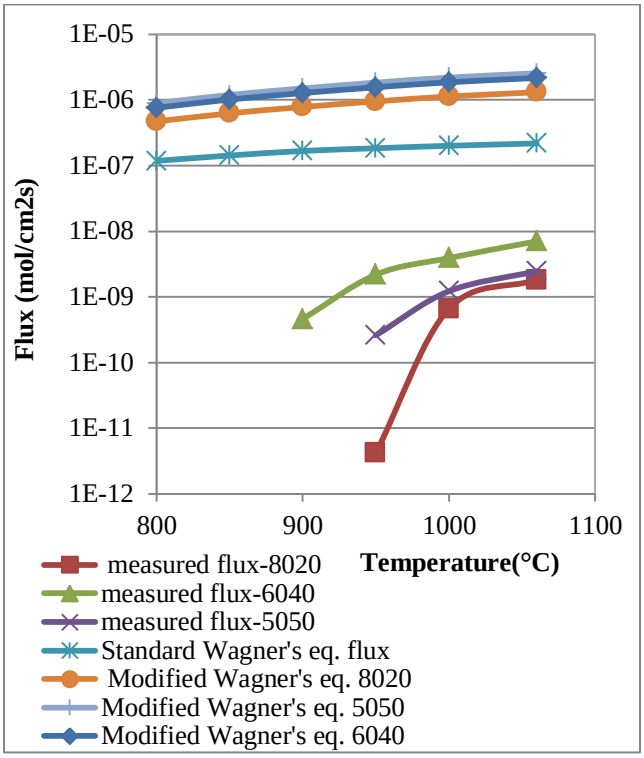

Figure 3.24. Flux comparison between experimental and calculated flux using modified Wagner's equation.

Here we see the modified equation calculates even higher flux compared to the standard Wagner's equation. Also the 50GDC50CFO has the highest flux which does not match the experimental result wherein 60GDC40CFO – an intermediate mixture has the highest flux. So in our subsequent work we will modify the Wagner's equation taking into account the emergent third phase, surface activity and calculated values of k and λ obtained from the 3D nanotomography (or other) study.

CHAPTER 4

BROADBAND DIELECTRIC SPECTROSCOPY (BbDS)

Broadband dielectric spectroscopy is the interaction of electromagnetic waves with matter in the frequency range from a lower 10^{-6} Hz to a higher frequency of 10^{12} Hz. This dynamic range contains information about the molecular and collective dipolar fluctuation; charge transport and polarization effects occur at inner and outer boundaries in the form of different dielectric properties of the material under study. Figure 4.1 shows the effect of different charge displacement mechanisms on dielectric response and their corresponding effective frequency range.

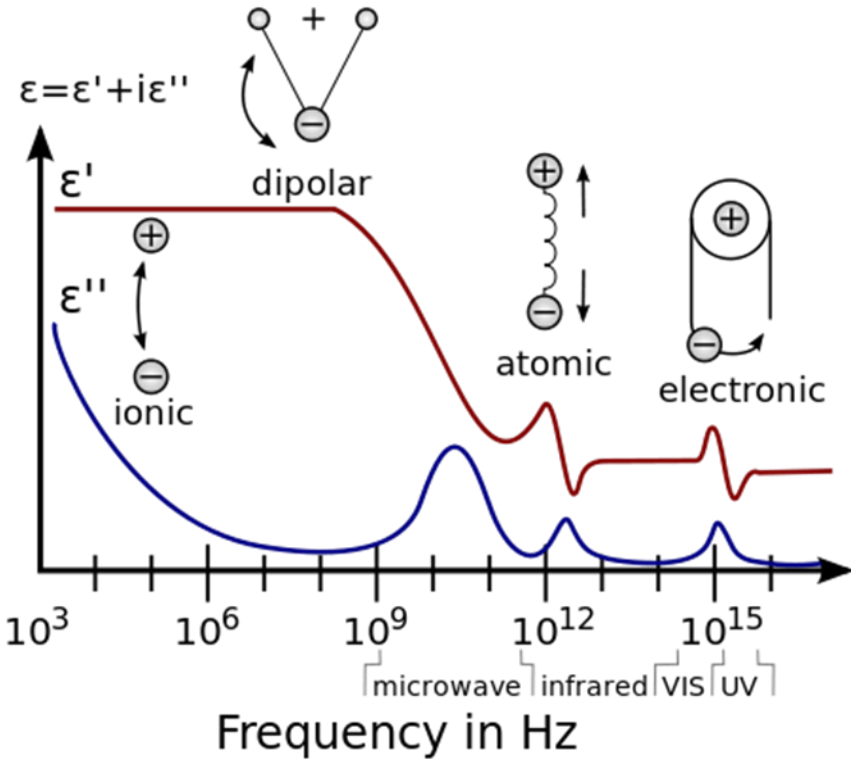

Figure 4.1. Dielectric responses of material constituents at broad band frequency range.

Hence broadband dielectric spectroscopy can be used as a useful tool to obtain a wealth of information on the dynamics of bound dipoles and mobile charge carriers depending on the details of the molecular system.

4.1 Maxwell's equations

Electromagnetic phenomena can be described by four equations which are called Maxwell equations [52].

$$\nabla.\vec{\mathbf{D}}=\rho \tag{4-1}$$

$$\nabla\times\vec{\mathbf{H}}=\vec{j}+\frac{\partial\vec{\mathbf{D}}}{\partial t} \tag{4-2}$$

$$\nabla\times\vec{\mathbf{E}}+\frac{\partial\vec{\mathbf{B}}}{\partial t}=0 \tag{4-3}$$

$$\nabla.\vec{\mathbf{B}}=0 \tag{4-4}$$

Here $\vec{\mathbf{D}}$ is the dielectric displacement, ρ is the charge density, $\vec{\mathbf{H}}$ magnetic field, $\vec{\mathbf{E}}$ electric field, $\vec{\mathbf{B}}$ magnetic induction and $\vec{j}$ is the ohmic current density. In addition to Maxwell's equations, the field must satisfy continuity equations based on the charge density ρ and current density $\vec{j}$ which can be expressed as follows

$$\nabla.\vec{j}+\frac{\partial\rho}{\partial t}=0 \tag{4-5}$$

The interrelation between the dielectric displacement $\mathbf{D}^{\rightarrow}$ and electric field $\vec{\mathbf{E}}$ can be expressed as for linear materials.

$$\vec{\mathbf{D}}=\varepsilon_0\vec{\mathbf{E}}+\vec{\mathbf{P}} \tag{4-6}$$

And polarization can be related to the charge density when no external source is present by the following equation

$$\nabla.\vec{\mathbf{P}}=-\rho \tag{4-7}$$

For a linear relationship between the dielectric displacement $\vec{\boldsymbol{D}}$ and electric field $\vec{\boldsymbol{E}}$ the proportionality constant ε can be used to express

$$\vec{\mathbf{D}}=\varepsilon\varepsilon_0\vec{\mathbf{E}} \tag{4-8}$$

Here the constant ε is called the permittivity of the material which describes the dielectric behavior. When the Polarization is $\vec{\mathbf{P}}$ is taken into consideration using (4-6) and (4-8) we obtain

$$\vec{\mathbf{P}}=\chi\varepsilon_0\vec{\mathbf{E}}\equiv\varepsilon_0(\varepsilon-1)\vec{\mathbf{E}} \tag{4-9}$$

Here χ is the polarization coefficient known as the dielectric susceptibility.

4.2 Dielectric relaxation

Maxwell's equation describes the complex permittivity ε^* as a time or frequency dependent property if time dependent processes take place within the sample. This time or frequency dependency can be attributed to several causes

Relaxation phenomena are typically related to the molecular fluctuation of dipoles due to their motion in a potential field. Moreover, the drift motion of mobile charge carriers (electrons, ions or charged defects) causes conductive contributions to the dielectric response [53]. In general, time dependent processes within the materials create fluctuations in the applied electrical field E(t) and the resulting dielectric displacement D(t).

The dependence of the complex dielectric function $\varepsilon^*(\omega)$ on the angular frequency ω of the outer electric field and temperature can generally be attributed to the following

1) Microscopic fluctuations of molecular dipoles [54].

2) Propagation of mobile charge carriers by translational diffusion of electrons, holes or ions.

3) The separation of charges at interfaces which gives rise to an additional polarization. The latter can take place at inner dielectric boundary layers (Maxwell/Wagner/Sillars-polarization) [55], [56] on a mesoscopic scale and/or at the external electrodes contacting the sample (electrode polarization) on a macroscopic scale. The contribution to the loss for this type of polarization can be orders of magnitude larger than the contributions from molecular fluctuation.

Each of the above mentioned processes have specific features in the frequency and temperature dependence of the real and imaginary part of the complex dielectric function. It is the objective of the present work is to analyze, to separate and to quantify their different contributions to the dielectric spectra for our materials of interest [53].

With gradual increasing frequency relaxation processes are characterized by some common features in the real and imaginary part of the complex dielectric function, which can be written as

$$\varepsilon^*(\omega)=\varepsilon'(\omega)-i\varepsilon''(\omega) \qquad (4\text{-}10)$$

For the real part $\varepsilon'(\omega)$ of the complex dielectric function there is a step like decrease with increasing frequency and the imaginary part $\varepsilon''(\omega)$ is characterized by a peak.

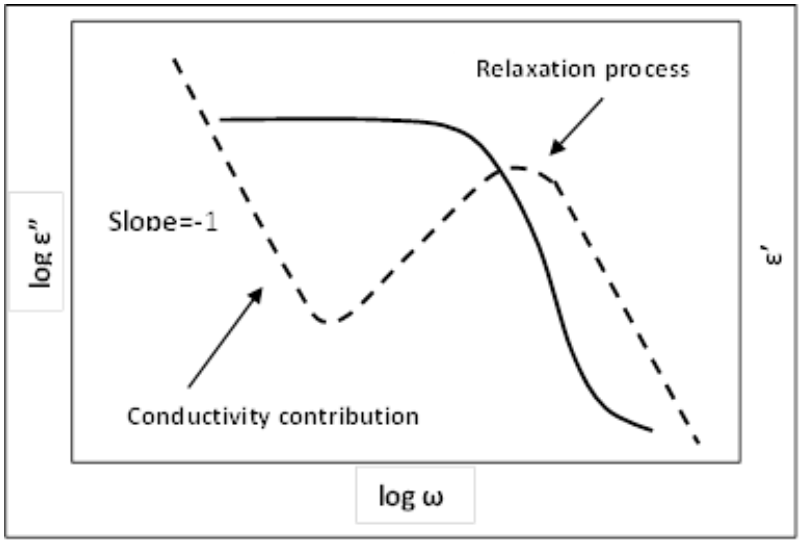

Figure 4.2. Real permittivity ε' (ω) (solid line) and imaginary permittivity ε" (ω) of the complex dielectric function for relaxation process of a ohmic conductor.

By contrast, conduction phenomena show an increase of the imaginary part of the dielectric function with decreasing frequency. In Figure 4.2, permittivity behavior of ohmic conductive material is shown for variable frequency. For pure ohmic conduction the real part of ε is independent of frequency.

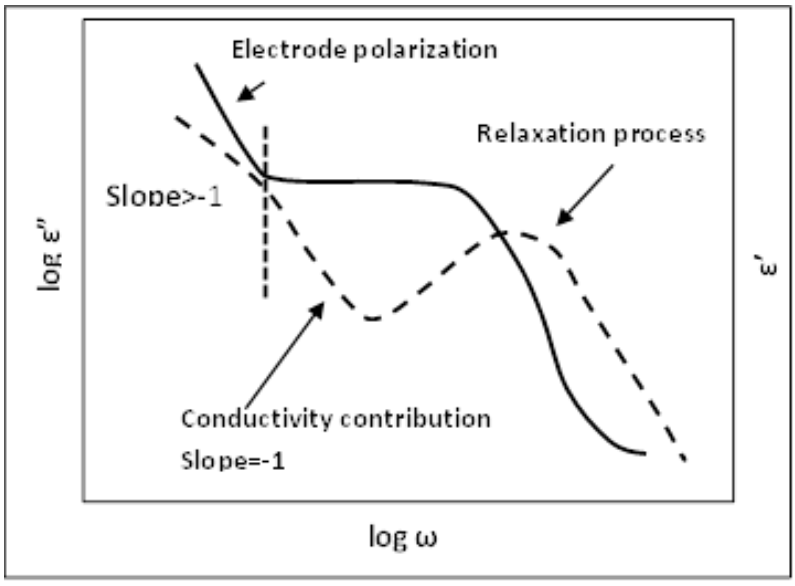

Figure 4.3. Real permittivity ε' (ω) (solid line) and imaginary permittivity ε" (ω) of the complex dielectric function for relaxation process of a ionic conductive material.

While for ionic material, conduction or polarization effects (at inner boundaries of external electrodes) the real part of epsilon increases with decreasing frequency shown in Figure 4.3.

Other useful alternative representations of dielectric properties of the material are the complex conductivity $\sigma^*$and complex electric modulus M*. They emphasize different aspects of polarization and charge transport for different frequency range. The dependence of real conductivity to frequency and temperature or charge carrier concentration has certain features that can be used to assume time temperature superposition and to scale the normalized conductivity with respect to normalized frequency to identify effect of different parameters on charge transport mechanisms [53], [54], [57].

4.3 Dielectric studies of Semiconducting disordered materials

From Maxwell's equation shown in equations (4-4) to (4-7), we see that the current density $\vec{j}$ and the time derivative of the electric displacement $\frac{\partial \vec{D}}{\partial t}$ are additive quantities. Thus the complex conductivity σ^* and the complex dielectric function (also called the complex permittivity, ε^*) are related by the following equation for a harmonic electric field.

$$\sigma^* = i\omega\varepsilon_0\varepsilon^* \tag{4-11}$$

Both of these quantities $\sigma^*$and ε^*contain significant information about the charge transport mechanisms in semiconducting disordered materials. To analyze the underlying charge transport mechanisms in these materials, measurement of the dielectric response over a wide frequency and temperature range can be made. And this response over a

frequency range represents a continuous process, wherein at higher frequency the charge carriers are driven by the external electric field over distances corresponding to atomic length scales while in the lower frequency region the charge carriers propagate on some percolation path from one side of the sample to the other. Thus, with decreasing frequency a length scale is involved going from microscopic to macroscopic dimensions. And it is a well-known experimental fact that dielectric property analysis from AC response shows extraordinarily similar behavior of dielectric functions for different materials including crystalline or amorphous ionic conductors and electronic conducting materials [58]–[61]. For disordered systems charge transport typically takes place due to hopping conduction of different types such as variable range hopping, phonon-assisted hopping, trigger induced hopping etc. [62]–[64]. And in a disordered system the motion of a charge, ionic or electronic, creates relaxation processes that are characterized by a relaxation time. This relaxation process can be studied by measuring the response of dielectric behavior by applying an external field excitation with a frequency comparable to the relaxation time. This complex dielectric behavior is found to be similar for a wide range of materials in frequency and temperature dependence such as electron conducting conjugated polymers [65], [66], ionic glasses [67], [68], ion conducting polymers [69], [70], and electron conducting carbon black composites [71], [72]. The different complex dielectric functions representations for these materials are equivalent but they emphasize different aspects of the underlying mechanisms. The dielectric interaction of these MIECs contains much information about their fundamental character and function. Broadband dielectric spectroscopy (BbDS) (with excitation in the 10^{-6} to 10^{12} Hz range) has been used as an effective field of that studies the dynamics of bound (dipole) and mobile

charge carriers as a function of applied conditions [53]. This knowledge of dielectric behavior of materials can be used to establish the effect of morphology and local interfaces between constituents on MIEC functionality in membranes. The goal of this work is to use dielectric response as a tool to analyze different dielectric mechanisms inside of an MIEC material as the basis for the prediction of oxygen transport in membrane separations. Understandings of these mechanisms are important to identify their contribution to the performance of the membranes, their dependence on different system and material parameters, and how to incorporate them to predict, design, control and fabricate a system of desired specification.

4.4 Broadband dielectric measurement

4.4.1 Novocontrol™ Systems

The dielectric impedance spectroscopy system consists of a Novotherm-HT high temperature control system with temperature ranges from ambient up to 1200˚C with 0.1˚C resolution. The system consists of a Novotherm-HT temperature controller, a furnace and a ceramic sample cell with movable holder from Probostat, an Alpha analyzer for impedance analysis. The specifications of the Novocontrol are as follows:

Frequency : 3μHz-20MHz

Phase accuracy : 0.002˚ or tanδ accuracy $3X10^{-5}$

Impedance range : $10^{-3}\Omega$-$10^{15}\Omega$

Novotherm- HT : Ambient to 1200˚C

Any sequence of time, temperature and DC-bias can be used. In figure 4.4 the schematic diagram of the Novocontrol setup is shown

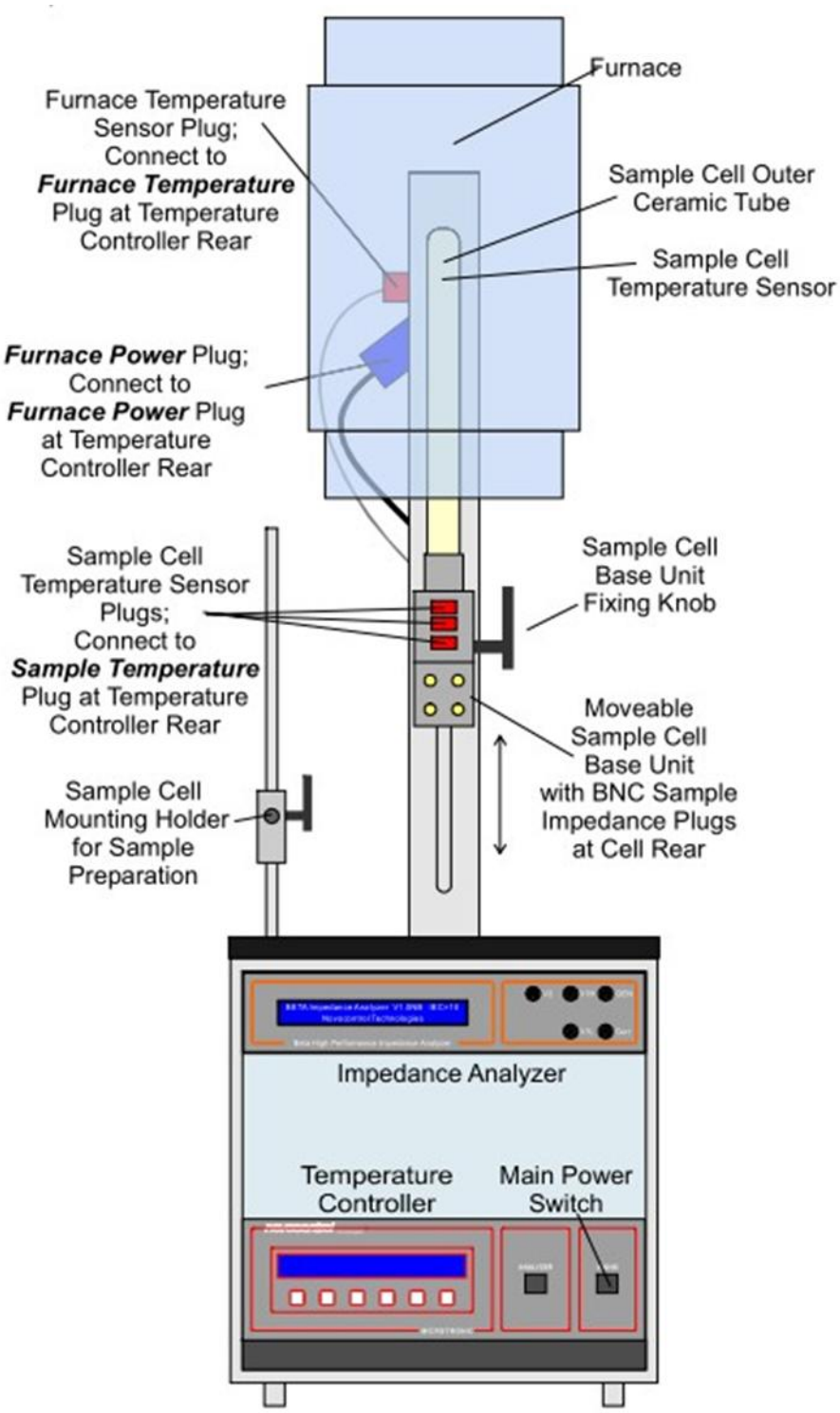

Figure 4.4. Novocontrol^{TM} system.

4.4.2 Alpha analyzer:

The alpha analyzer measures the complex dielectric, conductivity and impedance function of test materials as a function of frequency of the applied electric field with high precision. It is especially optimized for dielectric materials with high impedance and low loss factors over a broad frequency range, but can accurately measure highly conductive material with low impedance, as well.

4.4.3 Principles of Dielectric Measurement in the NOVOCONTRL:

The sample material is usually mounted in a sample cell between two electrodes forming a sample capacitor shown in figure 4.5.

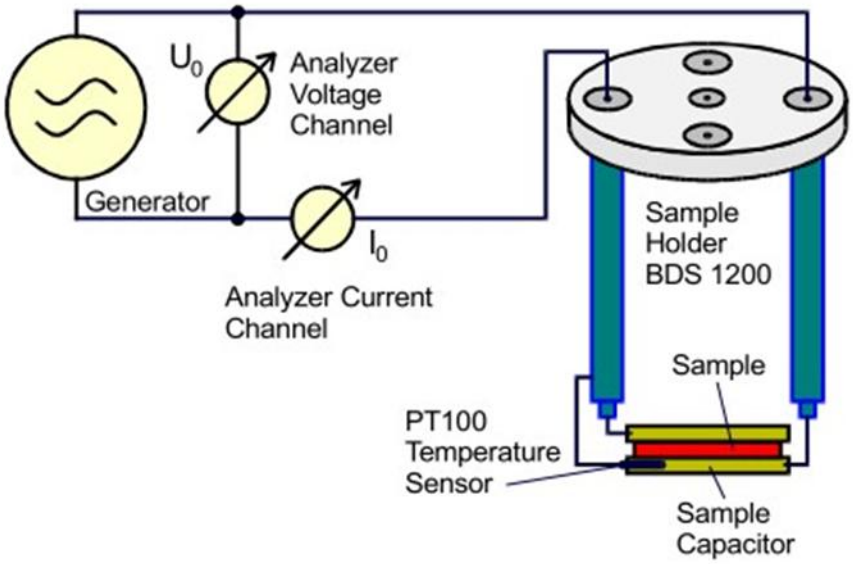

Figure 4.5. Principle of a dielectric or impedance measurement.

A voltage U_0 with a fixed frequency $\frac{\omega}{2\pi}$ is applied to the sample capacitor. U_0 causes a current I_0 at the same frequency in the sample. In addition, there will generally be a phase shift between current and voltage described by the phase angle φ shown in figure 4.6

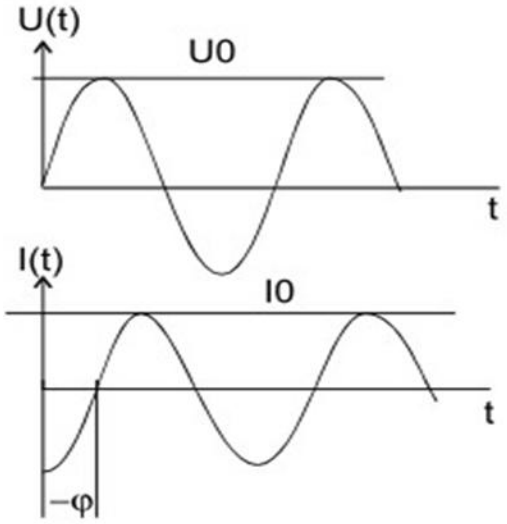

Figure 4.6. Amplitude and phase relations between voltage and current of a sample capacitor for electric measurements.

The ratio between U_0 and I_0 and the phase angle φ are determined by the sample material electric properties (permittivity and conductivity) and by the sample geometry. So the appropriate relations in complex notation can be expressed as

$$U(t)=U_0\cos(\omega t)=\mathrm{Re}\left(U^* \exp(i\omega t)\right) \tag{4-12}$$

$$I(t)=I_0\cos(\omega t+\varphi)=\mathrm{Re}\left(I^* \exp(i\omega t)\right) \tag{4-13}$$

With

$$U^*=U_0 \tag{4-14}$$

and

$$I^*=I'+iI'' \tag{4-15}$$

$$I_0=\sqrt{I'^2+I''^2} \tag{4-16}$$

$$\tan(\varphi)=\frac{I''}{I'} \tag{4-17}$$

For a sample with linear electromagnetic response, the measured impedance of the sample capacitor

$$Z^*=Z'+iZ''=\frac{U^*}{I^*} \tag{4-18}$$

And the imaginary permittivity can be calculated by

$$\varepsilon^*(\omega)=\varepsilon'-i\varepsilon''=\frac{-i}{\omega Z^*(\omega)}\cdot\frac{1}{C_0} \tag{4-19}$$

here C_0 is the capacity of the empty sample capacitor.

The specific conductivity is related to the dielectric function by

$$\sigma^*(\omega)=\sigma'-i\sigma''=i2\pi f\varepsilon_0(\varepsilon^*-1) \tag{4-20}$$

4.4.4 Probostat™ Assembly

The ProboStat™ is a test cell that enables in-situ measurements of electrical properties, transport parameters, and kinetics of materials, solid/gas interfaces and electrodes under controlled atmospheres at high temperatures up to 1600ºC. The sample under test rests on a 50 cm long support tube of alumina, inside a closed outer tube of alumina or silica. The sample can be contacted with 2 platinum wire mesh electrode shown in Figure 4.7. A spring-loaded alumina assembly holds the sample and electrodes in place under constant pressure. 16 electrical feed-throughs on the base allow use of 4 shielded electrode leads, surface guard, and 3 thermocouples. 2, 3 and 4 wire measurements are possible with the 4 electrode terminal available. Figure 4.8 shows gas supply tubes inside the sample station. Electrical connections are made via coax cables suitable for standard impedance spectrometer connectors, and standard thermocouple compensation cables. Gases can be fed in single or dual chamber modes directly onto or from electrodes, allowing measurements under controlled atmospheres, transport number

measurements with gradients, and testing of fuel cell, pump, and sensor components. Gas supply is via Swagelok quick-connects.

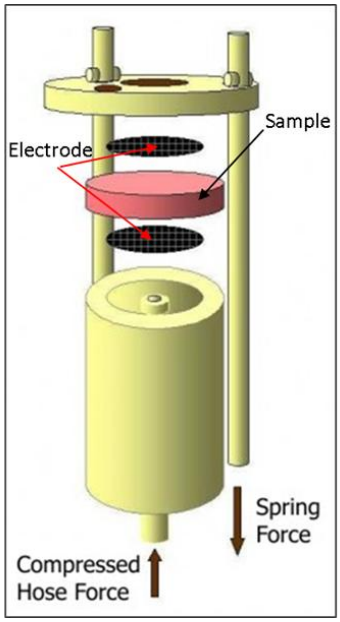

Figure 4.7. Sample inside the Probostat™ connected with two platinum wire mesh electrodes.

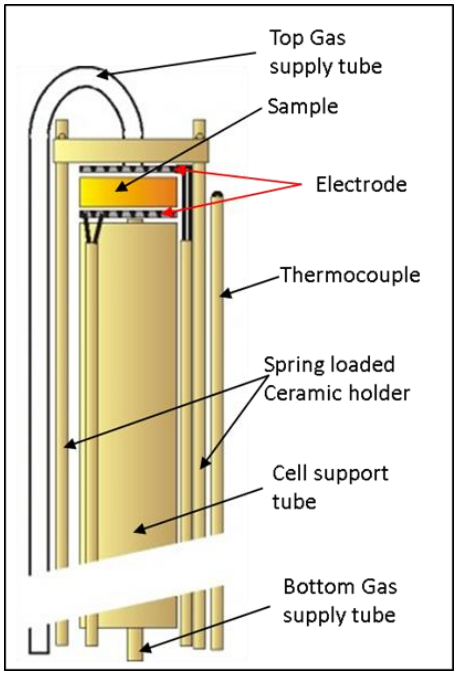

Figure 4.8. Spring loads and regular 2-electrode 4-wire setup with dual gas supplies and thermocouple in a Probostat™.

4.5 Dielectric impedance response study

In this study, we used the NOVOCONTROL^{TM} to measure the effects of electrode polarization, electrical properties of the single phase GDC and CFO, impedance response of the mixture materials in different gas surroundings, and in-situ impedance response of the 60GDC-40CFO membranes under various operating conditions. The single phase material conductivity was measured using the impedance study for a temperature range of 800°C-1060°C. Conductivity and dielectric response of the membranes were measured over a wide temperature range (400˚C-800˚C) and frequency (0.1Hz-1MHz) range in several gas environments. Gas was provided to the feed and permeate side independently at a flow rate of 50 ml/min with the following combinations: i) air/air, ii) N2/N2, iii) Air/N2 and iv) ambient air/nogas. For the in-situ measurement of the 60GDC-40CFO membrane, the sample was connected with the NOVOCONTROL during its operation and flux measurements with different operating temperatures and sweep gas flow rates.

4.5.1 Electrode polarization study

For our experiments we used platinum paste as an electrode to cover the entire surface. Pt paste, grade 5542 (ESL Inc.) was applied, dried at 110°C for 10 minutes and annealed to 950°C for 10 minutes with a ramp rate of 5°C/min. Then a platinum mesh electrode was placed over the paste covered face and electrode connection attached to the platinum mesh shown in figure 4.9.

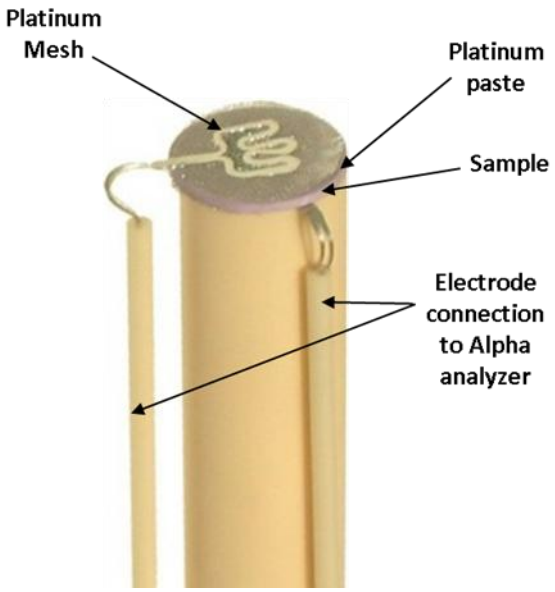

Figure 4.9. Complete in-situ measurement set-up block diagram.

To determine the effect of electrode polarization for the given platinum paste/platinum mesh electrode, we measured the conductivity value of a solid disc sample of YSZ and compared the values with reported conductivity values [73] for YSZ at high temperatures as shown in Figure 4.10(a). We also measured the conductivity value using only the platinum mesh as an electrode without using the platinum paste on the surface. A decreased value of conductivity for that case was observed indicating the improvement of the measurement by the use of platinum paste on the surface. Figures 10 show a) reported conductivity values and b) our measured value.

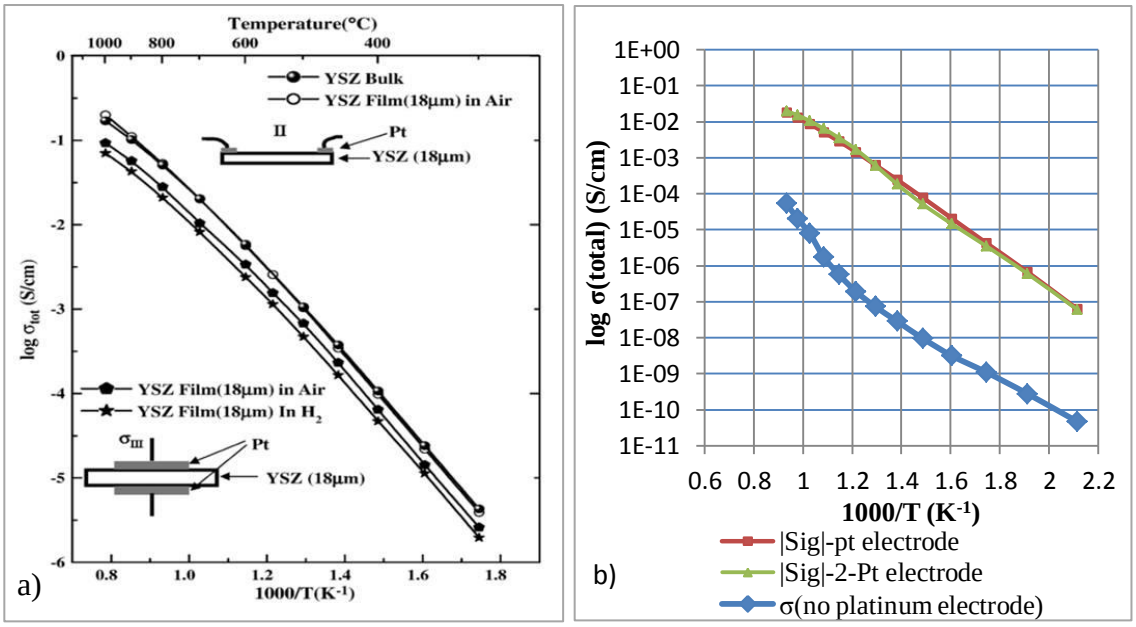

Figure 4.10. Complete in-situ measurement set-up block diagram.

4.5.2 Single phase material properties

Single phase material properties i.e. total conductivity, σ_t and permittivity, ε of GDC and CFO in ambient air were measured. Powder of the single phase materials GDC and CFO was die-pressed and sintered at 1300°C and 1100°C respectively to make the disk shaped samples with dimensions shown in Table 4.1.

Table 4.1. Dimensions of single phase GDC and CFO disk samples.

Sample	Diameter(mm)	Thickness(mm)	Area(mm^2)
GDC	15.4	1.3	186.27
CFO	14.9	2.16	174.37

Total conductivity of each samples were measured for 800°C to 1060°C and for a frequency range of 0.1HZ-1MHz. We calculated the conductivity of GDC at each temperature from the Cole-Cole plot shown in Figure 4.11 where the first intercept of the

x-axis of the plot is the total resistance of the material. We calculated the total conductivity of the samples using the resistivity relation.

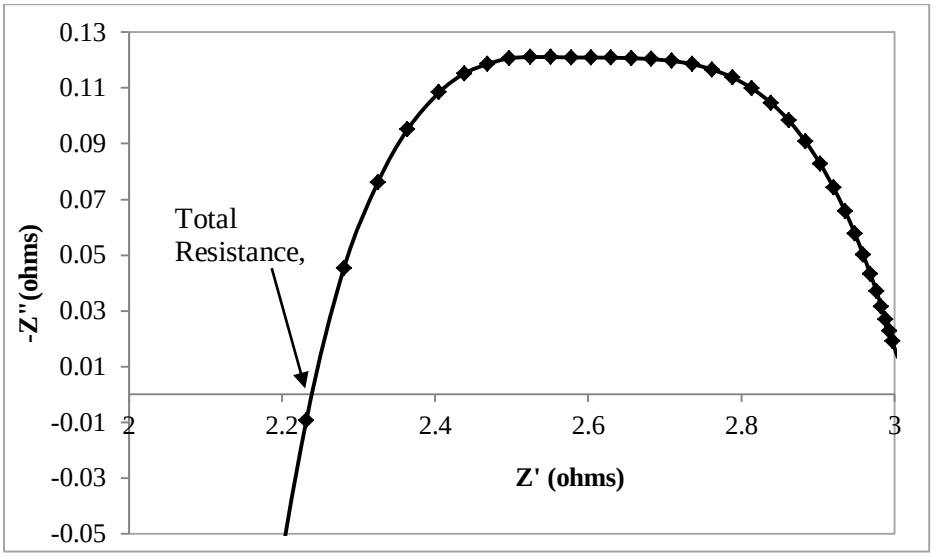

Figure 4.11. Cole-cole plot for GDC membrane at 1060°C in air.

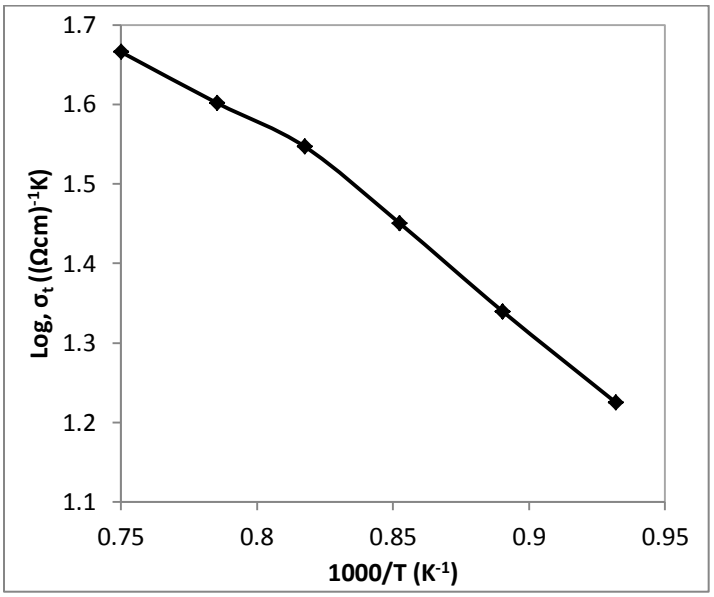

Figure 4.12. Total conductivity of GDC in air.

Figure 4.12 shows our measured value of GDC single phase represented in a Arrhenius plot. Our results were compared with values reported by Wang et. al., Ivers-Tiffee et. al. and Kudo et.al., shown in Figure 4.13 [74]–[76]. Our measure values were

lower than the reported value. This difference might have originated from difference in sintering condition and starting material as well.

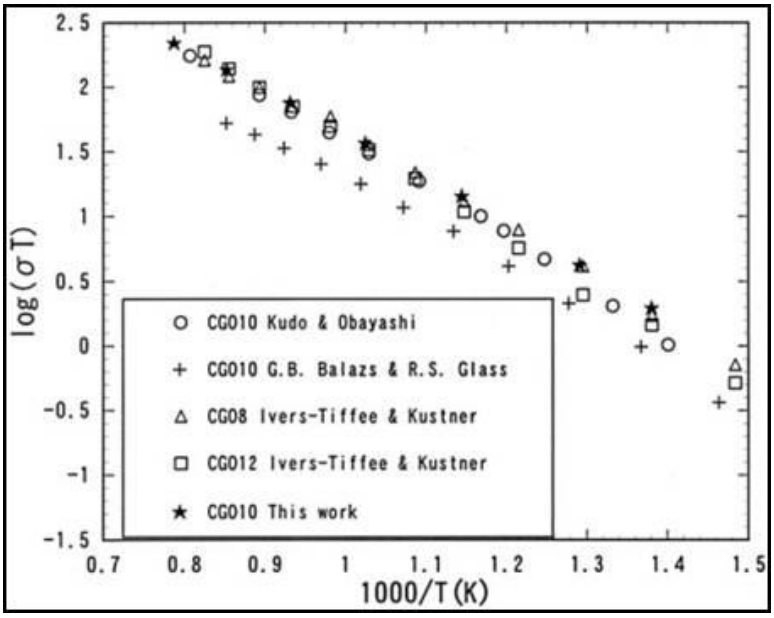

Figure 4.13. Total conductivity of different forms of GDC compared by Wang et. al. [74].

Similarly we measures conductivity values of CFO single phase material are shown in Figure 4.14.

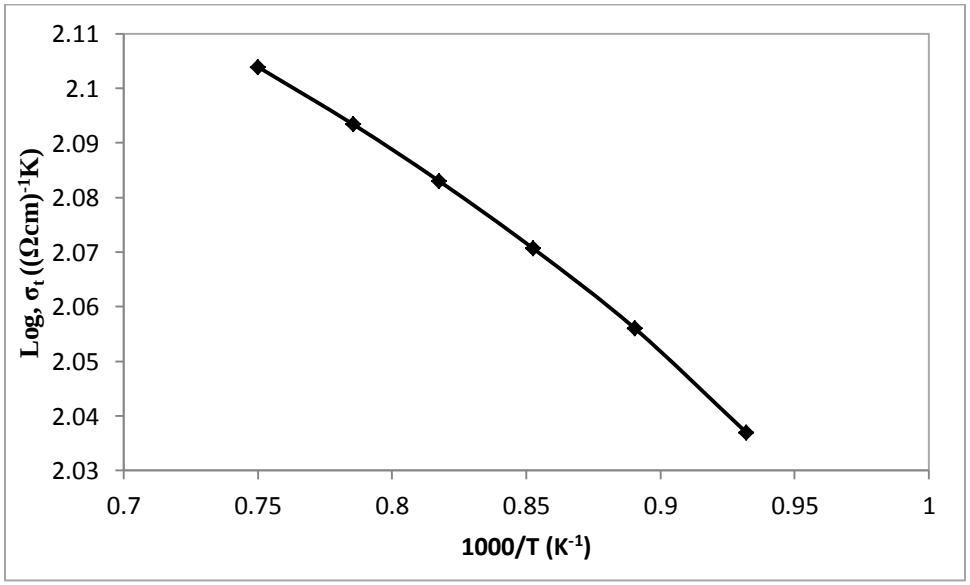

Figure 4.14. Total conductivity of CFO in air.

Conductivity values measured for GDC and CFO are presented in Table 4.2. These values were used in the calculation of flux using the Wagner's equation in Section 3.4.3.

Table 4.2. Total conductivity of single phase GDC and CFO.

Temperature(°C)	Total conductivity of GDC, σ(S/cm)	Total conductivity of CFO, σ(S/cm)
800	0.001014797	0.101479738
850	0.00101309	0.101309012
900	0.001003217	0.100321661
950	0.000989778	0.098977772
1000	0.000974009	0.097400852
1060	0.000952893	0.095289306

Our total conductivity of CFO was much lower compared to the reported result by Takamura et. al. [47]. For high conductive material like CFO to measure conductivity accurately, 4 probe DC measurement methods might be used.

4.5.3 Impedance of the membranes in different conditions

For impedance response of different samples the following conditions were used: i) no gas (ambient air), ii) air-air (air supplied to both membrane sides), iii) N_2-N_2 (N_2 supplied to both membrane side) and iv) N_2-Air (N_2 supplied to permeate, Air supplied to feed). Temperature was varied from 400˚C-800˚C in increment of 50˚C and each of the gas flow rate were maintained at 50mL/min. Impedance values were measured for a frequency range of 0.1Hz-1MHz. Total conductivity of the membranes at different frequency for 800°C is shown in Figure 4.15. Here we can see that the total conductivity of the 50GDC-50CFO is the highest and total conductivity decreases with decreasing CFO phase volume percentage. But our flux measurements indicate that flux value of the

membrane does not follow the conductivity trend shown in Figure 4.15 and an intermediate mixture of 60GDC-40CFO has a higher flux discussed in Section **3.4.1.**

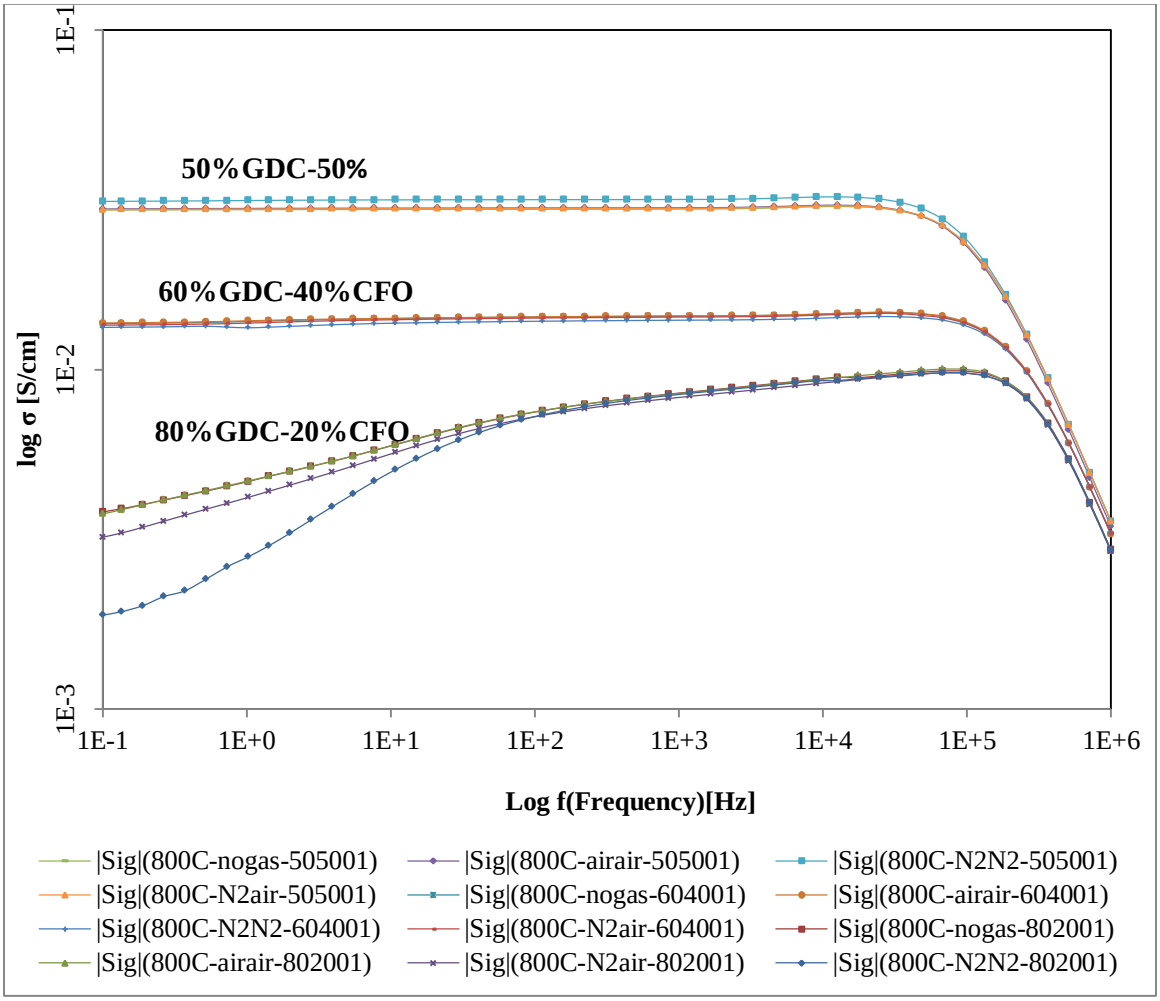

Figure 4.15. Combined conductivity vs. Frequency at various gas flow rates @ 800˚C.

4.5.4 In-situ impedance response of the 60GDC-40CFO membrane

To conduct in-situ impedance measurements of the 60GDC-40CFO MIEC membrane, the sample was set-up inside the Probostat^{TM} by similar methods used for the flux measurements. In the in-situ experiments, platinum paste was applied on each side of the sample. Platinum wire mesh was placed on top of the platinum paste layer and the sample

was placed in the support tube with gold seal rings. The membrane was subjected to different operating temperatures and sweep gas flows for the permeation and simultaneous measurements of flux and impedance response were made using a gas chromatographer and NOVOCONTROL^{TM}. Figure 4.16 shows a Cole-Cole plot for the 60GDC-40CFO sample at 850°C for different flow rates where we see that at lower flow rates the impedance is higher but the impedance becomes constant with higher flow rates. This is due to the fact that at slower flow rates, the surface effect becomes the controlling factor on the flow rate and does not reflect the effect of material bulk properties and interfaces. So to specifically study material parameter effects on flux, a higher flow rate should be used.

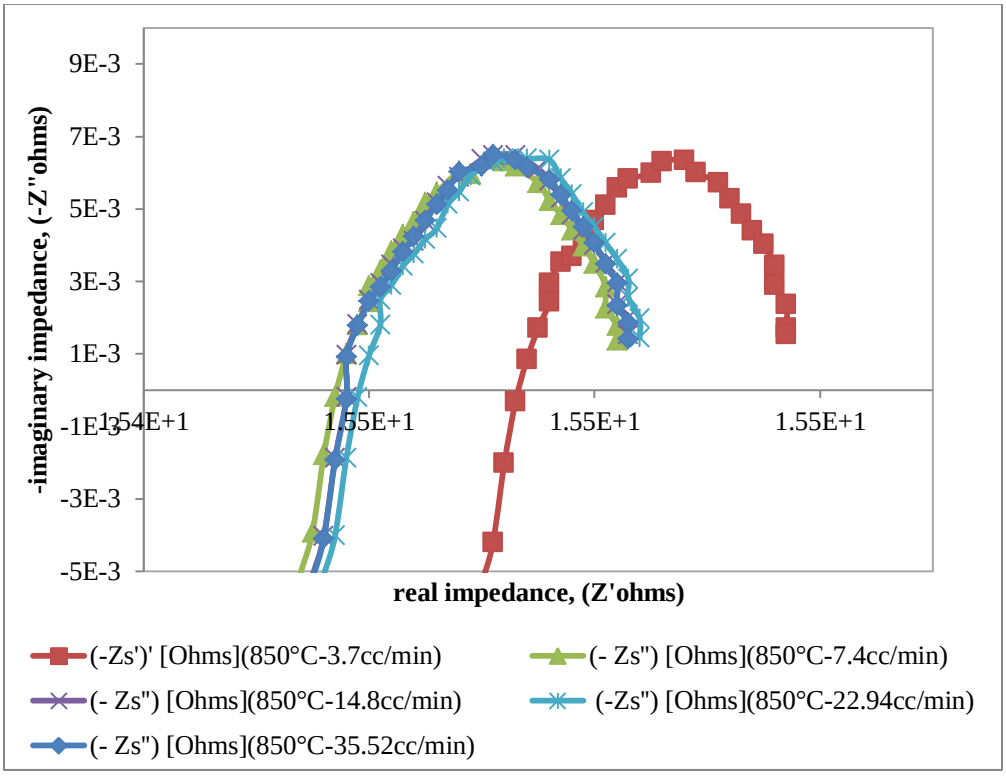

Figure 4.16. Cole-Cole plot for the 60GDC-40CFO samples at 850°C for different flow rates.

4.5.5 Permittivity study

Conduction phenomena show an increase in the imaginary part of the complex permittivity function, ε*(ω) in a material, as discussed earlier. For pure ohmic conductivity the real part of ε*(ω) is independent of frequency. But for non-ohmic or ionic conduction of polarization effects originating from inner boundaries or electrodes, the real part of ε*(ω) increases with decreasing frequency. Figure 4.17 shows a typical real permittivity response for a material exhibiting electrode polarization [53].

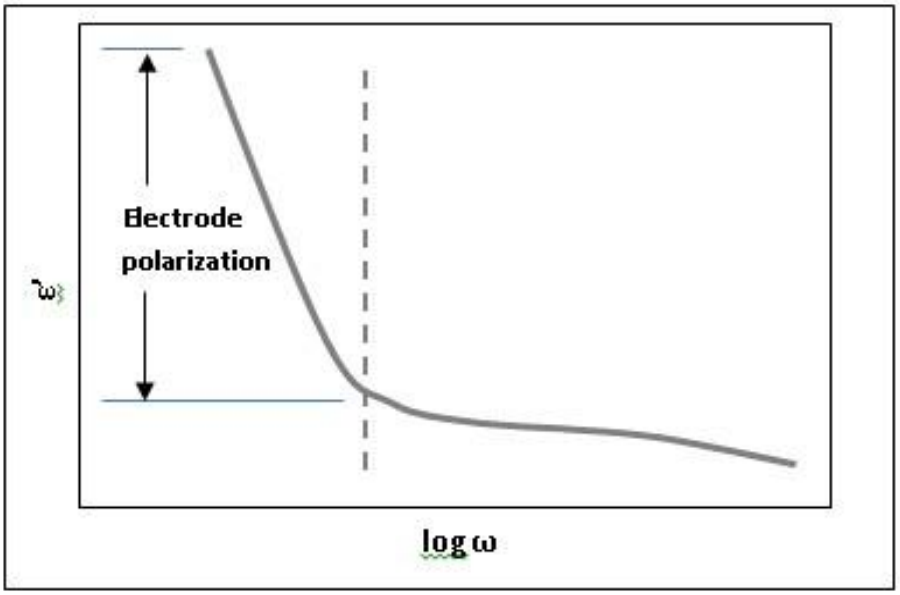

Figure 4.17. Electrode polarization responses in a permittivity plot at lower frequency.

In our initial study of the membrane impedance with no sweep gas flow, for a lower temperature of 400°C, the real permittivity part of ε*(ω) increased steeply with decreasing frequency indicating electrode polarization at lower temperature.

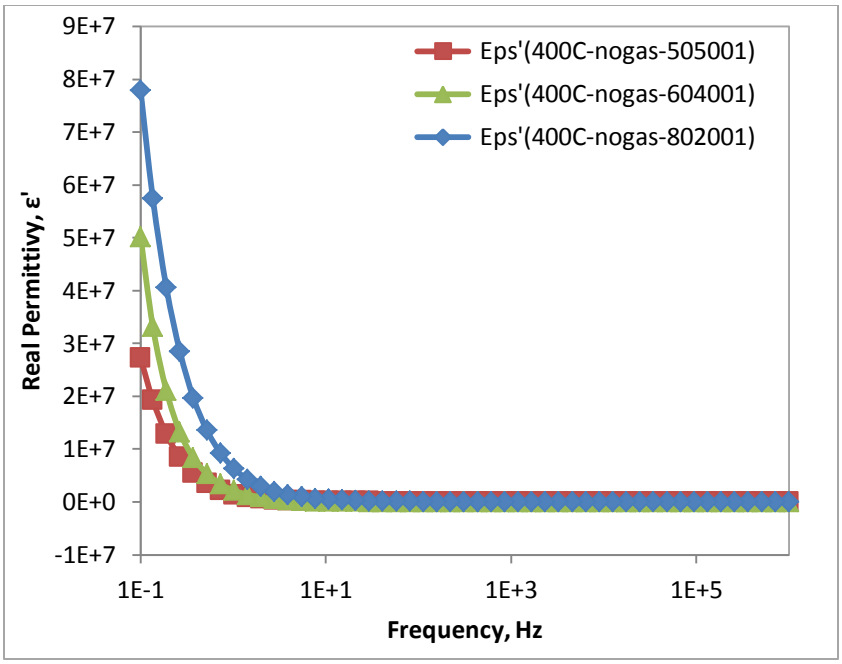

Figure 4.18. Permittivity plot for different mixtures @ 400C.

Figure 4.18 shows the steep rise of the real permittivity at lower temperature. At a higher temperature of 800°C, the 80GDC-20CFO sample shows much higher electrode polarization behavior as shown in Figure 4.19.

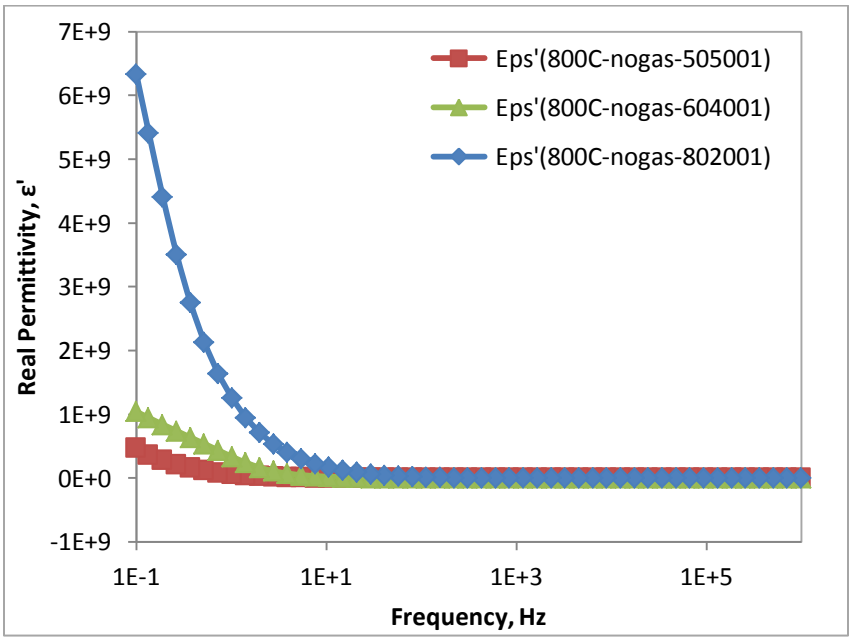

Figure 4.19. Permittivity plot for different mixtures @ 800C.

From our in-situ impedance response study of the 60GDC-40CFO sample, Figure 4.20 shows the real permittivity, ε'(ω) increasing with a steep slope indicating high electrode polarization for a lower temperature of 850°C. The electrode polarization is independent of the sweep gas flow rate.

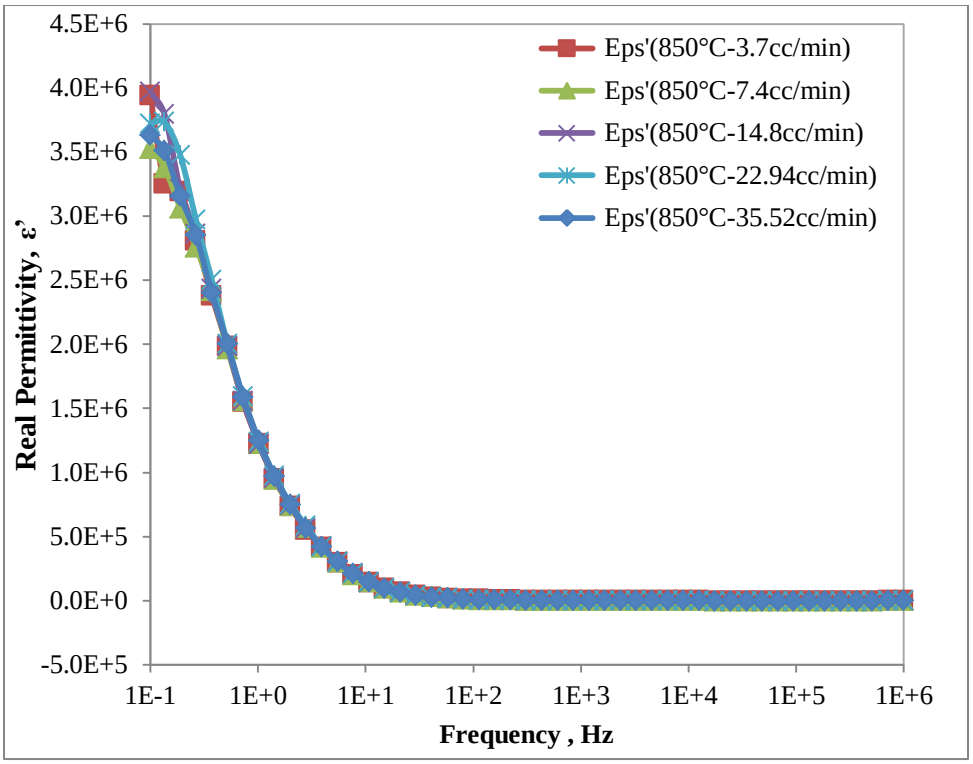

Figure 4.20. Real permittivity of 60GDC40CFO from in-situ measurements at 850°C for variable oxygen partial pressure.

The effect of electrode polarization decreases with increasing temperature shown in Figure 4.21 and the real permittivity plot represents ionic conduction.

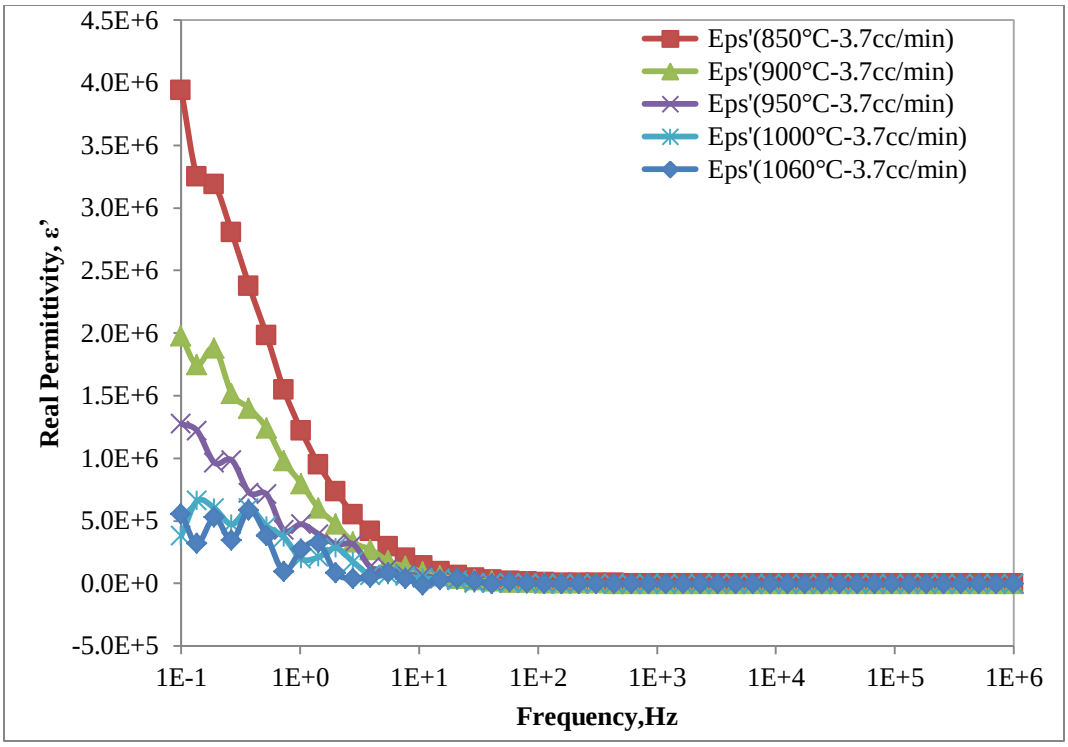

Figure 4.21. Real permittivity of 60GDC40CFO from in-situ measurements for variable temperature and constant oxygen partial pressure.

CHAPTER 5

NUMERICAL INVESTIGATION

5.1 Finite element analysis model

For the finite element analysis to generate a model capable of calculating impedance response for a given microstructure domain with different materials for a broadband frequency spectrum, COMSOL^{TM} Multiphysics software has been used. For this particular analysis the time harmonic in-plane quasi static, electric sub-module of the AC/DC module has been used. Similar models have been used to analyze dielectric response of water uptake in organic coatings [77]. This application is useful when inductive effects are negligible.

The time-harmonic, quasi-static, Maxwell's equations in vector form for the electric potentials are:

$$-\nabla.d\left((\sigma+j\omega\varepsilon_0)\nabla V-(J^c+j\omega P)\right)=dQ_j \tag{5-1}$$

The constitutive equations for linear, isotropic materials have been applied for the electric displacement vector, D:

$$\vec{D}=\varepsilon_0\varepsilon_r\vec{E} \tag{5-2}$$

As there is no current source present and no external current density, equation (5-1) becomes

$$-\nabla.d\left((\sigma+j\omega\varepsilon_0)\nabla V\right)=0 \tag{5-3}$$

Equation (5-3) is the partial differential equation used here to describe the Impedance response.

This model is capable of calculating dielectric response over a wide frequency range for a given domain. And this dielectric response showed sensitivity to local geometric variation of regular shapes [78]. Figures 5.1 and 5.2 shows dependence of impedance on microstructural variation where impedance varies for both geometrical shape and position difference. This difference is visible from a lower frequency to high frequency. For shape variation as holes of circular, square and triangular shape with equal area, impedance response is clearly visible. And even the positions of the holes are affecting the response as square holes were moved in the structure to get a different response.

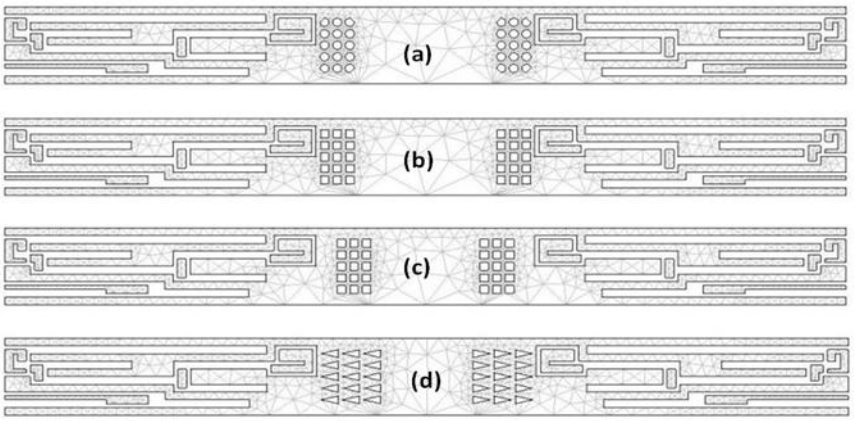

Figure 5.1. Geometric variation of shape and placement in a single phase material a) circular holes, b) square holes, c) square holes moved and d) triangular holes.

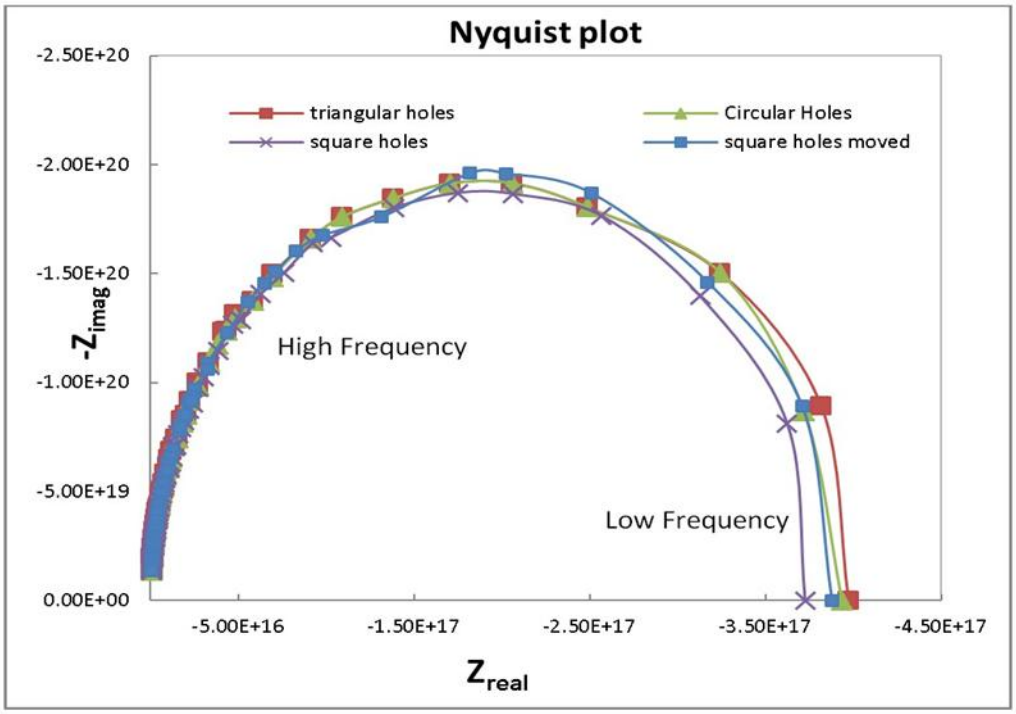

Figure 5.2. Impedance responses to variable geometric morphology over frequency range of 1Hz-1MHz.

5.2 Model validation

For our experiment we used a composite sample of high and low conductive material tin and epoxy shown in Figure 5.3. Dielectric permittivity of epoxy was higher than tin. The tin inclusion in the sample was prepared by using a die. Then the surface of the tin inclusion was machined to obtain smooth surface. The Lenticular shape can be described as the intersecting region between two cylinders. Then the tin inclusion was submerged in a pool of liquid epoxy inside a cubic die. After the epoxy solidified the combination structure was machined to obtain the shape shown in Figure 5.3.

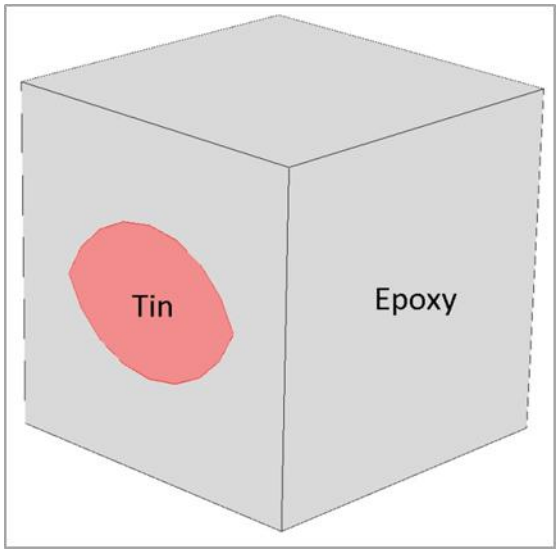

Figure 5.3. Epoxy-tin composite sample.

Baker et. al. provided the samples they used for their study of heterogeneous dielectric material [79] shown in Figure 5.4.

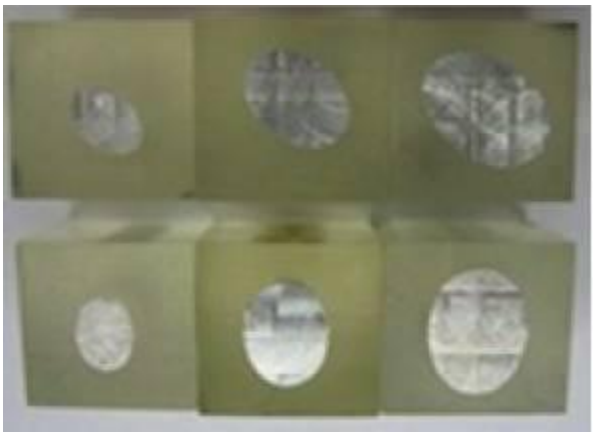

Figure 5.4. Epoxy-tin composite sample of different inclusion orientation and volume fraction.[79]

To get frequency dependent dielectric properties of individual materials we prepared a solid cubic sample of epoxy and tin and measured their conductivity and permittivity. NOVOCONTROL^{TM} was used to measure the properties. It has a frequency range from 3μHz-20MHz. But For our experiment we choose a range from 3Hz-1MHz.

Figure 5.5 and 5.6 show conductivity and permittivity is changing with increasing frequency. For tin its conductivity and permittivity was constant throughout the frequency range at $9.17x10^6$ S/m and 1.

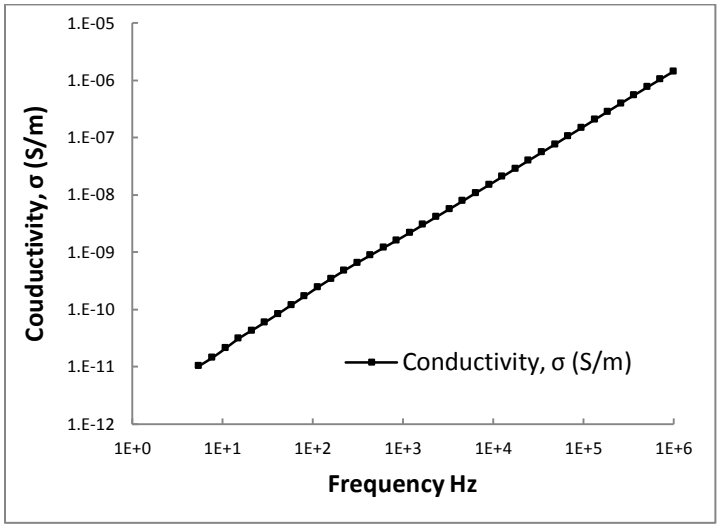

Figure 5.5. Single phase epoxy Conductivity increasing with increasing frequency, obtained using NOVOCONTROL.

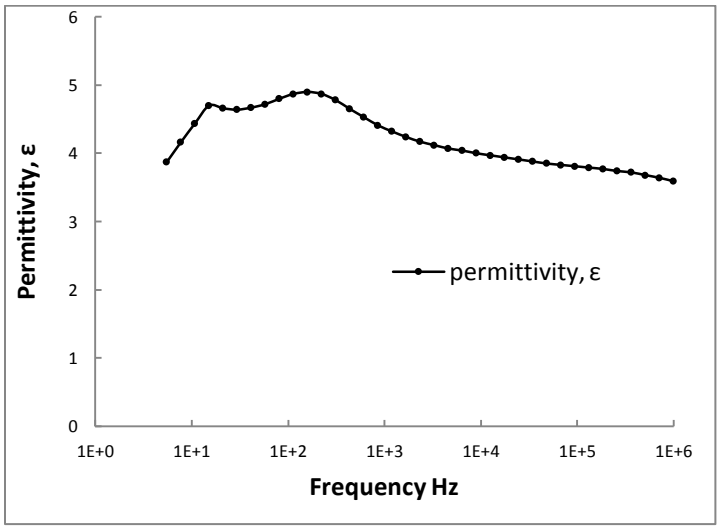

Figure 5.6. Single phase epoxy permittivity changing with frequency, obtained using NOVOCONTROL.

To apply potential to the sample for NOVOCONTROL measurement, a spring loaded fixture was used to maintain constant pressure. Copper plates were used as electrode for the samples.

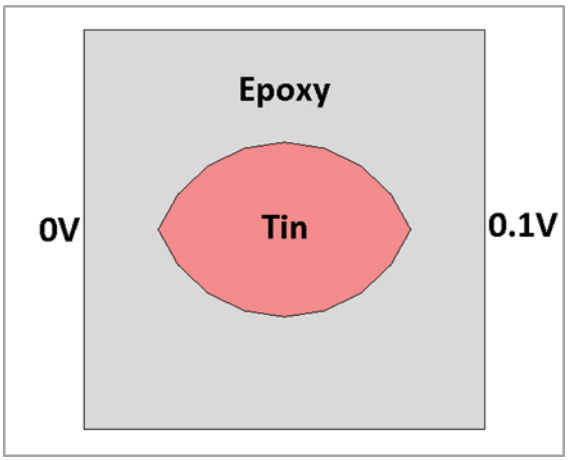

Figure 5.7. Boundary condition for model calculation.

Three different types of sample were made by changing the orientation of the lenticular tin inclusion. The orientations of the tin inclusion were 0˚, 45˚ and 90˚ with respect to the applied field direction. The measured frequency range was from 3Hz-1x10^6 Hz. Applied voltage was 0.1 Volt. The two input boundary conditions of 0V and 0.1 volt used in the model are shown in Figure 5.7. All the other boundaries of the domain were insulated. Frequency dependent single phase material properties obtained were provided to the COMSOL model and we used the values of varying conductivity and permittivity for epoxy to the calculation in COMSOL for corresponding frequency and kept the tin properties constant for all the calculation.

Figure 5.8 shows comparison of experimental and computational value of impedance for three different orientations. At higher frequency the data look to be in good agreement. But at the lower frequency the values have a very small difference with experimental values have slightly higher value than the calculated values. This may be due to the fact that for the experiments the impedance might include the impedance originating from the contact between the sample and electrode. Although the surface as

well as the electrode was polished to attain a good surface connectivity there still might be where the electrode was not touching properly. But for the computation we directly applied direct potential to the surface without any electrode. Hence lower impedance was measured for calculation. To avoid this in future a metallic conductive paste might be added on the input surface of the sample. And electrode domain can also be added to the model. So from the compared data it can be said that if a static material property value for the epoxy were to be selected to calculate computationally the impedance response of the sample, value for the higher frequency would not have match the experimentally measured data.

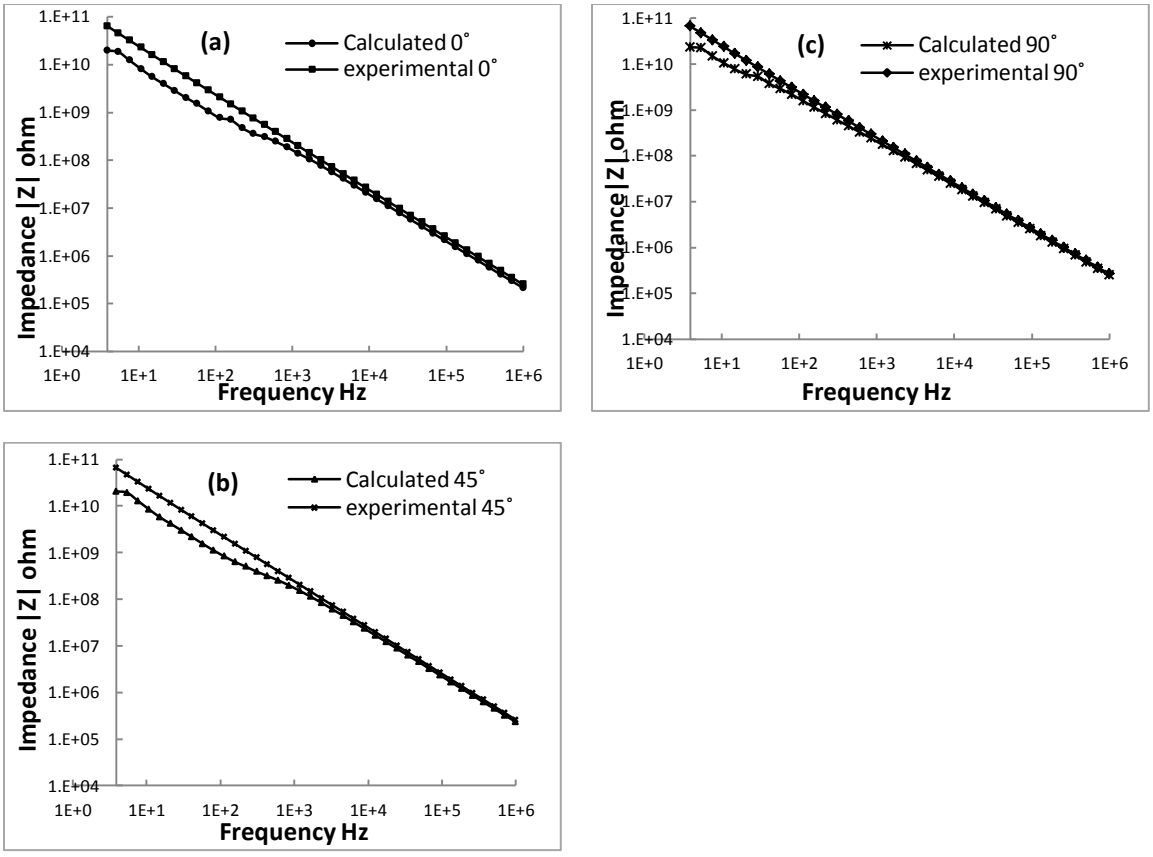

Figure 5.8. Measured impedance response vs computed impedance response of the epoxy-tin composite material (a) 0˚ orientation of the lenticular tin inclusion with the applied field, (b) 45˚ orientation of the lenticular tin inclusion with the applied field and (c) 90˚ orientation of the lenticular tin inclusion with the applied field.

So from the compared data it can be said that if a static material property value for the epoxy were to be selected to calculate computationally the impedance response of the sample, value for the higher frequency would not have match the experimentally measured data.

5.3 3D analysis of the real membrane structure

To validate our model we used regular geometric structure which can be drawn using the typical computer aided design (CAD) approach to describe a volume using splines, triangles etc. However, for a wide range of objects (biological structures, ceramic micro or nano structures for example) no CAD description is available. The simplest approach to obtain a topological model of these structures is to use an automated method for three dimensional volume or surface acquisition such as a surface scanner or one of a number of 3D imaging modalities (XCT, MRI, Ultrasound). A surface scanner can produce a point cloud description of the surface of the object. These scanners can generate a digital description of the volume by providing values measured at points placed on a structured grid. By considering that these points are in the center of contiguous but non overlapping bricks we can partition the scanned space. These bricks are called voxels (volumetric pixels).

5.4.1 X-ray micro and nano tomography

Initially our in house Xradia microXCT was used to generate 3D image of a single phase structure with irregular shaped inner structures. This is a non-destructive method.

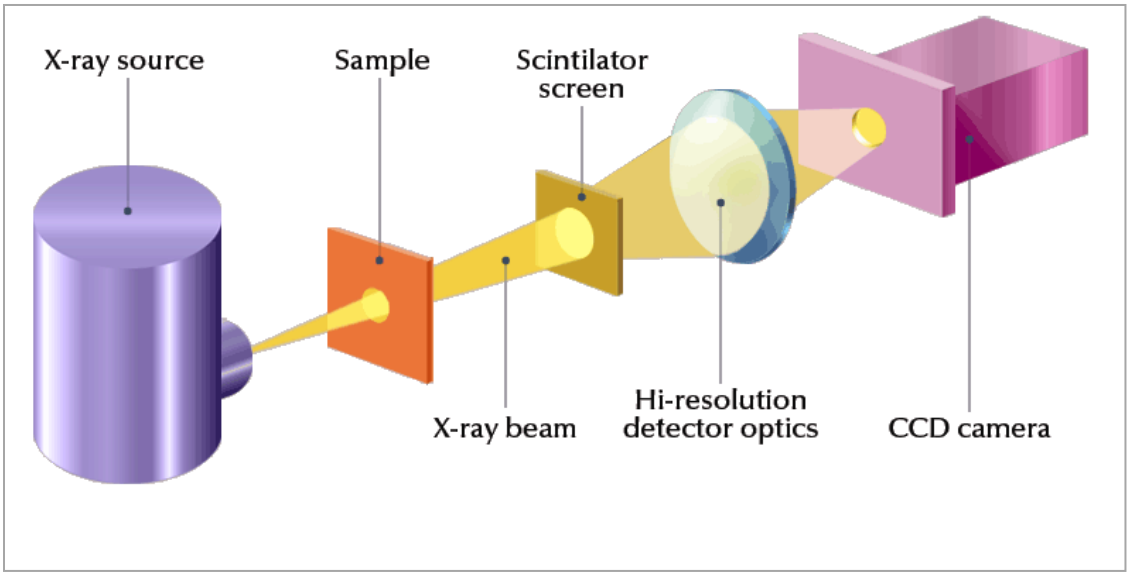

Figure 5.9. X-ray microscopy schematic diagram.

Figure 5.9 shows a schematic of the X-ray micro tomography system. The source for imaging is an X-ray generator, capable of producing X-ray radiation from 90kV-150kV. This range enables to resolve even low contrast materials like composites, polymers, foams and soft materials. The X-ray enters a reflector condenser optic and is refocused on the sample. The sample, mounted on a high precision manipulator, is rotated through a range of angles. X-ray penetrates through the sample, and 2D projection images are magnified onto a high-resolution CCD detector using a Fresnel zone plate, acting as an objective lens. A reconstruction algorithm is used to create 3D volume data from the acquired projections based on X-ray density and image shadowing.

But Micro XCT gave us image of the micro scale that did not capture smaller detail present in the MIEC membranes. To capture structural variation in the nanometer range similar process using nanotomography can be used shown by Chiu et al [80], [81] where X-ray nano tomography was done using transmission x-ray microscope (TXM) at the National Synchrotron Light Source, beamline X8C [82]. Harris et. al. performed

element-sensitive XNT measurements at X-ray beam energies above and below elemental contrast in the 3D X-ray image to identify different phases3D [83]. 3Drepresentation obtained from the x-ray nano-tomography is shown in Figure 5.10.

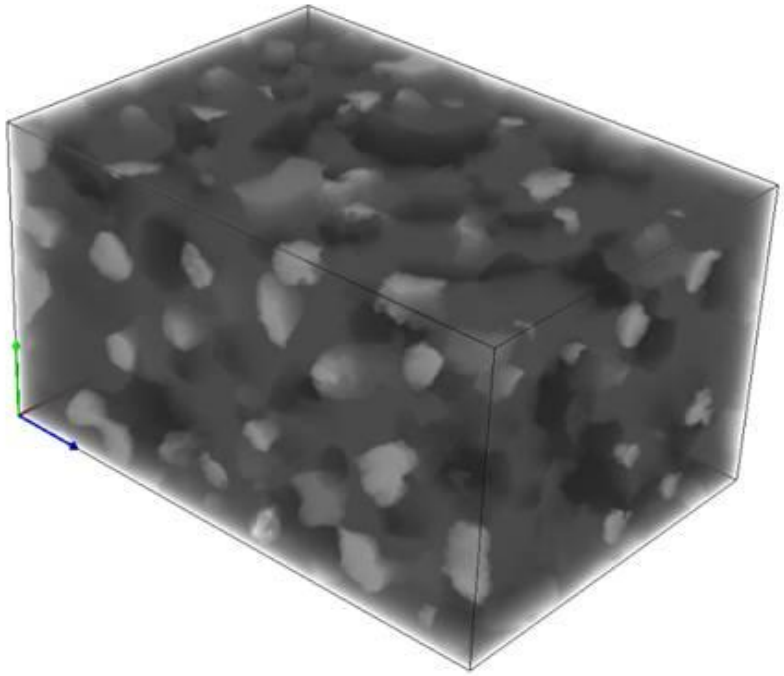

Figure 5.10. 3D x-ray scan of MIEC membrane.

Dr. Wilson Chiu and his group conducted the above investigation and provided us with the stack of images shown in Figure 5.11 and with the phases differentiated based on their X-ray absorption behavior and represented by different grayscale intensity shown in Figure 5.12.

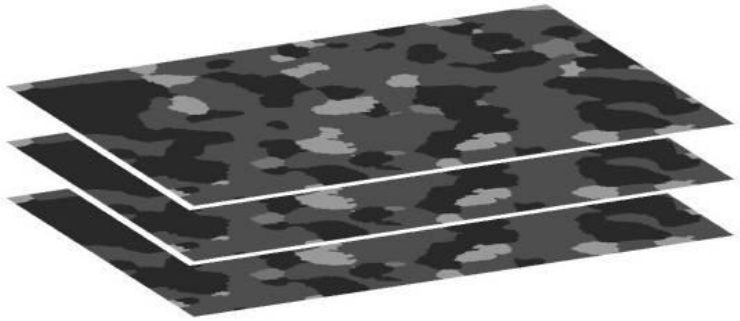

Figure 5.11. 2D image stack of image obtained from 3D x-ray scan.

The 2D image stacks with differentiated phases shown in Figure 5.11 were imported and analyzed in the Simpleware™ image processing software. It was also used to generate 3D domains to be used in the COMSOL™ multiphysics models.

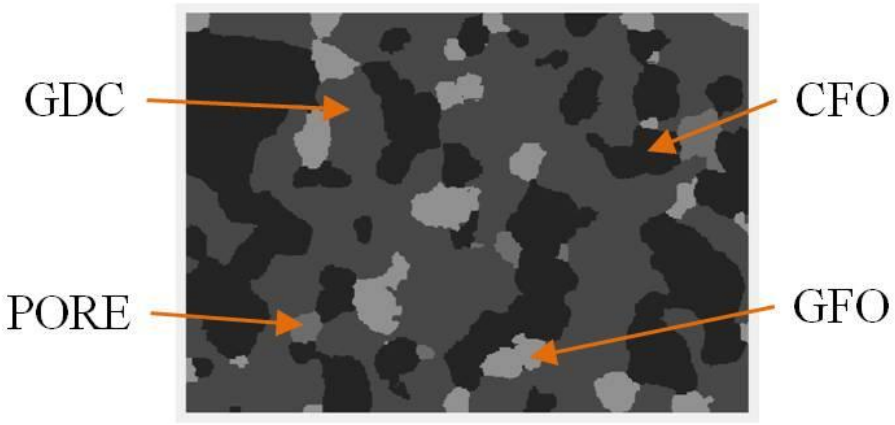

Figure 5.12. Grayscale segmentation of X-ray tomography scan based on X-ray absorption behavior.

5.4.2 Domain generation for computational study

The grayscale intensity data are treated as background data based on which Simpleware™ segments each phases. The segmentation will be done by assigning binary volume data called masks. These describe how an object fills the space. Ideally, each object of interest should be represented by a mask shown in Figure 5.13.

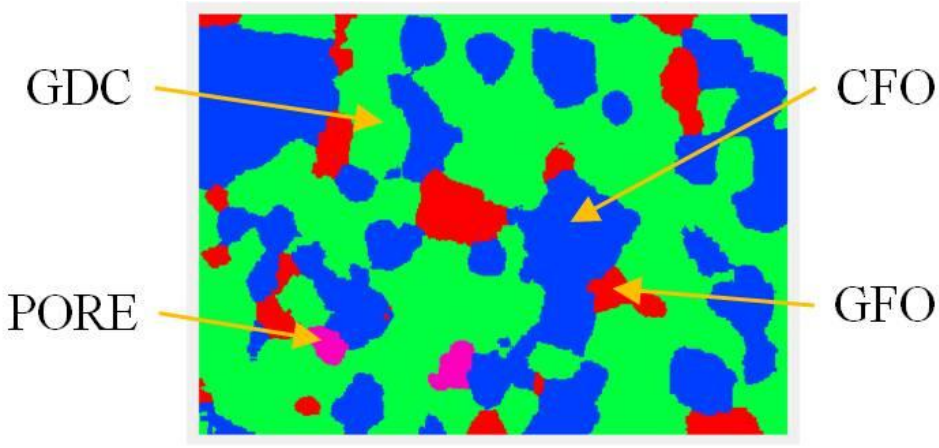

Figure 5.13.Mask segmentation of different membrane phases based on their grayscale intensity.

These masks can be analyzed on, modified and filtered within the software to remove image artifacts and noises using different filters available in the software. After the segmentation of the different phases into volume, it can be converted into volumetric mesh to be exported to COMSOL for calculation. It is possible to refine the mesh based on the size of the features of the structure. Figure 5.14 shows the different layer of the 3D masks.

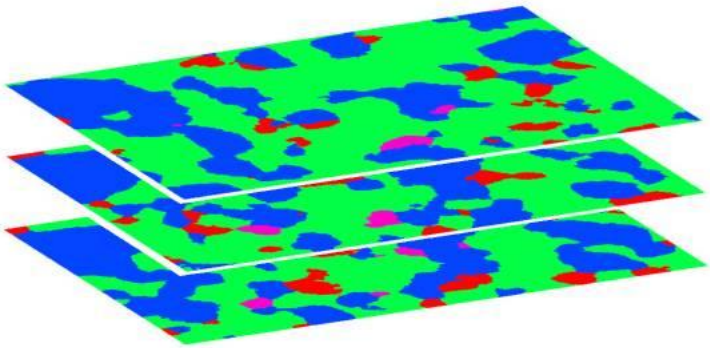

Figure 5.14. Stack of segmented mask representing different layer of the membrane structure.

Figure 5.15 shows the combined 3D volume representation of the 60%GDC-40%CFO which is divided into 4 different phases differentiated by different colors.

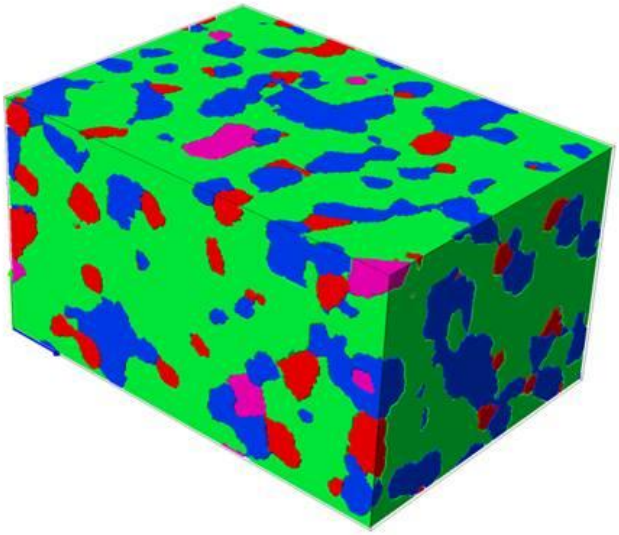

Figure 5.15. Three dimensional volume representation of full 60%GDC-40%CFO membrane.

Surface area of the different phases, their volume fraction can be calculated from there representing volumes. Volume fraction and surface area of the 60%GDC-40%CFO is shown in Table 5.1.

Table 5.1. Total volume, volume fraction and surface area of the phases present in the 60%GDC-40%CFO membrane.

Phase	Color	Volume (mm^3)	Volume fraction of background (%)	Surface area (mm^2)
CFO		1.14E+07	34	2.09E+06
GDC		1.91E+07	57	2.63E+06
PORE		5.73E+05	1.71	1.68E+05
GFO		2.44E+06	7.29	8.46E+05

Here we can see that although we started with a 60%GDC-40%CFO sample, after sintering, there is a third phase present and also there is a small percentage of pores present in the sample. Thus, the sample contains less percentage of GDC and CFO than we intended. Figure 5.16 shows all of the four phases presented separately.

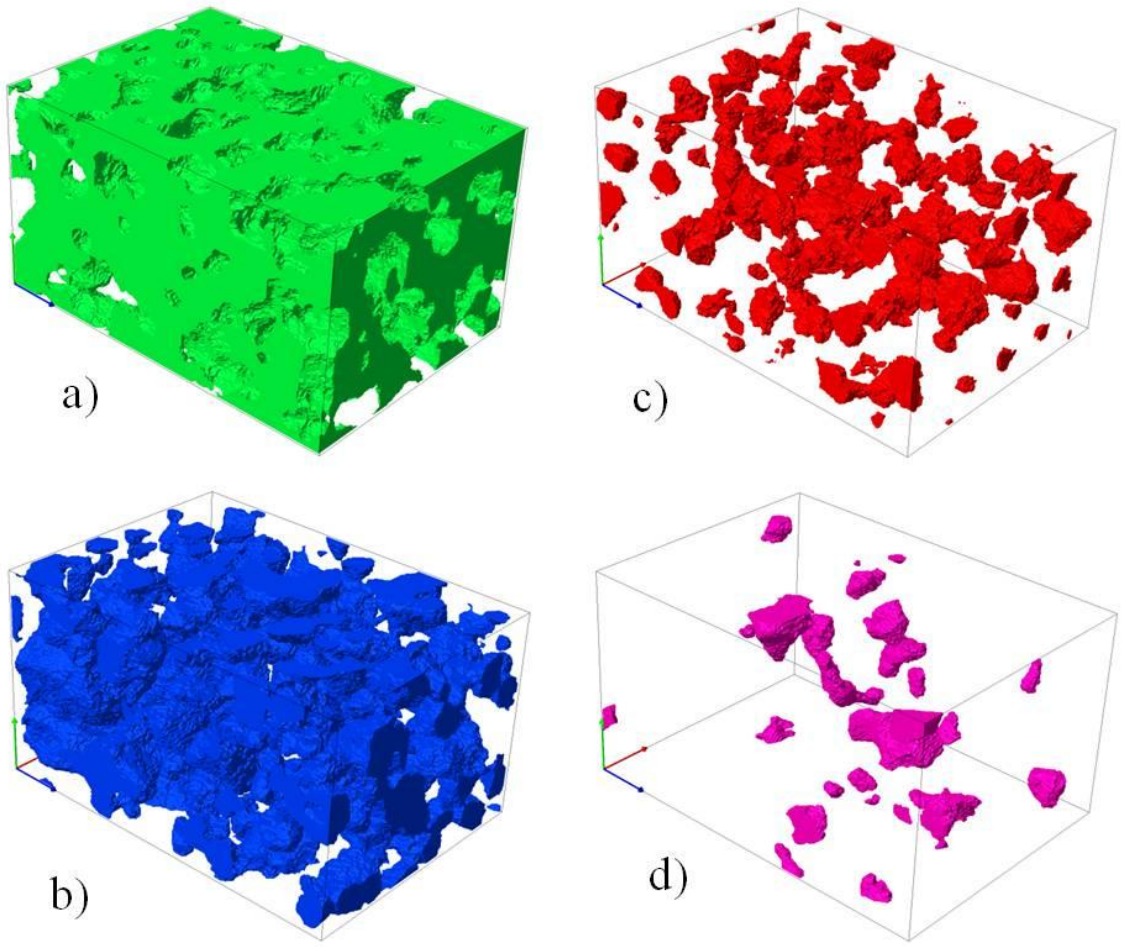

Figure 5.16. Three dimensional volume representation of separated constituents of 60%GDC-40%CFO- a) GDC, b) CFO, c) GFO and d) pore.

The above volume data can be manipulated by the Simpleware™ algorithm to generate volume a computational mesh for COMSOL calculation. Figure 5.17 shows mesh generated from the 3D volume of 60%GDC-40%CFO which can be directly exported into COMSOL™ Multiphysics to calculate impedance response, or for any other computational calculation.

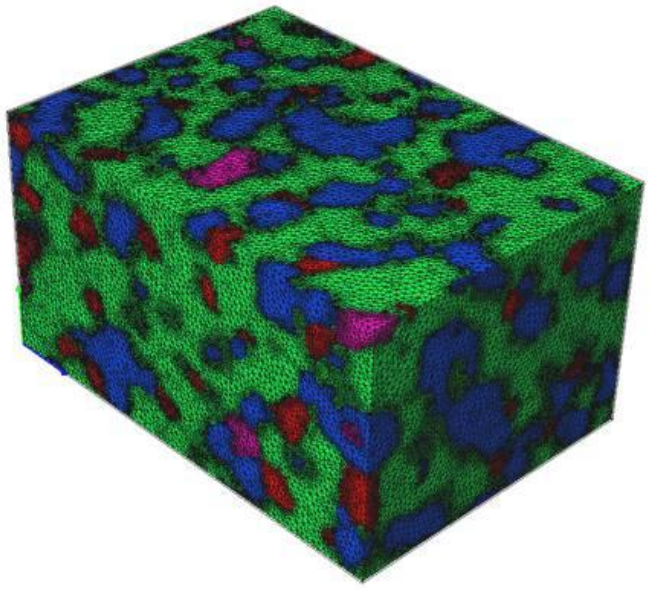

Figure 5.17. Three dimensional mesh representation 60%GDC-40%CFO membrane generated from Simpleware™.

5.4 Computational analysis of real membrane structure

We solved for the impedance and voltage distribution of the GDC-CFO structure using COMSOL Multiphysics. We obtained the domain mesh from Simpleware. The material properties of GDC and CFO used in the calculation were obtained from NOVOCONTRL measurements. We used GFO conductivity values from the literature and conductivity of air inside the pores from values provided in COMSOL. We applied a 1A current on one boundary with a frequency range of 0.1 HZ-1MHz. The opposite boundary of the input current boundary was kept at a ground potential, and the remaining boundaries were set as insulated boundary. Figure 5.18 shows the voltage distribution over the entire membrane. Different properties of the composite structures such as impedance, admittance, capacitance, permittvity, conductivity, and current flow path can

be obtained from the model. Figure 5.19 shows the impedance response of the membrane over a wide frequency range.

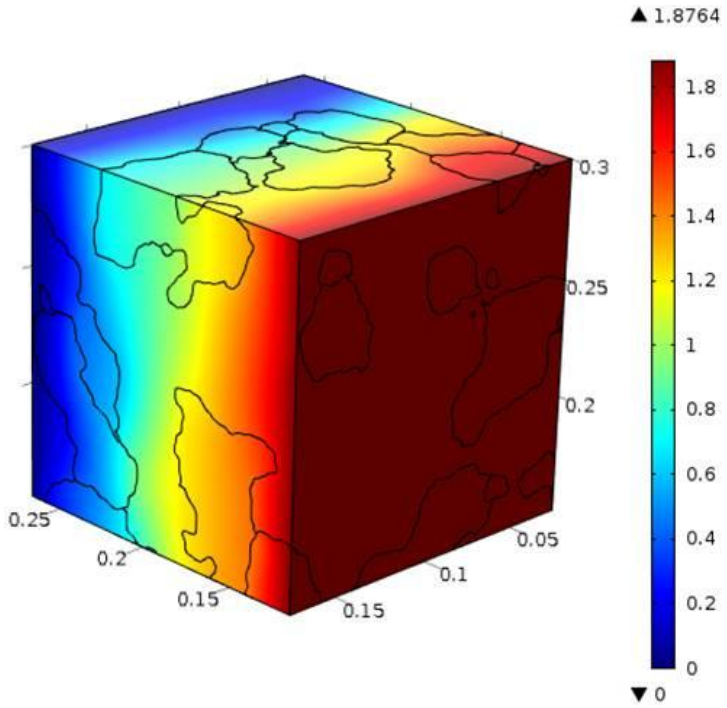

Figure 5.18. Voltage distribution in the 60%GDC-40%CFO membrane generated using COMSOL™.

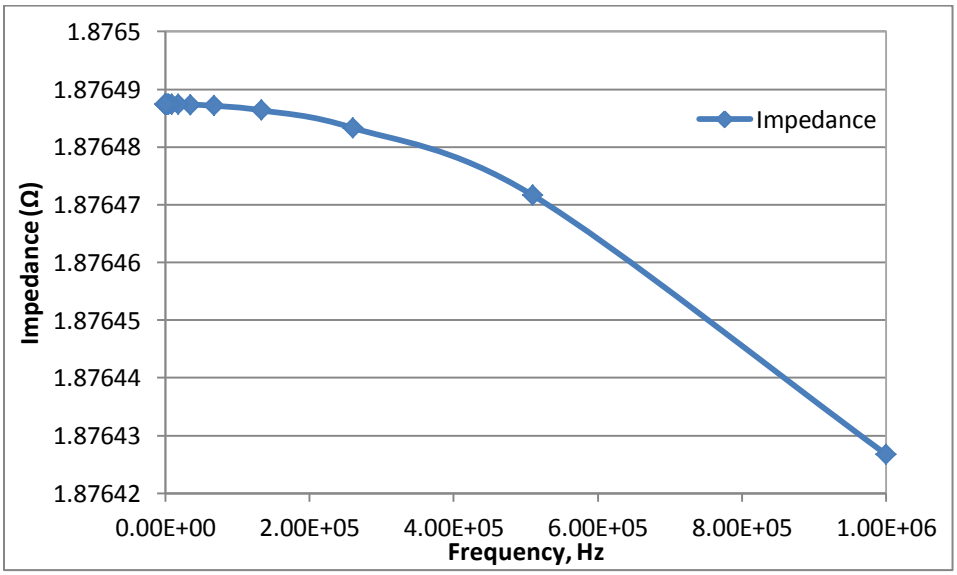

Figure 5.19. Impedance response of the 60%GDC-40%CFO membrane generated using COMSOL™.

This impedance response study of an actual membrane structure by creating domain from the real material gives us the capability to simulate different membrane mechanisms using COMSOL. In our future work, development of a computational model of membrane is under way where membrane operation will be simulated based on Nernst-Planck equation shown in Equation 5.4.

$$\mathbf{N}_i = -D_i \nabla c_i - z_i u_{m,i} F c_i \nabla \varphi + c_i \mathbf{u} \tag{5-4}$$

where N_i denote the mass flux vector (SI unit: mol/(m^2·s)) c_i is the concentration of species i (SI unit: mol/m^3), D_i is the diffusion coefficient of species i (SI unit: m^2/s), u is the solvent velocity (SI unit: m/s), F refers to Faraday's constant (SI unit: s·A/mol), φ denotes the electric potential (SI unit: V), z_i is the charge number of the ionic species (dimensionless), and $u_{m,i}$ its ionic mobility (SI unit: s·mol/kg). In this model ionic species subjected to electric fields are affected by migration transport in addition to the existing mass transport by diffusion and convection. Migration implies that positive ions migrate from positive to negative potential, and vice versa for negatively charged ions. For our case, we will consider diffusion through the solid membrane and omit the convection term in the solution. Also by coupling impedance response and flux transfer models in COMSOL, it will be possible to simulate impedance response of an operating membrane. In that case frequency and temperature dependent material properties obtained by NOVOCONTROL™ can be used for calculation.

CHAPTER 6

CONCLUSION

In this dissertation work, our goal was to study oxygen flux behavior influenced by various material and system parameters and also to understand the relationship between the internal mechanisms of dielectric behaviors of a mixed ionic electronic conducting (MIEC) oxygen separation membrane and the resulting flux in a heterogeneous functional material system.

For our study, we chose perovskite type gadolinium doped ceria-$Ce_{0.8}Gd_{0.2}O_{1.9}$ (CGO) as the ionic phase and spinel type cobalt ferrite-$CoFe_2O_4$ (CFO) as the electronic conductive phase. Nano powders of GDC and CFO were used to make the membranes of volume percentage of 50%GDC-50%CFO, 60%GDC-40%CFO and 80%GDC-20%CFO, die-pressed and sintered at 1300°C. Sample surface was polished to reduce surface roughness.

Microstructural characterization studies of the membranes were performed by scanning electron microscopy (SEM), X-ray diffraction (XRD) and energy dispersive X-ray spectroscopy (EDS). XRD and EDS data confirmed the presence of a third phase of gadolinium ferrite of two forms $GdFeO_3$ and/or $Gd_3Fe_5O_{12}$ in the three different mixture samples. Permeation flux of the membranes was experimentally measured by a gas chromatographer (GC) under several operating condition with varying temperature and oxygen partial pressure. SEM analysis of the two surfaces of the membranes operating

for 50-75 hours indicated degradation of the permeation side. Comparative studies showed membranes with higher CFO volume fraction had higher degradation among the membranes. This is likely due to the fact that CFO has a much lower sintering temperature compared to the GDC phase, much closer to the operating temperature of the membranes. For different volume fraction mixtures, flux comparisons indicated that the membrane flux did not follow the changes in volume fraction of the phases. An intermediate mixture of 60%GDC-40%CFO had the highest flux compared to the 50%GDC-50%CFO and 80%GDC-20%CFO samples. The lowest flux for the 80%GDC-20%CFO might be originated from the presence of the gadolinium ferrite species $Gd_3Fe_5O_{12}$ compared to $GdFeO_3$ present in the 60%GDC-40%CFO and 50%GDC-50%CFO samples. Also for the 80%GDC-20%CFO sample, the electronic phase had a smaller volume fraction compared to the other two mixture membranes. Consequently this electronic phase, which contributes to the overall membrane flux, could not percolate over the longer continuous electron paths causing the lower flux permeation values. SEM analysis of the membranes of different sintering conditions confirmed microstructural variations such as grain size and distribution of the different phases due to different sintering times and temperatures. Longer sintering times and higher sintering temperatures yielded larger grain size, and we saw increased flux permeation for membranes with larger grain size. It should be mentioned that our measured flux was lower than some other flux observed in investigations reported in the literature. This is due to the fact that our relative measurements were done within 50-75 hours of test time, but the absolute flux values for these materials would require much longer measurement times to allow for the equilibration of surface and volume effects.

The dielectric impedance response of single phase GDC, CFO and their different volume percent mixtures were measured. Temperature and frequency dependent single phase material properties were measured. Measured single phase values were comparable with literature values. The small differences might have originated from different starting material and sintering conditions. These single phase values were used in Wagner's equation to predict flux using a conformal COMSOL model to simulate impedance response on the real microstructure generated from three dimensional X-ray scans. Total conductivity of the mixture membranes were measured in different gaseous conditions. For all of the cases total conductivity increased with increasing CFO phase where 50GDC-50CFO had the highest value. This behavior was different from our measured flux behavior where an intermediate mixture of 60GDC-40CFO had the highest permeated flux. The in-situ impedance measurements showed that the lower sweep gas flow rates influenced the flux. So to investigate bulk material properties and interphase effects, higher flow rates of sweep gas are essential. Permittivity behavior at the lower temperatures also indicated electrode polarization. With increasing temperature, electrode polarization decreased and the real permittivity indicated non-ohmic conduction of oxygen ions through the membrane material.

Computational models using COMSOL Multiphysics was developed to study the impedance response of a given material domain. The model was validated using composite materials with regular geometric variations and experimentally measuring impedance response compared with computational values. Frequency and temperature dependent material properties of the single phase constituents, required for COMSOL calculation were measured using the NOVOCONTROL system. To study impedance

behavior of the real microstructure, three dimensional domains were created from X-ray nano-tomography. Initial calculations showed that the model was capable of resolving a large mesh of the real microstructure. Work is underway to develop a model to simulate oxygen flux transport using the Nernst-Planck equation and thus predict the impedance response of an operating membrane computationally by coupling the above models to measured or designed microstructures. Such an understanding and models would greatly reduce the cost and lost time of trial and error presently used to design heterogeneous functional materials like MIEC membranes.

REFERENCES

[1] U. B. Pal, D. E. Woolley, G. B. Kenney, Emerging SOM technology for the green synthesis of metals from oxides, JOM. 53 (2001) 32–35. doi: 10.1007/s11837-001-0053-4.

[2] K. Brinkman, T. Iijima, H. Takamura, The oxygen permeation characteristics of Bi1 − xSrxFeO3 mixed ionic and electronic conducting ceramics, Solid State Ion. 181 (2010) 53–58. doi:10.1016/j.ssi.2009.11.016.

[3] H. Takamura, M. Ogawa, K. Suehiro, H. Takahashi, M. Okada, Fabrication and characteristics of planar-type methane reformer using ceria-based oxygen permeable membrane, Solid State Ion. 179 (2008) 1354–1359. doi:10.1016/j.ssi.2008.04.001.

[4] R. P. O'Hayre, S. W. Cha, W. Colella, F. B. Prinz, Fuel cell fundamentals, John Wiley & Sons, Hoboken, New Jersey, 2006.

[5] C. Yang, A. Coffin, and F. Chen, "High temperature solid oxide electrolysis cell employing porous structured (La0.75Sr0.25)0.95MnO3 with enhanced oxygen electrode performance," *Int. J. Hydrog. Energy*, vol. 35, no. 8, pp. 3221–3226, Apr. 2010.

[6] T. Ishihara, Y. Tsuruta, T. Todaka, H. Nishiguchi, and Y. Takita, "Fe doped LaGaO3 perovskite oxide as an oxygen separating membrane for CH4 partial oxidation," *Solid State Ion.*, vol. 152–153, pp. 709–714, Dec. 2002.

[7] H. Takamura, K. Enomoto, Y. Aizumi, A. Kamegawa, and M. Okada, "Preparation and oxygen permeability of Pr–Al-based perovskite-type oxides," *Solid State Ion.*, vol. 175, no. 1, pp. 379–382, 2004.

[8] Z. Shao, G. Xiong, H. Dong, W. Yang, and L. Lin, "Synthesis, oxygen permeation study and membrane performance of a Ba0.5Sr0.5Co0.8Fe0.2O3−δ oxygen-permeable dense ceramic reactor for partial oxidation of methane to syngas," *Sep. Purif. Technol.*, vol. 25, no. 1–3, pp. 97–116, Oct. 2001.

[9] V. V. Kharton, A. V. Kovalevsky, A. P. Viskup, F. M. Figueiredo, A. A. Yaremchenko, E. N. Naumovich, and F. M. B. Marques, "Oxygen permeability and faradaic efficiency of Ce0.8Gd0.2O2-δ-La0.7Sr0.3MnO3-δcomposites," in *Journal of the European Ceramic Society*, vol. 21, pp. 1763–1767.

[10] U. Nigge, H.-D. Wiemhöfer, E. W. J. Römer, H. J. M. Bouwmeester, and T. R. Schulte, "Composites of Ce0.8Gd0.2O1.9 and Gd0.7Ca0.3CoO3−δ as oxygen permeable membranes for exhaust gas sensors," *Solid State Ion.*, vol. 146, no. 1–2, pp. 163–174, Jan. 2002.

[11] C. S. Chen, B. A. Boukamp, H. J. M. Bouwmeester, G. Z. Cao, H. Kruidhof, A. J. A. Winnubst, and A. J. Burggraaf, "Microstructural development, electrical properties and oxygen permeation of zirconia-palladium composites," *Solid State Ion.*, vol. 76, no. 1–2, pp. 23–28, Feb. 1995.

[12] J. Sunarso, S. Baumann, J. M. Serra, W. A. Meulenberg, S. Liu, Y. S. Lin, and J. C. Diniz da Costa, "Mixed ionic–electronic conducting (MIEC) ceramic-based membranes for oxygen separation," *J. Membr. Sci.*, vol. 320, no. 1–2, pp. 13–41, Jul. 2008.

[13] B. Wang, M. Zhan, D. Zhu, W. Liu, and C. Chen, "Oxygen permeation and stability of Zr0.8Y0.2O0.9–La0.8Sr0.2CrO3-δ dual-phase composite," *J. Solid State Electrochem.*, vol. 10, no. 8, pp. 625–628, Aug. 2006.

[14] X. S. Wu, C. L. Yang, C. S. Chen, and W. Liu, “Oxygen permeation through a Bi1.5Y0.3Sm0.2O3–La0.8Sr0.2MnO3−_δ dual-phase composite membrane,” in *Proceedings of the Ninth International Conference on Inorganic Membranes*, R. Bredesen and H. Raeder, Eds. Lillehamer, Norway: SINTEF, 2006, pp. 570–574.
[15] H. Wang, W. S. Yang, Y. Cong, X. Zhu, and Y. S. Lin, “Structure and oxygen permeability of a dual-phase membrane,” *J. Membr. Sci.*, vol. 224, no. 1–2, pp. 107–115, Oct. 2003.
[16] V. V. Kharton, A. V. Kovalevsky, A. P. Viskup, F. M. Figueiredo, A. A. Yaremchenko, E. N. Naumovich, and F. M. B. Marques, “Oxygen permeability and faradaic efficiency of Ce0.8Gd0.2O2-δ-La0.7Sr0.3MnO3-δcomposites,” in *Journal of the European Ceramic Society*, 2001, vol. 21, pp. 1763–1767.
[17] C. S. Chen, B. A. Boukamp, H. J. M. Bouwmeester, G. Z. Cao, H. Kruidhof, A. J. A. Winnubst, and A. J. Burggraaf, “Microstructural development, electrical properties and oxygen permeation of zirconia-palladium composites,” *Solid State Ion.*, vol. 76, no. 1–2, pp. 23–28, Feb. 1995.
[18] E. Capoen, M. C. Steil, G. Nowogrocki, M. Malys, C. Pirovano, A. Löfberg, E. Bordes-Richard, J. C. Boivin, G. Mairesse, and R. N. Vannier, “Oxygen permeation in bismuth-based materials. Part I: Sintering and oxygen permeation fluxes,” *Solid State Ion.*, vol. 177, no. 5–6, pp. 483–488, Feb. 2006.
[19] J. Kim and Y. S. Lin, “Synthesis and oxygen permeation properties of ceramic-metal dual-phase membranes,” *J. Membr. Sci.*, vol. 167, no. 1, pp. 123–133, Mar. 2000.
[20] K. Wu, S. Xie, G. S. Jiang, W. Liu, and C. S. Chen, “Oxygen permeation through (Bi2O3)0.74(SrO)0.26–Ag (40% v/o) composite,” *J. Membr. Sci.*, vol. 188, no. 2, pp. 189–193, Jul. 2001.
[21] Y. Teraoka, H.-M. Zhuang, S. Furukawa, and N. Yamazoe, “Oxygen permeation through Perovskite-type oxides,” *Chem. Lett.*, no. 11, pp. 1743–1746.
[22] P. N. Dyer, R. E. Richards, S. L. Russek, and D. M. Taylor, “Ion transport membrane technology for oxygen separation and syngas production,” *Solid State Ion.*, vol. 134, no. 1–2, pp. 21–33, Oct. 2000.
[23] P. J. Gellings and H. J. Bouwmeester, *Handbook of Solid State Electrochemistry*. CRC Press, 1997.
[24] S. P. S. Badwal and F. T. Ciacchi, “Ceramic Membrane Technologies for Oxygen Separation,” *Adv. Mater.*, vol. 13, no. 12–13, pp. 993–996, Jul. 2001.
[25] J. Fleig, “The grain boundary impedance of random microstructures: numerical simulations and implications for the analysis of experimental data,” *Solid State Ion.*, vol. 150, no. 1–2, pp. 181–193, Sep. 2002.
[26] C. M. Mari and G. Dotelli, “How to forecast the electrical behaviour of ionic conductor composites?,” *J. Mater. Sci.*, vol. 36, no. 5, pp. 1141–1147, Mar. 2001.
[27] Z. L. Wang and Z. C. Kang, *Functional and Smart Materials: Structural Evolution and Structure Analysis*. Springer.
[28] P. Dutta, S. Pal, M. S. Seehra, Y. Shi, E. M. Eyring, and R. D. Ernst, “Concentration of Ce3+ and Oxygen Vacancies in Cerium Oxide Nanoparticles,” *Chem. Mater.*, vol. 18, no. 21, pp. 5144–5146, Oct. 2006.
[29] W.-Q. Han, L. Wu, and Y. Zhu, “Formation and Oxidation State of CeO2-x Nanotubes,” *J. Am. Chem. Soc.*, vol. 127, no. 37, pp. 12814–12815, Sep. 2005.

[30] J. A. Kilner and B. C. H. Steele, “Mass Transport in Anion-Deficient Fluorite Oxider,” in *Nonstoichiometric Oxides*, O. T. Soerensen, Ed. Elsevier, 1981.
[31] H. Inaba and H. Tagawa, “Ceria-based solid electrolytes,” *Solid State Ion.*, vol. 83, no. 1–2, pp. 1–16, Jan. 1996.
[32] G. Wulfsberg, *Inorganic Chemistry. Sausalito*. University Science Books, 2000.
[33] A. Goldman, “Crystal Structure of Ferrite,” in *Modern Ferrite Technology*, 2nd ed., Springer, 2006, pp. 51–69.
[34] C. Wagner, “Z. physik,” *ChemLeipzig B*, vol. 21, p. 25, 1933.
[35] L. Zhang, N. Xu, X. Li, S. Wang, K. Huang, W. H. Harris, and W. K. S. Chiu, “High CO2 permeation flux enabled by highly interconnected three-dimensional ionic channels in selective CO2 separation membranes,” *Energy Environ. Sci.*, vol. 5, no. 8, pp. 8310–8317, Jul. 2012.
[36] S.-J. Song, J.-H. Moon, T. H. Lee, S. E. Dorris, and U. Balachandran, “Thickness dependence of hydrogen permeability for Ni–BaCe0.8Y0.2O3 − δ,” *Solid State Ion.*, vol. 179, no. 33–34, pp. 1854–1857, Oct. 2008.
[37] P. a. M. Steeman and J. van Turnhout, “Dielectric Properties of Inhomogeneous Media,” in *Broadband Dielectric Spectroscopy*, P. D. F. Kremer and P.-D. D. A. Schönhals, Eds. Springer Berlin Heidelberg, 2003, pp. 495–522.
[38] R. W. Sillars, “The properties of a dielectric containing semiconducting particles of various shapes,” *J. Inst. Electr. Eng.*, vol. 80, no. 484, pp. 378–394, Apr. 1937.
[39] K. Wagner, “The after effect in dielectrics,” *Arch Electrotech*, vol. 2, pp. 378–394, 1914.
[40] D. Bruggeman, “Dielektrizitatskonstanten und Leitfahigkeiten der Mishkorper aus isotropen Substanzen,” *Ann PhysLeipzig*, vol. 24, pp. 636–664, 1935.
[41] G. Bánhegyi, “Comparison of electrical mixture rules for composites,” *Colloid Polym. Sci.*, vol. 264, no. 12, pp. 1030–1050, Dec. 1986.
[42] R. R. Bilboul, “A note on the permittivity of a double-layer ellipsoid,” *J. Phys. Appl. Phys.*, vol. 2, no. 6, p. 921, Jun. 1969.
[43] P. Buttin, B. Malki, P. Barberis, B. Baroux, and U. Cedex, “Solid State Transport of Reactive Charged Particles: Application to Metal Oxidation,” 2010.
[44] G. C. Papanicolaou, A. F. Koutsomitopoulou, and A. Sfakianakis, “Effect of thermal fatigue on the mechanical properties of epoxy matrix composites reinforced with olive pits powder,” *J. Appl. Polym. Sci.*, vol. 124, no. 1, pp. 67–76, 2012.
[45] G. J. Nelson, K. N. Grew, J. R. Izzo Jr., J. J. Lombardo, W. M. Harris, A. Faes, A. Hessler-Wyser, Van herle Jan, S. Wang, Y. S. Chu, A. V. Virkar, and W. K. S. Chiu, “Three-dimensional microstructural changes in the Ni–YSZ solid oxide fuel cell anode during operation,” *Acta Mater.*, vol. 60, no. 8, pp. 3491–3500, May 2012.
[46] I. Kagomiya, T. Iijima, H. Kakuta, and H. Takamura, “Oxygen Permeable Ce0.8Gd0.2 O 1.9 - CoFe2 O 4 Thin Films Prepared on Porous Ce0.8Gd0.2 O 1.9 Substrates,” *Electrochem. Solid-State Lett.*, vol. 8, no. 1, pp. A70–A73, Jan. 2005.
[47] H. Takamura, M. Kawai, K. Okumura, A. Kamegawa, and M. Okada, “Preparation and Oxygen Permeability of Gd-Doped Ceria and Spinel-Type Ferrite Composites,” *MRS Online Proc. Libr.*, vol. 756, 2002.
[48] B. Lal, K. K. Bamzai, P. N. Kotru, and B. M. Wanklyn, “Microhardness, fracture mechanism and dielectric behaviour of flux-grown GdFeO3 single crystals,” *Mater. Chem. Phys.*, vol. 85, no. 2–3, pp. 353–365, Jun. 2004.

[49] P. B. A. Fechine, F. M. M. Pereira, M. R. P. Santos, F. P. Filho, A. S. de Menezes, R. S. de Oliveira, J. C. Góes, L. P. Cardoso, and A. S. B. Sombra, "Microstructure and magneto-dielectric properties of ferrimagnetic composite GdIGX:YIG1−X at radio and microwave frequencies," *J. Phys. Chem. Solids*, vol. 70, no. 5, pp. 804–810, May 2009.
[50] S. M. Murphy, D. A. Slade, K. J. Nordheden, and S. M. Stagg-Williams, "Increasing oxygen flux through a dense oxygen permeable membrane by photolithographic patterning of platinum," *J. Membr. Sci.*, vol. 277, no. 1–2, pp. 94–98, Jun. 2006.
[51] A. Thursfield and I. S. Metcalfe, "Air separation using a catalytically modified mixed conducting ceramic hollow fibre membrane module," *J. Membr. Sci.*, vol. 288, no. 1–2, pp. 175–187, Feb. 2007.
[52] P. G. Huray, *Maxwell's Equations*. John Wiley & Sons, 2011.
[53] F. Kremer and A. Schönhals, Eds., *Broadband dielectric spectroscopy*. Springer, 2003.
[54] F. Kremer, L. Dominguez, W. H. Meyer, and G. Wegner, "Thermal and dielectric properties of glassy ionenes," *Polymer*, vol. 30, no. 11, pp. 2023–2029, Nov. 1989.
[55] K. W. Wagner, "The after effect in dielectrics," *Arch Electrotech*, vol. 2, pp. 378–394, 1914.
[56] R. W. Sillars, "The properties of a dielectric containing semiconducting particles of various shapes," *J. Inst. Electr. Eng.*, vol. 80, no. 484, pp. 378–394, Apr. 1937.
[57] J. C. Dyre and T. B. Schrøder, "Universality of ac conduction in disordered solids," *Rev. Mod. Phys.*, vol. 72, no. 3, pp. 873–892, Jul. 2000.
[58] A. Bunde, P. Maass, H. E. Roman, W. Dieterich, and J. Petersen, "Transport of disordered structures: Effect of long range interactions," *Solid State Ion.*, vol. 40–41, Part 1, pp. 187–191, Aug. 1990.
[59] K. Funke and R. Hoppe, "Jump-relaxation model yields Kohlrausch-Williams-Watts behaviour," *Solid State Ion.*, vol. 40–41, Part 1, pp. 200–204, Aug. 1990.
[60] A. K. Jonscher, *Dielectric relaxation in solids*. Chelsea Dielectrics, London, 1983.
[61] A. K. Jonscher, "Dielectric relaxation in solids," *J. Phys. Appl. Phys.*, vol. 32, no. 14, p. R57, Jul. 1999.
[62] N. F. Mott and E. A. Davis, *Electronic Processes in Non-Crystalline Materials*. Oxford University Press, 2012.
[63] H. Böttger and V. V. Bryksin, *Hopping conduction in solids*. VCH Weinheim, 1985.
[64] S. R. Eliot, *Physics of amorphous materials*. Longman, London, 1990.
[65] A. J. Epstein, "AC conductivity of polyacytylene: Distinguishing mechanisms of charge transport," in *Handbook of Conducting Polymers, Second Edition,*, T. A. Skotheim, Ed. New York: Marcel Dekker, 1986, p. 1041.
[66] K. L. NGai and R. W. Rendell, in *Handbook of conducting polymers*, T. A. Skotheim, Ed. 1986, pp. 967–1039.
[67] C. A. Angell, "Fast ion motion in glassy and amorphous materials," *Solid State Ion.*, vol. 9–10, Part 1, pp. 3–16, Dec. 1983.
[68] C. A. Angell, "Dynamic processes in ionic glasses," *Chem. Rev.*, vol. 90, no. 3, pp. 523–542, May 1990.
[69] A. L. Efros and B. I. Shklovskii, *Electronic properties of doped semiconductors*. Springer-Verlag Berlin Heidelberg GmbH, 1984.

[70] T. Tsutsui, R. Tanaka, and T. Tanaka, “Dynamic mechanical properties of some novel ionene polymers,” *J. Polym. Sci. Polym. Phys. Ed.*, vol. 13, no. 11, pp. 2091–2102, Nov. 1975.
[71] F. Kremer, T. A. Ezquerra, M. Mohammadi, W. Bauhofer, T. A. Vilgis, and G. Wegner, “Dynamic percolation in an insulator-conductor composite: Polyethyleneoxide-polypyrrole, as studied by a.c. conductivity measurements,” *Solid State Commun.*, vol. 66, no. 2, pp. 153–157, Apr. 1988.
[72] R. Pelster and U. Simon, “Nanodispersions of conducting particles: preparation, microstructure and dielectric properties,” *Colloid Polym. Sci.*, vol. 277, no. 1, pp. 2–14, Feb. 1999.
[73] O. H. Kwon and G. M. Choi, “Electrical conductivity of thick film YSZ,” *Solid State Ion.*, vol. 177, no. 35–36, pp. 3057–3062, Nov. 2006.
[74] S. Wang, T. Kobayashi, M. Dokiya, and T. Hashimoto, “Electrical and Ionic Conductivity of Gd-Doped Ceria,” *J. Electrochem. Soc.*, vol. 147, no. 10, pp. 3606–3609, Oct. 2000.
[75] T. Kudo and H. Obayashi, “Mixed Electrical Conduction in the Fluorite-Type Ce1 − x Gd x O 2 − x / 2,” *J. Electrochem. Soc.*, vol. 123, no. 3, pp. 415–419, Mar. 1976.
[76] T. Ivers-Tiffee and D. Küstner, “Electrical behavior of doped ceria,” *Silic. Ind.*, vol. 49, no. 11–12, pp. 227–230, 1984.
[77] O. A. Stafford, B. R. Hinderliter, and S. G. Croll, “Electrochemical impedance spectroscopy response of water uptake in organic coatings by finite element methods,” *Electrochimica Acta*, vol. 52, no. 3, pp. 1339–1348, Nov. 2006.
[78] F. Rabbi and K. Reifsnider, “Relationship of Micro-Structure Morphology to Impedance in Heterogeneous Functional Materials,” 2010, pp. 393–397.
[79] J. Baker, J. M. Adkins, F. Rabbi, Q. Liu, K. Reifsnider, and R. Raihan, “Meso-design of heterogeneous dielectric material systems: Structure property relationships,” *J. Adv. Dielectr.*, p. 1450008, May 2014.
[80] G. J. Nelson, W. M. Harris, J. J. Lombardo, J. R. Izzo Jr., W. K. S. Chiu, P. Tanasini, M. Cantoni, Van herle Jan, C. Comninellis, J. C. Andrews, Y. Liu, P. Pianetta, and Y. S. Chu, “Comparison of SOFC cathode microstructure quantified using X-ray nanotomography and focused ion beam–scanning electron microscopy,” *Electrochem. Commun.*, vol. 13, no. 6, pp. 586–589, Jun. 2011.
[81] J. R. Izzo, A. S. Joshi, K. N. Grew, W. K. S. Chiu, A. Tkachuk, S. H. Wang, and W. Yun, “Nondestructive Reconstruction and Analysis of SOFC Anodes Using X-ray Computed Tomography at Sub-50 nm Resolution,” *J. Electrochem. Soc.*, vol. 155, no. 5, pp. B504–B508, May 2008.
[82] Y. K. Chen-Wiegart, W. M. Harris, J. J. Lombardo, W. K. S. Chiu, and J. Wang, “Oxidation states study of nickel in solid oxide fuel cell anode using x-ray full-field spectroscopic nano-tomography,” *Appl. Phys. Lett.*, vol. 101, no. 25, p. 253901, Dec. 2012.
[83] W. M. Harris, K. S. Brinkman, Y. Lin, D. Su, A. P. Cocco, A. Nakajo, M. B. DeGostin, Y. K. Chen-Wiegart, J. Wang, F. Chen, Y. S. Chu, and W. K. S. Chiu, “Characterization of 3D interconnected microstructural network in mixed ionic and electronic conducting ceramic composites,” *Nanoscale*, vol. 6, no. 9, p. 4480, 2014.